Contacts and Interface Evolution in Thermoelectric Modules

Malik, Safdar Abbas

Publication date:
2018

Document Version
Publisher's PDF, also known as Version of record

Contacts and Interface Evolution in Thermoelectric Modules

PhD Thesis by:

Safdar Abbas Malik

Principal Supervisor:

Dr. Ngo Van Nong

Associate Professor

Co-supervisor:

Dr. Eugen Stamate

Senior Scientist

Department of Energy Conversion and Storage

Technical University of Denmark

August 2018

DTU Energy

Department of Energy Conversion and Storage

Declaration:

This is second version of the thesis. The following changes have been made to the first version:-

1. Some figures were enlarged to make the text in them more readable (figures: 1.1, 1.9, 3.3, 3.4, 3.5).

2. Some typing mistakes were corrected.

3. In the introduction chapter, following sentences were added to make the content more clear and elaborate:-

   i. On page 3, last line reads: “In this system, ~ 25% of the lattice vibrations have the mean free path between 1nm to 5nm, and ~ 55% of the phonon modes lie in the range of 5nm to 100 nm. The phonon modes with mean free paths in the range of 0.1µm to 1µm constitute only 20% of the lattice thermal conductivity”. This is added to describe figure 1.2.

   ii. On page 8, the third line after equation 1.10 reads: “The pressure term is important in sintering processes that involve high pressure, e.g. formation of Diamond under high pressure deep inside the earth. Entropy also becomes important in ordered systems, e.g. in the case of superlattices, like the Au-Cu alloy, where different kinds of atoms occupy definite geometrical positions instead of diffusing randomly”.

Abstract

As human civilization faces global warming as the biggest existential threat it has ever faced, harnessing waste heat is a sustainable, renewable source of energy to reduce our dependence on fossil fuels. By directly converting heat into electricity, thermoelectricity offers solutions for waste heat recovery. In the past, very stable and high-performance telluride based thermoelectric generators (TEG) have been used for extraterrestrial missions to provide the energy needed for probing the dark deep space. In the recent years, the interest in application of this technology to automobiles, factories, power plants, military and households has increased. There has been great advancement in discovery of new and smart materials, exhibiting high thermoelectric (TE) performance, but the transition towards their commercialization is not smooth. While many new materials, such as Zn_4Sb_3, Mg_2Si, SnSe, skutterudites, Cu_2Se, etc., have been reported to show very high thermoelectric performance, the application of these materials in commercial TEGs is still hindered. One of the key challenges is to form stable and low resistant contacts for intensive working conditions. In this thesis, different joining methods were developed to make contacts between various TE materials and metallic electrodes. Interfacial microstructure evolution was investigated to study the contact stability and degradation mechanism. ZnSb was first chosen because it is non-toxic, low-cost, abundant and light weight thermoelectric material. The successful method developed for ZnSb is then extended to $CoSb_3$ based Skutterudites, which are among the highest performing TE materials in the temperature range (300 ^{o}C-600 ^{o}C).

In the first part, conventional joining method using soldering alloys was investigated. Low-cost high performance ZnSb material was chosen to bond with different metal electrodes such as Ag, Ni and Crofer 22 APU using some commercially available Zn-based solders. The joints were tested for long time at high temperature and the interfacial microstructure and chemical composition were observed using scanning electron microscope equipped with energy dispersive x-ray spectrometer (EDS). It was found that both Ag and Ni electrodes reacted with Zn-based solders and formed a thick diffusion layer comprising of different intermetallic phases. Furthermore, Zn was found to deeply diffuse into ZnSb TE leg, resulting in change of material composition. Introduction of thick films of Ti and Cr as buffer layers could not stop this diffusion. In case of Crofer 22 APU, the reaction layer was found to be minor; suggesting that Crofer 22 APU was a good electrode to be used with Zn-based solders.

A novel solder-free joining method using microlayers of Ti and Cr as interconnecting agents was then developed and demonstrated on the ZnSb TE system. It was found that, using microlayers of Ti and Cr as interconnecting agents, a very good interfacial contact was obtained without any gaps or cracks. Interestingly, the starting composition of ZnSb legs was also preserved. The interfacial contact of ZnSb/Cr/Ni was found to be stable after heat treatment at 400 ^{o}C for 30 hours, suggesting solder free joining as an effective method for reliable contacts in TE devices in the medium temperature range (200 ^{o}C-400 ^{o}C).

The solder free joining method was further developed and applied to different high-performance materials in higher temperature range. A very stable n-type skutterudite material was chosen to join with Crofer 22 APU electrode. The joint was tested at 550 ^{o}C for 300 hours and the interfacial

microstructure was studied. Cr and Co based interconnecting layers were systematically investigated and it was found that the Cr/Co multilayer made the best contact.

Abstrakt

Da den menneskelige civilisation står overfor global opvarmning som et af de største eksistentielle kriser nogensinde, er konverteringen af spildvarme til en bæredygtig vedvarende energikilde en attraktiv løsning, der kan reducere afhængigheden af fossilt brændstof. Termoelektricitet gør det muligt at konvertere varme til elektricitet. Tidligere har højt ydende og stabile tellurid termoelektriske generatorer (TEG) været brugt, til missioner udenjordisk ved at forsyne den påkrævende energi til sondering af rummet. I de seneste år er der opstået interesse for at udnytte denne teknologi i områder som biler, fabrikker, kraftværker, militær og husholdninger. Der har været stor fremgang i opdagelsen af nye og effektive materialer med høj termoelektrisk (TE) ydeevne, men overgangen mod kommercialisering er stadig en udfordring. Selvom nye materialer som Zn_4Sb_3, Mg_2Si, SnSe, skutterudider, Cu_2Se, osv. har vist sig at have glimrende termoelektrisk ydeevne, men anvendelsen af disse materialer i kommercielle TEGs er stadig en udfordring. En af de største udfordringer er at producere en stabil og lav resistent kontakt til intensive arbejdsforhold. I denne tese er forskellige sammensætnings metoder blevet udviklet, til at skabe kontakt mellem forskellige TE materialer og metalliske elektroder. Udviklingen af grænseflade mikrostruktur er blevet undersøgt for at undersøge kontakt stabiliteten og nedbrydningsmekanismen. ZnSb blev valgt som det første materiale på baggrund af, at det er et termoelektrisk materiale, som er let, ugiftigt, billigt, og let tilgængeligt. Den succesfulde metode udviklet til ZnSb, blev derefter udvidet til $CoSb_3$ baseret skutterudider, som er blandt de bedste TE materialer ved en temperatur mellem 300 ^{o}C-600 ^{o}C.

Den første del af tesen undersøger konventionelle sammensætningsmetoder ved brug af lodningslegeringer. ZnSb blev valgt som materialet der skal bindes til forskellige metal elektroder som sølv, nikkel og Crofer 22 APU. Materialerne blev loddet sammen med kommercielle zink baseret loddematerialer. Sammensætningen blev testet i lang tid ved høj temperatur, hvorefter grænseflade mikrostruktur og kemisk komposition blev observeret ved brug af elektronmikroskop (SEM) og Energi-dispersive røntgen spektroskopi (EDS). Undersøgelsen viste at både sølv og nikkel elektroderne reagerer med de zink baserede loddematerialer, hvilket resulterede i et tykt diffusions lag bestående at forskellige intermetalliske faser. Det resulterede også i, at zink var dybt diffunderet i ZnSb, hvilket resulterede i en ændring af materiale kompositionen. Introduktionen af en tyk film bestående af titan eller krom som buffer lag var ikke i stand til at stoppe diffusionen. Ved brug af Crofer 22 APU, viste det sig at reaktionslaget var minimalt; hvilket tyder på, at Crofer 22 APU var det optimale elektrode valg til zink baseret loddematerialer.

En ny loddefri sammensætnings metode blev hermed udviklet, ved brug af mikrolag med titan og krom som sammenkoblings materialer. Denne metode blev demonstreret på ZnSB TE systemet. Undersøgelsen viste, at titan og krom mikrolag til sammenkoblingsmidler resulterede i et rigtig god grænseflade kontakt uden huller eller revner. Yderligere, var denne metode også i stand til at konservere den oprindelige komposition af ZnSb. Grænseflade kontakten af ZnSb/Cr/Ni viste sig at være stabil efter varme behandling ved 400 ^{o}C i 30 timer, hvilket tyder på at den lodnings frie metode er effektiv til at skabe pålidelig kontakt i TE enheder ved medium temperatur (200 ^{o}C-400 ^{o}C).

Den lodningsfri metode var yderligere udviklet og anvendt til forskellige højtydende materialer i en højere temperatur interval. En særdeles stabil n-type Skutterudite blev valgt til sammensætning med

Crofer 22 APU elektroden. Den blev testet ved 550 ^{o}C i mere end 300 timer, hvorefter grænsefladens mikrostruktur blev undersøgt. De sammenføjende lag baseret på Krom og kobolt blev undersøgt systematisk og resultatet viste, at et flerlagede krom/kobolt gav den bedste kontakt.

Acknowledgements

This thesis has come out as a result of my three years stay at the Risø campus of the Technical University of Denmark (DTU), whose beautiful and quiet location I always enjoyed. Both the beautiful beach and the work environment made my stay a positive and pleasant experience. Three years of studying at DTU has not only improved my understanding of the concepts of material science, but also taught me scientific way of thinking and self-management.

This work would not be possible without the guidance of my supervisors Dr. Ngo van Nong and Eugen Stamate. I have learned a lot from them, both in the form of discussions and interactions as a colleague. They taught me how to approach the scientific questions systematically, and motivated me to make my ideas a reality. Dr. Ngo van Nong is an intelligent material scientist who helped me throughout this research, from teaching me basic lab skills to discussing the outcome of experiments to improving my write up. Dr. Eugen Stamate performed his role as a co-supervisor to the best. He trained me on deposition of metallic films that was a crucial step towards development of the new joining method. I will also like to thank Prof. Nini Pryds, Dr. Rasmus Bjørk and Dr. Kasper K. Nielsen for being my supervisors for the first year and a half, I have learned a lot from them. Prof. Nini Pryds is an excellent material scientist and physicist, with a very busy schedule. I will like to thank him for discussions and guidance during the course work at DTU. I would like to express my gratitude for our section head, Dr. Severine Ramousse. I will also like to thank Prof. Mads Brandbyge of DTU Nanotech for discussions on electron transport. I gratefully acknowledge the financial support by the Danish Council for Strategic Research under the CTEC project No. 1305-00002B.

I will also like to thank my colleagues, both past and present, especially Dr. Le Thanh Hung, who has helped me a lot in the lab. I will also like to thank Jonas Lehmann, who helped me with the translation of the abstract of this thesis. I am grateful to other colleagues: Li Han, Ali Sarhadi, Stefano Dallolio, Nicola Mazzanti, Steeven H. Spangsdorf and Daniele Reschiotto. My special thanks go to the laboratory technicians and engineers Ebtisam Abdellahi, Jørgen Geyti, Soren Køch, Karl Thydén, Henrik Paulsen, and Carsten Gynther Sørensen. I will also like to acknowledge our secretaries, especially Connie Munch Westergaard and Anita Voss for all the administrative work.

I am also thankful to the assessment committee members, Dr. Per Eklund and Dr. Alireza Rezaniakolaei, for evaluating and assessing my thesis.

My deepest gratitude goes to my family: my wife for her continuous support and encouragement, and my child who is a source of joy and happiness for me.

List of Publications

(Scientific Journals)

1. Safdar Abbas Malik, Le Thanh Hung, Ngo Van Nong, "Solder free joining as a highly effective method for making contact between thermoelectric materials and metallic electrodes", Materials Today Energy, Volume 5, Pages 305-311 (2017).
2. Safdar Abbas Malik, Le Thanh Hung, Ngo Van Nong, "Microstructure and chemical data of the thermoelectric ZnSb material after joining to metallic electrodes and heat treatment", Data in Brief, Volume 15, Pages 97-101 (2017).
3. Shyam Prasad K, Ashok Rao, Benedict Christopher, Ruchi Bhardwaj, Nagendra Singh Chauhan, Safdar Abbas Malik, Ngo Van Nong, B.S. Nagaraja, Riya Thomas, "Tuning the thermoelectric properties by manipulating copper in Cu_2SnSe_3 system", Journal of Alloys and Compounds, Volume 748, Pages 273-280 (2018).

(Conference Proceedings)

1. Safdar Abbas Malik, Le Thanh Hung, Ngo Van Nong, "Contact of ZnSb thermoelectric material to metallic electrodes using S-Bond 400 solder alloy", Materials Today: Proceedings, ECT 2017 Special Issue (in press).

(Manuscript in preparation)

1. Safdar Abbas Malik, Eugen Stamate, Ngo Van Nong, "Solder free joining for $CoSb_3$ based Skutterudite thermoelectrics, manuscript in preparation (2018).

Contents

Chapter 1: Introduction

1.1 Thermoelectricity

Thermoelectricity is a coupled effect whereby heat gradients drive charge and/or spin. Seebeck in 1822 observed for the first time the Seebeck effect[1]: when he heated one end of a metallic rod, he observed a deflection in the compass needle placed near the rod. He, mistakenly, interpreted this effect as magnetism induced by temperature gradient. A year later, Hans Christian Ørsted, the founder and the first director of the Technical University of Denmark, identified this effect as heat induced electricity, and coined the term 'thermoelectricity'[2]. About 12 years later, Peltier observed the back action counterpart, the Peltier effect[3]: a temperature gradient was maintained between their junctions when electrical current was passed through a closed loop made of two dissimilar conductors. Lord Kelvin in 1850's established the relation between these two effects[4] and discovered a third thermoelectric phenomenon, the Thomson effect[5]: the absorption of heat in conductors subjected to a temperature gradient, when electrical current passes through them. The Thermoelectric effects are thermodynamically reversible; however, they are accompanied by irreversible processes like Joule heating.

Thermoelectric devices have a broad spectrum of applications[6]. They not only work silently, they can be very small, e.g. miniaturized thermoelectric modules can cool electronic devices at microscale[7−9]. These devices are widely used as temperature sensors in electrical appliances[10], Peltier coolers[11] and as source of energy in remote places, like deep space[12]. Recently, attempts are being made to use this technology as a waste heat recovery mechanism in industry[13]. However, low energy conversion efficiency is the main challenge faced by state-of-the-art thermoelectrics, as compared to fossil fuels.

1.1.1 Seebeck effect

The physics of Seebeck effect is as follows: the Fermi Dirac probability distribution function, 'f(E)' for the charge carriers in a conductor changes with temperature:

$$f(E) = \frac{1}{e^{(E-E_f/k_B T)}+1}. \qquad (1.1)$$

Where 'E' is the energy of the charge carriers, 'E_f' is the Fermi energy, 'k_B' is the Boltzmann constant and T is the temperature. When a material is subjected to thermal gradient, the probability function does not remain uniform throughout. The gradient in the probability function makes the charges flow.

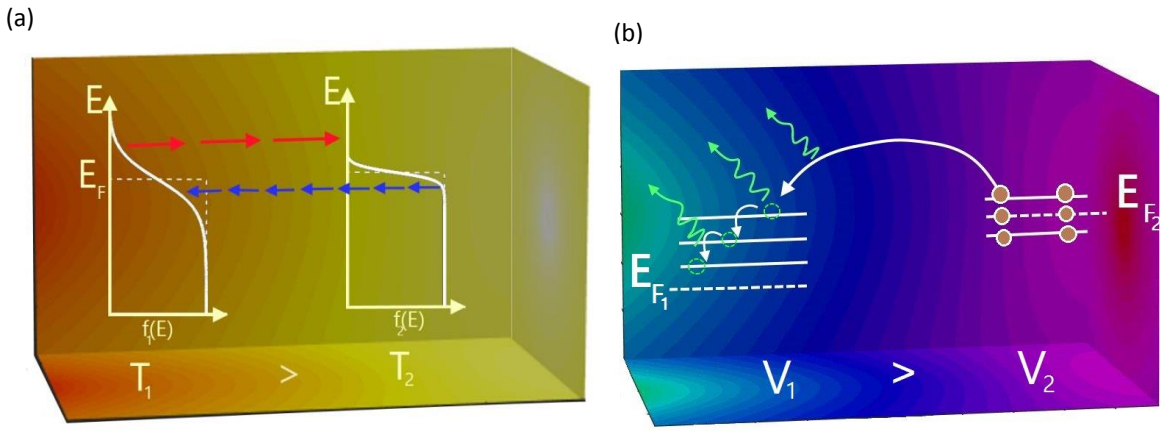

Figure 1.1: (a) Seebeck effect, **(b)** Peltier effect.

Figure 1.1(a) is a schematic diagram of the probability distribution at the hot and cold sides of a thermoelectric material. Temperature gradient, 'ΔT' induces a slope in probability distribution, $\frac{df(E)}{dT}$. High energy electrons (red) from hot side slide down to the low energy states in the cold side, while low energy electrons (blue) from the cold side diffuse into the low energy states in the hot side that were thermally vacated (bipolar transport). This process does not change the position of the Fermi level in the system, i.e. $\frac{dE_f}{dT} = 0$, and an open circuit voltage develops as a result, $\Delta V = \alpha \Delta T$; where $\alpha = \frac{1}{q}\frac{d(E-E_f)}{dT}$ is the Seebeck coefficient and 'q' is the charge of majority carriers (negative for electrons and positive for holes).

1.1.2 Peltier effect

When a potential difference is applied across a junction of two dissimilar conductors, carriers flowing across the junctions absorb thermal energy at one junction and release on the other, cooling the first with respect to the other. This is illustrated in figure 1.1(b). The electrical potential applied across the interface of two materials lowers the Fermi level of the end with positive bias with respect to that in the other part of the junction such that the electrons crossing the interface fall into lower vibronic levels, releasing phonons. This process heats up this end until its probability function spills beyond the Fermi level to the extent that the vibronic states contributing to the conduction across the interface are at the same energies. Depending upon the band structures of the materials in contact, a temperature gradient, 'ΔT', is established. The rate of heat transfer with respect to the supplied electrical current is defined as Peltier coefficient, 'π', and it is related to the Seebeck coefficient by the Kelvin relation: '$\pi = \alpha T$'.

1.1.3 Properties of thermoelectric materials

Enhancement of the efficiency of a thermoelectric material requires optimization of a series of conflicting material properties, namely: the Seebeck coefficient, 'α'; the electrical conductivity, 'σ'; and the thermal conductivity, 'κ'. The thermoelectric performance of a material is quantified in terms of the dimensionless figure of merit, 'zT'[14].

$$zT = \frac{\alpha^2 \sigma T}{\kappa} = \frac{nq\mu}{\kappa}\alpha^2 T \qquad (1.2)$$

where ‘μ’, the mobility of the carriers - each with charge ‘q’, is directly proportional to the thermal conductivity, ‘κ’, at a particular temperature, ‘T’. Similarly, the higher the carrier concentration, ‘n’, the lower is the Seebeck coefficient, ‘α’. Generally, a polycrystalline degenerate semiconductor, that can manage to sufficiently scatter phonons but provides high mobility to the charge carriers - a ‘phonon-glass electron-crystal’ - would establish the delicate balance between these parameters[15]. The first generation of bulk thermoelectric materials was produced till a century ago with zT of 0·1−0·6. A revival in the research came in 1990’s when it was predicted theoretically that nanostructural engineering could enhance the thermoelectric efficiency of a material[16]. This explained the high efficiency of the second-generation materials, that came in 1960’s with traces of nanostructuring, having zT values around 0·8−1·7. The aim for the third generation to come is to achieve zT values greater than 2.

Ioffe in 1957 argued that compound semiconductors not only had high Seebeck coefficients, but they also had lower thermal conductivities as compared to metals, and the degree of scattering of phonons in a disordered material was higher than that of electrons. His magnum opus ‘Semiconductor Thermoelements and Thermoelectric Cooling’ [14] gave a new life to thermoelectricity and marked the beginning of the second generation of thermoelectrics. The denominator of equation 1.2, ‘κ’, is the sum of electronic thermal conductivity, ‘κ_e’, and lattice thermal conductivity, ‘κ_l’. Electronic thermal conductivity is related to the electrical conductivity by Wiedemann-Franz law: $\kappa_e = \sigma LT$, where ‘L’ is the Lorentz number. For metals, the electronic part accounts for most of the thermal conduction, but for semiconductors, most of the heat is carried by lattice vibrations. The lower its thermal conductivity, the higher temperature gradient a material can maintain.

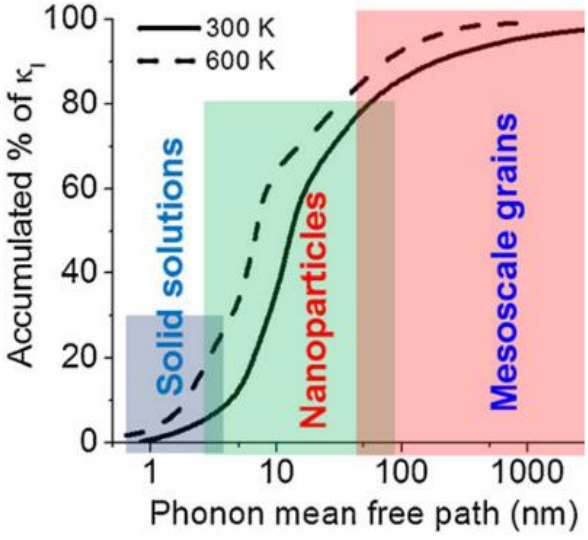

Figure 1.2: Contributions of phonons with various mean free paths to the accumulated lattice thermal conductivity of PbTe, calculated at temperatures of 300K and 600K. Image adapted from[17].

To improve the figure of merit, most of the attention has been paid to lowering the lattice thermal conductivity by controlling the microstructure of materials such that the electronic and heat conduction are decoupled[15], [17]. In PbTe[17], one of the leading thermoelectric materials discovered in 1960’s, the typical value of electronic mean free path is ≈ 30nm, while phonons have mean free paths in a wide range of 1nm – 10μm as depicted in figure 1.2. In this system, ~ 25% of the lattice vibrations have the mean free path between 1nm to 5 nm,

and ~ 55% of the phonon modes lie in the range of 5nm to 100 nm. The phonon modes with mean free paths in the range of 0.1µm to 1µm constitute only 20% of the lattice thermal conductivity. The transport of electrons and phonons is sufficiently decoupled because of disorder on multiple length scales: from polycrystalline grain boundaries to nanoinclusions to point defects. These defects do scatter electrons as well, but it turns out to be an affordable compromise. However, there is a limit to this route[18], although - in theory - it has been recently proposed that careful nanoarchitecture can get over this limit[19]. The numerator of equation 1.2 contains the Power Factor, '$\alpha^2\sigma$', which depends on the density and dispersion of energy states in the vicinity of Fermi level. These are the states that take part in the charge transport. Recently, people have started paying more attention to modifying the electronic structure to improve the power factors, making novel materials that involve careful doping and/or nanofabrication[20]–[22]. Point defects not only prove to be useful in scattering phonons, but also, they may improve electrical power factor by providing higher carrier concentrations or resonant electron states near the Fermi level[23]–[25]. Moreover, Interface potentials at nanoinclusions and the grain boundaries can suppress the disadvantageous bipolar transport of thermally generated electron-hole pairs in most narrow bandgap thermoelectrics.

Thermoelectric energy converters usually operate at temperatures higher than the normal temperature range for most semiconductors. Therefore, their stability at high temperature is a matter of great concern, and while a material may exhibit very good thermoelectric properties, it may not be able to withstand high temperature gradients and long operating times[26]. This emphasizes importance of investigating phenomena like strains within these materials[27], phase transitions[28], thermal expansion[29], mechanical strength[30], oxidation and sublimation[31], etc.

1.2 Thermoelectric devices

Conventional thermoelectric devices are fabricated as set of unicouples whereby each unicouple has one leg of p- and one of n-type thermoelectric material, with dimensions of few millimeters, which are connected electrically in series but thermally in parallel as shown in figure 1.3.

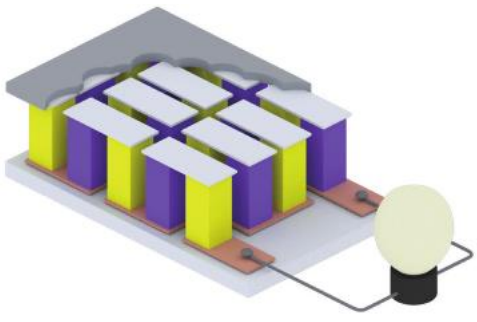

Figure 1.3: A conventional thermoelectric module. The yellow and purple colours demonstrate the p- and n-type of conduction. The assembly is packed between two thermally conducting ceramic plates (e.g. alumina or beryllia). Metallic strips (e.g. copper) are used as electrodes for electrical conduction. Image adapted from [32].

When these legs are subjected to a heat gradient, their carriers flow towards their colder ends and, due to difference in sign, a potential difference of a few millivolts per degree is achieved

between the colder ends of both the legs. The magnitude of the potential difference depends upon the temperature difference between the hot and the cold sides, as well as on intrinsic properties of the materials used. If this set up has to be used as a Peltier cooler, electrical power needs to be supplied to pump heat from one end to the other. The performance and stability of a thermoelectric device is not only dependent on the performance and stability of the thermoelectric materials that the legs are made of, but also on the properties of electrodes and the soldering/brazing alloys that connect the legs to the electrode stripes. It also depends on the temperature gradient that is applied across the device. Therefore, not only the physical properties of the p- and n-type semiconductors have to be taken into consideration, but also the properties of the metal-semiconductor interface, especially their stability and electrical and thermal resistance are important.

Consider a thermoelectric unicouple consisting of p-type and n-type thermoelectric legs of length 'L' and cross-sectional areas 'A_p' and 'A_n', respectively. A temperature gradient, '$\Delta T=T_h - T_c$', is applied between its hot and cold ends. Hot side of the legs is connected by a metallic electrode while a load of resistance 'R_L' is applied across the cold ends of the unicouple. The internal resistances are 'R_p' for the p-type leg and 'R_n' for the n-type leg. The total Seebeck coefficient, 'S', of the unicouple is the sum of the magnitudes of the Seebeck coefficients, 'α_p' and 'α_n', respectively of the p- and n-type legs, i.e.:

$$S = |\alpha_p| + |\alpha_n|.$$

Similarly, the total internal electrical resistance, 'R_i', is the sum:

$$R_i = R_p + R_n = L\left(\frac{1}{\sigma_p A_p} + \frac{1}{\sigma_n A_n}\right)$$

and the total internal thermal conduction, 'K_i', is:

$$K_i = (\kappa_p A_p + \kappa_n A_n)/L$$

where 'κ_p, σ_p' and 'κ_n, σ_n' are the thermal and electrical conductivities of the p- and n-type legs, respectively.

In real applications, heat is lost to the environment due to convection and radiation. If we consider the ideal case, with no heat loss, no contact resistances and constant value of Seebeck coefficient along the legs, the emf (electromotive force) or the open circuit voltage is:

$$\Delta V = S\Delta T;$$

and the current flowing through the load is:

$$I = \frac{S\Delta T}{R_i + R_L}.$$

The power delivered to the load is:

$$P = I^2 R_L = \left(\frac{S\Delta T}{R_i + R_L}\right)^2 R_L.$$

The total heat transfer from the hot side, 'q_h', is a sum of conductive heat transfer and the Peltier cooling associated with the current flow:

$q_h = K_i\Delta T + ST_h$.

The efficiency of the unicouple is, therefore,

$$\eta = \frac{P}{q_h} = \left(\frac{S\Delta T}{R_i + R_L}\right)^2 \frac{R_L}{K_i\Delta T + ST_h}.$$

According to the maximum power transfer theorem, the output power reaches its maximum when '$R_L = R_i$', but the efficiency is higher if '$R_L > R_i$', because a higher amount of source power would be consumed by the load.

The maximum efficiency of a thermoelectric device is defined in terms of the dimensionless figure of merit for the modules, 'ZT', as:

$$\eta_{max} = \eta_c \times \left[\frac{(ZT+1)^{1/2}-1}{(ZT+1)^{1/2}+\frac{T_c}{T_h}}\right] \qquad (1.3)$$

Where, '$\eta_c = \frac{\Delta T}{T_h}$' is the Carnot efficiency and, '$ZT = \frac{S^2T}{R_iK_i}$'.

If we incorporate the thermal and electrical contact resistances, 'K_c' and 'R_c', and the total thermal and electrical resistances, 'K' and 'R', can be defined as $K = K_i\left(1 + \frac{2K_i}{K_c}\right)^{-1}$ and $R=R_i+2R_c$ [33], and the device figure of merit is: $ZT = \frac{S^2T}{RK}$.

The electrical resistance is also affected by the Schottky barrier between the metal and thermoelectric semiconductor, but the major part of thermal and electrical contact resistances greatly depends on the quality of joining. If the quality of the joint is not good enough, the cold side of the thermoelectric legs will not be as cold as the cold side of the device and the hot side of the device will also lose heat at the interface due to poor conduction.

The electrical and thermal contact resistances are quantified in terms of area specific contact resistances, i.e. $\rho_c = R_cA$ and $\kappa_c = K_c/A$. A joint with contact resistance lower than 10% of the total resistance is considered to be a good contact. Therefore, for better performance, the length of the leg should be more than 5mm [34].

1.3 Diffusion in solids

Diffusion is the net movement of molecules or atoms from a region of high concentration to a region of low concentration, resulting in a uniform dissolution. Concentration gradient is the main driving force behind this phenomenon. It is different from convection in that it does not involve bulk movement of particles. A classic example of diffusion is dissolution of salt in water. Diffusion takes place in all forms of matter; here we consider the case of solids. In addition to concentration gradient, other factors also play their role, like temperature, stress, solubility, defects, etc. Diffusion is an isotropic process, i.e. it does not have a preferred direction. However, if the material has anisotropy, e.g. non-cubic lattice, the diffusion can be different in different directions. Diffusion in solids takes place when a solid gets in contact with some other solid, liquid or gas; or when there are inhomogeneities within the solid itself such that annealing has to be performed and atoms diffuse to regions of low concentrations in order to reduce the gradients. The phenomenological description of diffusion processes, still valid today to a great extent, was given by Fick in 1855.

Fick's first law relates the diffusive flux of a concentration to spatial gradient of the concentration in a steady state, as:

$$j = -D\frac{\partial C}{\partial x} \qquad (1.4)$$

where 'j' is the mass flux (with dimensions of $ML^{-2}T^{-1}$), 'D' is the diffusivity (with dimensions of L^2T^{-1}), 'C' is the concentration (with dimensions of ML^{-3}) and 'x' is the measure of length. Equation (1.4) is Fick's first law.

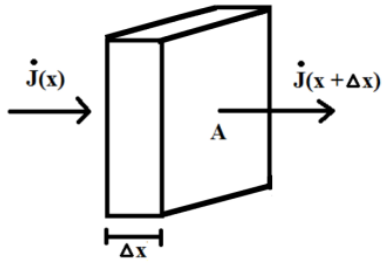

Figure 1.4: Mass fluxes in and out of a volume V = A·Δx.

Fick's second law describes with the change in concentration as a result of diffusion with respect to time. It can be derived be considering the mass balance. The change in concentration per unit time in a volume 'V = A·Δx' equals the sum of the diffusion fluxes in and out of the volume times the area:

$$\frac{\partial M_{total}}{\partial t} = \frac{\partial M_{in}}{\partial t} - \frac{\partial M_{out}}{\partial t}$$

$$V\frac{\partial C}{\partial t} = A \cdot [j(x) - j(x + \Delta x)]$$

$$\frac{\partial C}{\partial t} = -[j(x + \Delta x) - j(x)]/\Delta x$$

for infinitesimal length, 'Δx→0';

$$\frac{\partial C}{\partial t} = -\frac{\partial j}{\partial x} \qquad (1.5)$$

inserting equation (1.4) in (1.5),

$$\frac{\partial C}{\partial t} = D\frac{\partial^2 C}{\partial x^2}. \qquad (1.6)$$

Equation (1.6) is Fick's second law for one dimensional case, with constant diffusivity, 'D'. This is a continuity equation corresponding to the conservation of mass. In three dimensions, Fick's second law becomes:

$$\frac{\partial C}{\partial t} = D\left(\frac{\partial^2 C}{\partial x^2} + \frac{\partial^2 C}{\partial y^2} + \frac{\partial^2 C}{\partial z^2}\right). \qquad (1.7)$$

If the system involves other fluxes too, then equation (1.4) is not sufficient anymore and other fluxes also need to be incorporated in equation (1.7). If the diffusion co-efficient is not constant in all directions, then equation (1.7) becomes:

$$\frac{\partial \mathrm{C}}{\partial \mathrm{t}} = \boldsymbol{\nabla} \cdot (\mathrm{D}\boldsymbol{\nabla}\mathrm{C}) \qquad (1.8)$$

If the diffusion co-efficient varies with position such that, D = D(x), equation (1.6) becomes:

$$\frac{\partial \mathrm{C}}{\partial \mathrm{t}} = \frac{\partial}{\partial \mathrm{x}}\left(\mathrm{D}\frac{\partial \mathrm{C}}{\partial \mathrm{x}}\right) = \frac{\partial \mathrm{D}}{\partial \mathrm{x}}\frac{\partial \mathrm{C}}{\partial \mathrm{x}} + \mathrm{D}\frac{\partial^2 \mathrm{C}}{\partial x^2}. \qquad (1.9)$$

There can be many reasons behind this dependence. For example, the diffusion coefficient may depend on concentration which is varying as the process goes, or system is subjected to a temperature gradient, and so on and so forth. Similarly, if an electrical potential or stress makes the ions or atoms move in a certain preferred direction, we will need to modify the flux equation. Different methods have been developed to solve these problems numerically, using data obtained by experimental measurements[35].

1.4 Alloys and phase diagrams

In chemistry, a region of a material with a homogeneous atomic structure is called a phase. The making of alloys and chemical phases is one of the most important phenomena that shape the thermal history of thermoelectric materials. When thermoelectric materials are put to operation, their microstructure and properties evolve and the knowledge of phase transitions becomes crucial.

A metallic alloy is a chemical mixture of a metal and one or more other metals or non-metals. A binary alloy is made up of two chemical elements, a ternary alloy contains three and a quaternary alloy has for constituents. Alloys are defined by giving the molar concentrations of their components or their chemical formulae. An ideal solid solution is formed when elements are dissolved completely and homogeneously in a solid matrix. In all alloys, there is one principle element to which other elements are added (e.g. aluminum alloys have Al as principle constituent). In this section, we will consider the simple case of binary alloys. When a binary alloy solidifies, its microstructure corresponds to either a solid solution or two separate solid solutions, or a chemical compound embedded in a solid solution.

For a given alloy composition of volume, ‘V’, at a constant temperature, ‘T’, and pressure, ‘P’, the Gibbs free energy, ‘G’, is defined as:

$$\mathrm{G} = \mathrm{U} + \mathrm{PV} - \mathrm{TS} = \mathrm{H} - \mathrm{TS} \qquad (1.10)$$

where ‘U’ is the internal energy, ‘S’ is the entropy and ‘H’ is the enthalpy. Each mixture has a free energy, and the state with the lowest free energy is the one that forms at thermodynamic equilibrium. The pressure term is important in sintering processes that involve high pressure, e.g. formation of Diamond under high pressure deep inside the earth. Entropy also becomes important in ordered systems, e.g. in the case of superlattices, like the Au-Cu alloy, where different kinds of atoms occupy definite geometrical positions instead of diffusing randomly. Generally, in the solid state, pressure has a negligible contribution to the energetics of the system and therefore it can be ignored. Entropy is also very small for most solids as they have a regular order in the form of lattice structure. Therefore, the material state of most alloys can be described by the composition and temperature only. The two dimensional plots showing variation in equilibrium composition with respect to temperature are called “phase diagrams”.

In the case of pure substances, the melting point is a unique temperature at which the substance changes from solid state to the liquid state. However, in the case of alloys, both the solid and liquid states may coexist over a range of temperature. Below the lower end of this range, the alloy is all solid; and above the upper end of this range, the alloy has been molten completely. These are called the "solidus" and "liquidus" temperatures. Consider the phase diagram of an interesting thermoelectric alloy, the Cu-Ni system, in figure 1.5.

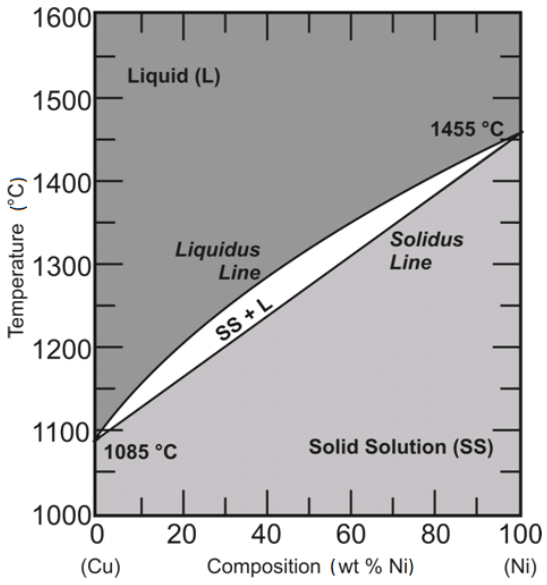

Figure 1.5: Phase diagram of Cu-Ni alloy[36].

We can read from the phase diagram that the pure Cu has a unique melting point of 1085 ^{o}C and pure Ni has a unique melting temperature of 1455 ^{o}C, but all the alloying compositions have a region of solid micro-particles mixed in a liquid. Here the solid solution exists for all compositions of Cu-Ni alloy. To understand the solidification of a certain composition, we consider the example of Cu-60Ni, i.e. the solid solution with 60% Ni.

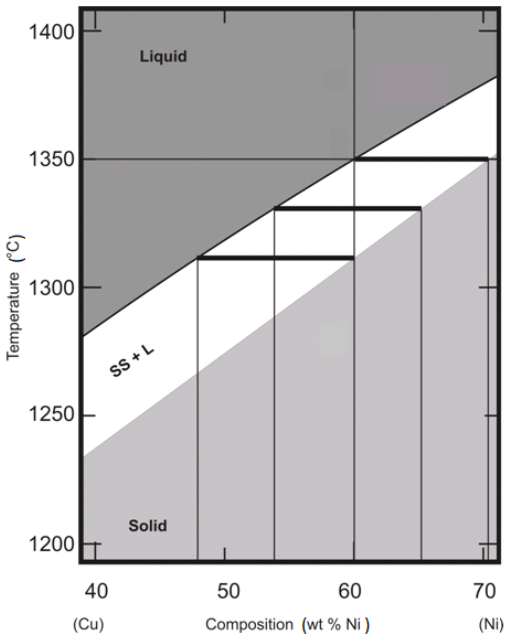

Figure 1.6: Solidification of Cu-60Ni alloy[36].

As shown in figure 1.6, the alloy is completely molten into liquid phase above 1350°C, with a perfect composition of 60% Ni and 40% Cu. As we cool down and reach this point, the alloy starts to solidify. However, looking at the 1350°C point on the solidus line, we learn that the first micrograins to form are those with 70% Ni. When we cool down further, we see that the composition of the liquid is getting richer in Cu content. At point 1330°C the new micrograins have a composition of 65% Ni. The content of Ni in liquid has reduced to 54%. At 1310°C, the final solidification takes place and the content of Ni has dropped down to 48%. In the solid phase, the composition of the alloy is not homogeneous, but has the same lattice structure. This alloy will undergo internal diffusion to achieve homogeneity.

The Cu-Ni solid solution is "single-phase". It is not further divided into other phases, which means that the atomic structure does not change with composition. In more complex systems, this shall change. Usually there is a "solubility limit" for every phase and the principle element cannot dissolve the other substance beyond that limit. The lines separating different phases in the solid state are called "solvus boundaries".

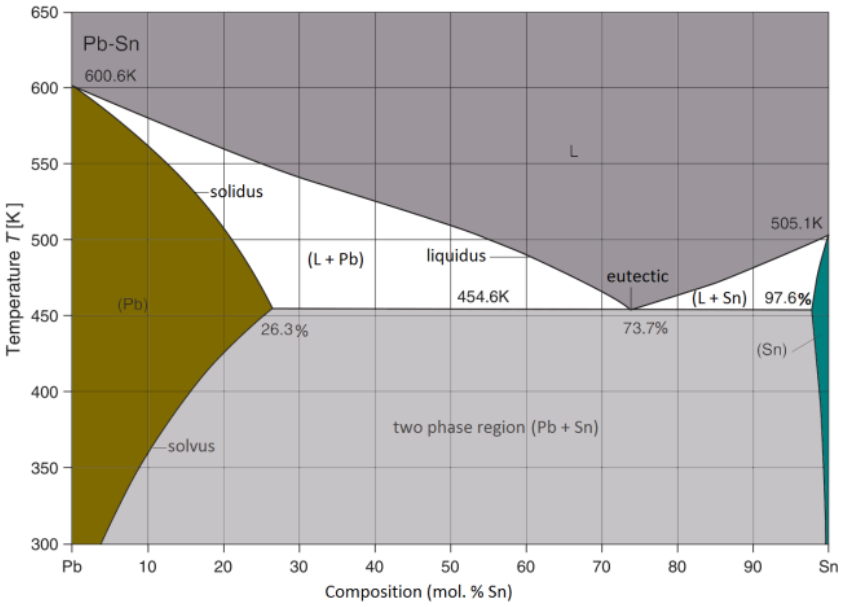

Figure 1.7: Phase diagram of Pb-Sn alloy[37].

Figure 1.7 presents the Pb-Sn phase diagram. In the solid state, there are two "single-phase" regions in this phase diagram, on the left is Pb-rich region and on the right is Sn-rich region. In between them is a "two-phase" region which is a mixture of solid solutions of Pb and Sn. Any point in two phase region corresponds to a weighted mixture of the single phases existing at that particular temperature on the solvus line. All three regions are separated by solvus lines. Note that the solubility of pure substances is quite low. Especially on the right side of the phase diagram, a very narrow Sn-rich region shows that Sn tends not to dissolve in Pb. The same is the case for Ni in Zn[38]. The points where the solvus and solidus lines match is the point of maximum solubility. These are on 26.3 mol.%Sn for Pb in Sb and 97.6 mol.%Sn for Sn in Pb, at 454.6K temperature.

Now consider the point where the two liquidus lines match. This common lower limit of two liquidus lines is called the "eutectic point". At this composition and temperature, like for the melting point of a pure solid, the solid and liquid phases can coexist. Brazing and soldering alloys are preferred to have eutectic or near-eutectic compositions.

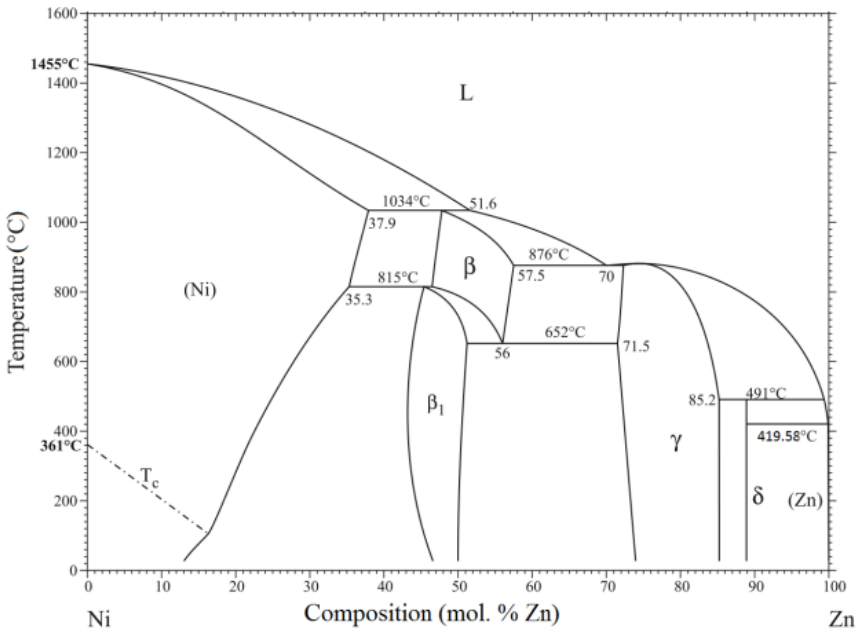

Figure 1.8: Phase diagram of Ni-Zn alloy[39].

In many cases, chemical reactions take place and new compounds form between the alloying elements. These are called intermetallic compounds, if the reactants are metals. These are single phases of fixed composition, distinct crystal structure and unique melting points. Usually they melt at higher temperature due to thermodynamic stability. As an example, have a look at the phase diagram of Ni-Zn system in figure 1.8. This diagram has many phases in the solid region. The crystal structures of different phases in Ni-Zn phase diagram are given in Table 1.1.

Phase	Composition (mol.% Zn)	Space group	Prototype
(Ni)	0-37.9	$Fm\bar{3}m$	Cu
β	46.5-57.5	$Pm\bar{3}m$	CsCl
β_1	43-51.2	P4/mmm	γCuTi
γ	71.5-85.2	$I\bar{4}3m$	Cu_5Zn_8
δ	88.9	C12/m1	…….
(Zn)	100	$P6_3/mmc$	Mg

Table 1.1: Crystal structures in Ni-Zn system[39].

1.5 Joining mechanisms

The making of stable and low resistance contacts between thermoelectric legs and metallic electrodes is as crucial as the stability and performance of the thermoelectric material itself. The contact layers between the thermoelectric legs and metallic electrodes need to have good electrical and thermal conductivities and reasonable mechanical strength. Thermoelectric devices operate at high temperature. Therefor a good understanding of the bonding mechanisms is also essential. There is a set of macroscopic and microscopic properties and mechanisms that govern this bonding. First and foremost is the thermal expansion coefficient: the parts of a system, that is supposed to be subjected to thermal gradients, need to have

compatible coefficients of thermal expansion such that the joints do not break up during the process due to accumulation of thermal stresses. Then there are bonding mechanisms. Bonding between two surfaces might result from mechanical interlocking whereby a molten fluid fills the pores on the surfaces and holds them together upon cooling. It can also have a chemical dimension, i.e. it might result from formation of ionic or metallic bonds. Interatomic forces like van der Waals interaction might also play their part in holding the two surfaces together. Another important mechanism is diffusion: atoms or micro-grains from one material can transfer to the other, resulting in a good adhesion of the surfaces. This might also involve co-sintering when subjected to heat and pressure. Crystallographic matchup is also important as similarly oriented planes and matching lattice constants make stronger bonds, but since thermoelectric materials are mostly poly-crystalline, it does not play a significant role here.

The joining processes are accompanied by cleaning mechanisms, application of heat and pressure. Cleaning mechanisms remove the oxidation layers and contaminants from the surfaces, in order to make intimate contact possible. The choice of cleaning mechanism depends on the hardness of oxides (e.g. 1800 HV for Al_2O_3 and 160 HV for Cu_2O, while harnesses of Al and Cu are 15 HV and 40 HV respectively [40]) and the nature of the contaminants (e.g. organic contaminants can be removed with acetone). Strength of the joint is directly proportional to the actual bond area. Heat and pressure help reduce the yield strength of the base materials and permit plastic deformation to occur, that results in joining. It is important to ensure homogeneity of heat and pressure. Pressure can rupture the oxide layer on the surface and heat can make the oxide particles dissolve in metal matrix. Pressure and heat also make the diffusion and chemical reactions occur faster. After the process of bond formation, the recrystallization and growth of grains and realignment of dislocations occurs at the interface. This stabilization and homogenization of interface happens at lower temperatures and longer times compared to the bonding process.

Now we present an overview of mechanisms adopted to connect thermoelectric materials to metallic electrodes:

1.5.1 Soldering and brazing

Soldering and brazing is joining of two surfaces by molten filler, without melting the base materials. These fillers are usually metallic alloys, characterized by their solidus and liquidus temperatures (see figure 4). By convention, if the filler melts below 450 ^{o}C, it is called a solder and the process is called soldering; above this temperature, the process is called brazing.

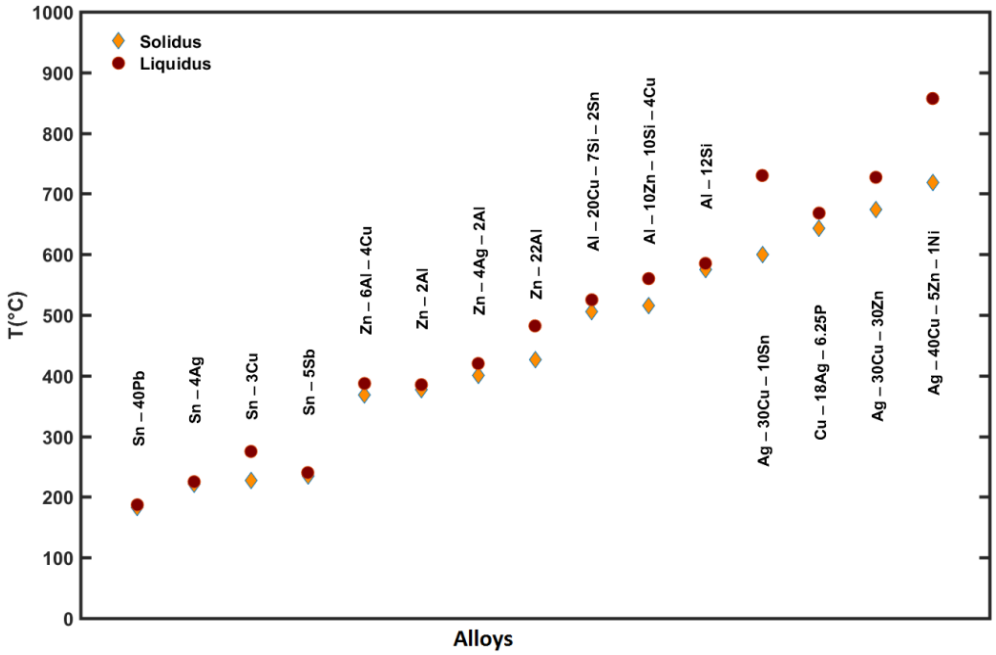

Figure 1.9: An overview of the solidus and liquidus temperatures of some famous fillers in the relevant temperature range [41][42][43][44][45][46].

The underlying phenomenon in this process is called wetting: the filler fluid penetrates between the base materials by capillary force. Wettability depends on many physical properties, i.e. composition of the filler and the base materials, flux, temperature, microstructure and condition of the surface, atmosphere, etc. The major obstacle against wetting is surface oxidation and every soldering or brazing process requires a removal or breakdown of the oxide layer. Therefore, the first step is to apply fluxes or polishing to remove the oxidation layer as a precursor to wetting.

The process of wetting is quantified by the following Young's equation[47]:

$$\gamma_{ls} = \gamma_{sf} - \gamma_{lf}\cos\theta \qquad (1.11)$$

where 'γ_{ls}' is the interface tension between the melt and the surface of the base material, 'γ_{sf}' denotes the interface tension between the flux and the solid base material, 'γ_{lf}' is the interface tension between the melt and the flux and 'θ' is the contact angle.

The metallurgical reaction of the melt and base material starts after wetting and results in formation of a reaction layer or the intermetallic compounds. During this process, base material dissolves into the melt, and it is more evident when melt is an alloy of the base material. This dissolution can be quantified with the help of following equation[47]:

$$\frac{dC}{dt} = K\frac{A}{V}(C_s - C) \qquad (1.12)$$

Here 'C' is the concentration of the solute of base material and the melt after reaction time 't', 'K' is the proportionality constant, 'A' is the area of contact between the base and the melt, and 'V' is the volume of the melt. 'C_s' is the saturation limit of 'C' which rises with increasing temperature. Since the formation of intermetallic compounds may damage the excellent properties of our materials, choice of an optimum temperature and time is crucial. In the worst case, the filler may completely penetrate into the base materials which can

damage the joint quality as well. This phenomenon becomes very important when it comes to thermoelectric devices that operate at high temperatures for long times. Therefore, it is better to have a look at the phase diagrams of possible alloy systems and choose such filler that does not react fast with the base material. The growth rate of intermetallic compounds can also be suppressed by adding a buffer layer. However, addition of buffer layer may come as a compromise on the joint quality. Another factor is the microstructure of the base material, the filler penetrates through grain boundaries and this is fast in the case of materials with small grain size.

Use of soldering/brazing as joining mechanism is an old practice in thermoelectric technology. Weinstein et al.[48] successfully bonded p-type PbTe thermoelectric legs to pure iron electrode by using SnTe as braze alloy. The process was completed in two stages: first a layer of SnTe powder was kept over Iron electrode at 850 ^{o}C for 1 hour to let it melt and wet the surface of the electrode, and then, at a lower temperature of 808 ^{o}C the SnTe coated surface of the electrode was pressed on the thermoelectric leg for 2-4 minutes. The bond was observed to be strong and contact resistance was measured to be ~10μΩcm^2 for carefully prepared joints.

A similar but isothermal joining process, called 'solid-liquid interdiffusion bonding'[49], involves a thin layer (few microns) of filler, preferably having a eutectic composition so that it melts thoroughly at the eutectic temperature. After the filler melts, the joint is kept at constant temperature for long enough time such that the melting point of the filler increases beyond this temperature due to dissolution of base materials. As a result, the filler is fully consumed and the interface solidifies at constant temperature which often results in homogeneous joint microstructure. In this process, the formation of intermetallic layer is desirable and, because of the small volume of the melt, this layer does not grow too much to damage the quality of materials. This process can be described by Fick's equation of mass transfer:

$$(C_L - C_S) \cdot \frac{dX(t)}{dt} = D_S \cdot \frac{\partial}{\partial x} C_S - D_L \cdot \frac{\partial}{\partial x} C_L \qquad (1.13)$$

'C_L' and 'C_S' are the liquid and solid concentrations at the interface, 'X(t)' is the position of solid-liquid interface that moves during the process of dissolution, 'D_L' and 'D_S' are the solute diffusivities in the liquid melt and solid base material. Pressure does not affect this process, however, excessive pressure may squeeze so much that some areas do not bond due to lack of filler, hence resulting in porosity. Heating rate also needs to be high enough such that the filler does not diffuse into the base materials before reaching its melting point.

Lin, et al.[50] investigated solid-liquid interdiffusion bonding between Zn_4Sb_3 thermoelectric material and copper. The Zn_4Sb_3 leg was electroplated with Ni and then Ag layer, while the Cu electrode with Ag and Sn layers respectively, with thickness of 4μm each. The Zn_4Sb_3/Ni/Ag/Sn/Ag/Cu assembly was hot-pressed in vacuum over temperatures of 250°C-325°C for 5-30 minutes and a respective set of samples was obtained. Molten Sn reacted with Ag to form Ag_3Sn and Cu_3Sn, resulting in isothermally solidified strong joint. Interstitial Zn from Zn_4Sb_3 diffused into the Ni barrier layer to form γ - Ni_5Zn_{21}. Traces of Zn and Sb migration into the Sn layer were also identified.

1.5.2 Diffusion bonding

Diffusion bonding is a joining process whereby two clean solid surfaces bond at atomic level as a result of local plastic deformation under elevated temperature and moderate pressure for relatively long time[51]. The mechanism of this process can be thought of as a sintering process. Both the materials are heated upto ~ 50-70% of their melting point which results in interdiffusion of the grains of the two surfaces and formation of new microstructure at the interface. This process completes in two stages. When the two surfaces come close, due to the inevitable surface roughness, the first contact is made by the asperities. Hence the pressure at those grains is very high, resulting in breaking up of the asperities and microplastic deformation. This stage completes when, as a result of increasing contact area, the local stress becomes less than the yield strength of the material. Still the bonding has only occurred at 10% of the area. Now the second stage kicks in. Thermally activated sintering mechanism leads to elimination of voids and recrystallization of the interface. This method usually produces joints of very high quality but it comes with the limitation of high temperature and long time. Weinstein et al.[48] bonded n-type PbTe thermoelectric legs with pure iron by interdiffusion mechanism at 858 ^{o}C for 20-30 minutes, a temperature below PbTe-Fe eutectic. The joint was reported to be strong enough with low contact resistance (~10$\mu\Omega cm^2$).

1.5.3 Co-sintering

Sintering is a process of heating and pressing of a powder in order to impart strength and integrity. The heat and pressure bind micrograins of the powder together to reach solidification, without decomposing or melting them. Spark plasma sintering (SPS) is an ultra-fast sintering process which involves high electrical current and uniaxial pressure. The heat comes from localized Joule heating at the boundaries of the micrograins. This one-step sintering is not only cost effective, but it also helps preserve the phonon-glass characteristics of thermoelectric materials. Recently this method is also being applied to sinter powders of thermoelectrics together with electrodes. Sintering involves three stages:

(1) Evaporation and condensation: At first stage the micrograins start to form necks. The mass transfer from the areas of high curvature to the areas of low curvature improves the contact between the grains and increases the strength. As more times passes, the contact area increases and the material becomes stronger. If the starting powder is fine enough, the mass transfer would be faster and the process will take lesser time. The temperature has to be optimally chosen so that while one achieves fast enough mass transfer, the solid phase of the micrograins and chemical composition are preserved. This requires knowledge of thermal phase transitions in the material.

(2) Diffusion by vacancy: In the second stage, the material starts to shrink as necking starts to push the pores from regions of high density to the regions of low density. Mass diffusion within micrograins starts to maximize the contact area. A network of isolated pores is formed.

(3) Viscus flow: This last and final stage involves further densification and pore elimination. Due to the applied pressure and heat, the pores keep on getting smaller and smaller until a steady state is reached where the material can no longer push into them.

Liu et al.[52] co-sintered layers of Ni with p-type $Bi_{0.4}Sb_{1.6}Te_3$ and n-type $Bi_2Te_{2.7}Se_{0.3}$ thermoelectric materials using a hot-pressing method. The bonding strengths were ~30MPa for p-type and ~20MPa for n-type samples. Although the contact resistance for p-type

samples was less than 1 $\mu\Omega cm^2$, it was very large for n-type samples (210 $\mu\Omega cm^2$). In the n-type samples, significant diffusion of Te into the electrode and Ni into the thermoelectric material was observed. It was concluded that the diffusion of Ni into the thermoelectric material damages the electrical conductivity, because it changed the stoichiometry of the material in the vicinity of the interface such that a p-type region was developed.

Kraemer et al.[53] sintered powders of silver and $MgAg_{0.965}Ni_{0.005}Sb_{0.99}$ thermoelectric material with spark plasma sintering method. A precise amount of thermoelectric powder was sandwiched between silver powders inside a graphite die and SPS sintered at 300 ^{o}C to obtain ~5mm long leg with ~0.25-0.35 mm thick electrodes. Silver was chosen as an electrode because it's thermal expansion coefficient ($19{\cdot}5\times10^{-6}/^{o}C$) matches with that of $MgAg_{0.965}Ni_{0.005}Sb_{0.99}$ ($20\times10^{-6}/^{o}C$). The other reason for this choice was that silver being one of the elements constituting the thermoelectric material, will have a small concentration gradient for diffusion towards the material. The joining resulted in a well-defined interface, and little interdiffusion of elements with no significant effect on contact resistance was observed.

1.6 Electronic structure of contacts

The metal-semiconductor contact can either be Shottky or Ohmic, depending on the IV characteristics. An ohmic contact is the one that has a negligible potential drop across the metal-semiconductor junction. An ideal Shottky contact has rectifying behavior and higher contact resistance. The quality of the electrical contacts is not only determined by the homogeneity and strength of physical bonding, it is also influenced by the electronic band structure across the interface.

Schottky [54] and Mott [55] for the first time formulated the bending of bands in semiconductor side of the metal-semiconductor junction in 1938. The Schottky - Mott rule defines a potential barrier that the charge has to cross to move from one side of the interface to the other. The height of the potential barrier, 'Φ_b', depends on the difference between the work function, 'Φ_m', of the metal and the electron affinity of the semiconductor, 'χ_s', i.e.:

$$\Phi_b = \Phi_m - \chi_s \qquad (1.14)$$

The height of this barrier is usually in the range of 0.5-1.5 eV [56], which is well above the thermal energy of charge carriers in the operating temperature range of Thermoelectrics (~0.05-0.1 eV). When metal-semiconductor joint is formed, charges from one surface flow towards the other to align the Fermi level, 'E_F', in the system. As the metal has large density of carriers, the charge build up at the interface is screened within a few Ångstroms, i.e. the electric field does not even penetrate through the first atomic layer of the metal. In the case of semiconductors, the Debye length is usually of the order of ~ 10 nm.

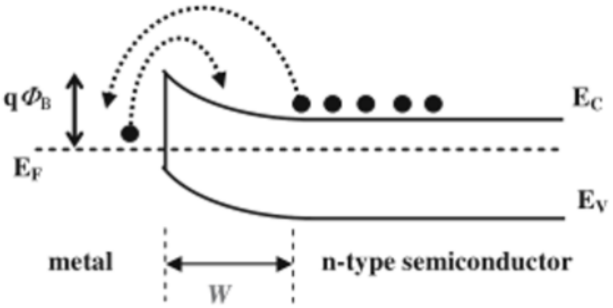

Figure 1.10: Band diagram of a metal semiconductor (n-type) interface according to the Schottky-Mott model. W is the width of the depletion region. Image adapted from [57].

This gives rise to the bending of the conduction and valence bands ('E_C' and 'E_V') in the semiconductor, as shown in figure 1.5. The region with bending bands is called the depletion region; whose width, 'W', is inversely proportional to the carrier concentration in the semiconductor.

However, this is a very simple model and does not describe the complete picture [56]. First and foremost phenomenon that needs to be taken into account is the tunneling effect for degenerate semiconductors. In the case of degenerate semiconductors, the depletion region becomes thinner and therefore charge carriers can tunnel through the potential barrier[58]. This effect reduces the contact resistance. Then there are the interface electronic states that result from the decaying solutions of Schrödinger's equation at the interface (the metal-induced gap states or 'MIGS') and the chemical bonding between the surfaces. These interface states trap charges and pin the Fermi level at the interface[59]. These surface states assist the tunneling of carriers across the interface[60]. There are other mechanisms too that contribute to the electronic conduction across the interface. The inter-diffusion and defects at the interface[61] can cause fluctuations in the interface free energy. These defects are usually related to the synthesis and growth, or growth. Compound semiconductors can have polarization of electronic charge. Interface diploes[62] can provide a layer of charge at the interface that will affect the conduction. Strain due to lattice mismatch[63] also changes the interface energy and influences conduction.

1.7 Motivation and outline

Today, the global energy market is increasing rapidly because of increasing use of modern technology and population growth. According to the estimates of the International Energy Agency, "the world is set to add the equivalent of today's China plus India to its energy demand by 2040" [64]. While it means an increased dependence on fossil fuels, the hydrocarbon reserves are depleting and temperatures across the globe are rising to alarming levels due to CO_2 and CH_4 emission. On the other hand, the use of green technologies, like hydropower, solar energy, wind energy, geothermal energy and thermoelectric energy is on the rise. Thermoelectric technology is one of the areas which have attracted lot of attention due to its technological flexibility. However, one of the major challenges in the path towards a widespread application of this technology to daily life is the stability of thermoelectric devices. Thermoelectric devices usually work at elevated temperatures, and because of that, thermal degradation of the interfaces puts its long term reliability to test.

The overall objective of this thesis is to understand the scientific and technical problems of the interfacial contacts in TEGs and their dynamic behavior at high temperatures, and to develop innovative joining methods for making stable and good TE contacts.

Among many interesting materials for commercial applications [65], we chose to study formation and interface evolution of contacts for ZnSb and $CoSb_3$ based Skutterudites. The first two chapters of this thesis describe the scientific foundations and methods used to carry out this research. Third chapter presents an overview of the structural and thermoelectric properties of the TE materials chosen for this research. While both the Znsb and skutterudites have very different carrier concentrations and bandgaps, the electrical conduction is metallic. In both cases, dramatic reduction of thermal conductivity is achieved by introducing defects in the lattice and exploiting the complexity of the unit cell. The unit cells of these materials have void spaces where weekly bonded impurities can sit and cause the decay of lattice vibrations. This phenomenon was further explored by calculating the lattice contribution in thermal conductivities. It was noted that the lattice thermal conductivities of both the materials are very small. Later in this chapter, unpublished results on the joining experiments carried out on Crofer 22 APU electrode for ZnSb material are presented. Main results of the thesis are presented through 04 scientific papers, of which 03 have been published or accepted for publication and 01 has to be submitted.

The last part of the thesis presents the conclusion and outlook followed by a list of manuscripts in appendices that have been published or are in the process of publishing. Appendix 1 presents the initial results for the solder free joining method. This joining method addresses the two-fold problem of deterioration of both the TE material and the metallic electrode, by introducing a very thin intermetallic layer in the place of solder/braze alloy. This layer being produced by the reaction of the electrode and TE material with a pure metal at a higher temperature, does not grow further at the working temperature. The results from the conventional soldering of ZnSb are partially presented in both appendix 1 and 3. Appendix 2 highlights the migration of Zn atoms from Zn-based solder to the interstitial sites and voids in the ZnSb leg. This migration changes the composition of the ZnSb phase and kills the purpose of the choice of this material. Appendix 4 is based on further extension of the idea of solder free joining method to a skutterudite system. It is noted that for this system, a Cr/Co multilayer is a better interconnecting agent for solder free joining.

Chapter 2: Methods

In this chapter, the main experimental methods used for this research are described.

2.1 Preparation and processing

Following methods were applied to produce the materials and set them up for characterization.

2.1.1 Spark plasma sintering

The spark plasma sintering (SPS) method was used to sinter the pellets of thermoelectric materials used in this research. It is a pulsed electric current sintering technique whereby a high intensity direct current is passed through a fine powder, pressed under uniaxial high pressure, for short time[66].

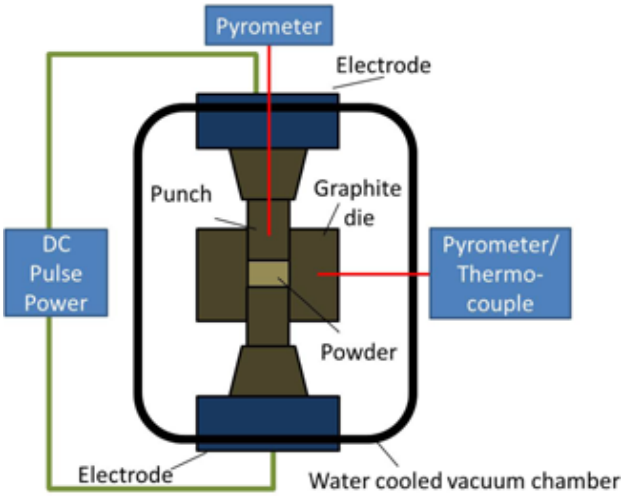

Figure 2.1: Schematic diagram of spark plasma sintering. Image adapted from [66].

The commercially obtained powders were loaded between two graphite punches into a graphite die with graphite foil as the delaminating layer. The powder was first cold-pressed in the die and then the punches were removed one by one and cleaned so that there is no powder on them that could stick with them after sintering.

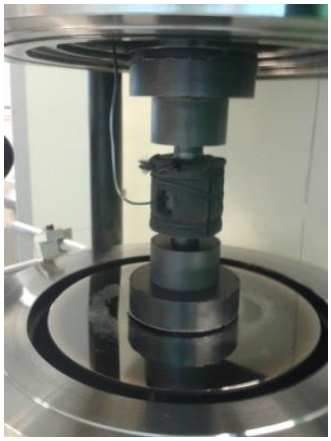

Figure 2.2: Graphite die with powder mounted in SPS system.

The assembly was packed again and loaded into the SPS unit Dr. Sinter 515S (Syntax Inc. Japan). The chamber was closed and pumped, so that water vapors or oxygen would not react

with the material during sintering. First the sintering was performed manually to understand the behavior of material, which is specific to composition and quality of powder. The sintering time, pressure and ramping rate was different for different materials. Once the sintering parameters were explored, a consistent pattern was used to make samples.

2.1.2 Surface treatment

The SPS sintered thermoelectric legs, solders and electrodes were cut to required size using Struers Accutom-5 cutting equipment. In order to remove oxide layers and smoothen their surface, the samples were polished using SiC sandpapers. After polishing, the samples were washed with acetone and ethanol, and dried with nitrogen.

2.1.3 Magnetron sputtering

Magnetron sputtering is a widely used technique to grow thin films on surfaces. The basic principle is the sputtering of target material as a result of ion bombardment, and deposition of those evaporating particles on the surface of substrate. An electrical potential causes the molecules of low pressure gas to ionize and bombard the target that has opposite polarity. In magnetron sputtering, the process is enhanced with the help of a magnetic field, which makes the ions spiral and hence increases their probability of hitting the target. The electrical power supplied to the target can be a DC power in case of conductive target or an RF AC power for an insulating target like oxides.

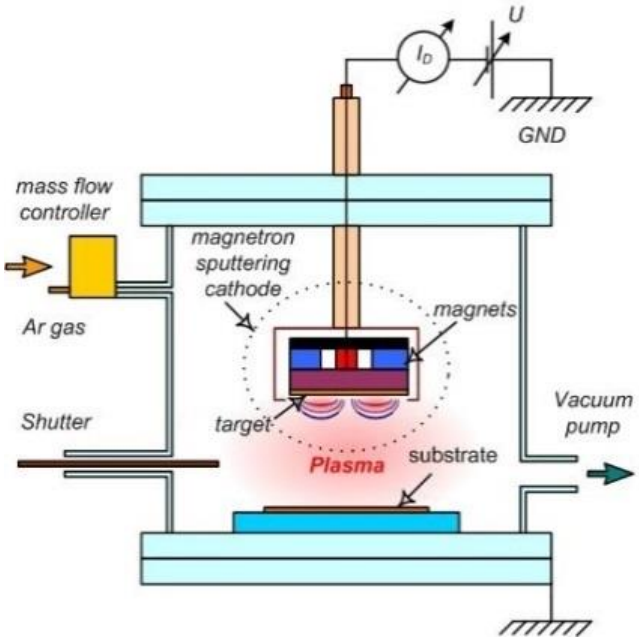

Figure 2.3: Schematic diagram of magnetron sputtering.

A stronger magnet has to be used for magnetic targets, because they might shield the intensity of normal magnets. This technique was used to sputter a few micro-meter thick metal films on thermoelectric substrates. It was a non-reactive sputtering carried out in Argon atmosphere, after establishing vacuum overnight. The sputter rate, or the yield, depends on the material properties of the target, the electrical potential applied, the pressure of plasma gas, and the intensity of the magnet. It was quantified in terms of film thickness and the time taken for deposition, keeping the other parameters unchanged.

2.1.4 Joining

The joining was performed using a simple hot-pressing method in Argon atmosphere. For conventional joining, appropriate solders or braze alloy were used as fillers. Thin sheets of solder were placed between polished and cleaned metallic electrodes and thermoelectric legs and heated under pressure upto its liquidus point.

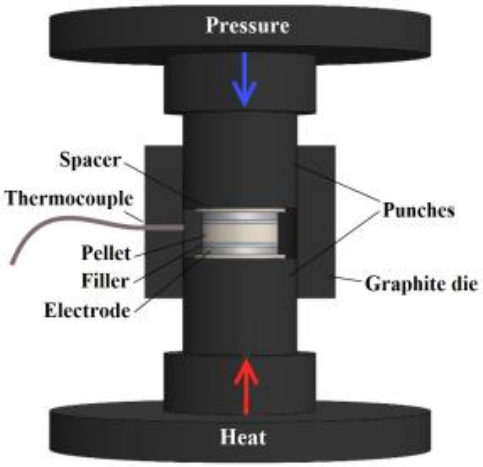

Figure 2.4: Schematic diagram of the joining process.

For solder-free joining, a thick film of pure metal was grown on two opposite surfaces of thermoelectric legs to be used as filler. It was then sandwiched between polished and cleaned metallic electrodes and heated under pressure. The solder and the metallic film were chosen so that they could react and form strong bonds with the thermoelectric material and the electrode.

2.2 Characterization

2.2.1 Thermoelectric properties

Seebeck coefficient and electrical resistivity of the materials were measured on ULVAC-RIKO ZEM3 system. A sample of cylindrical or rectangular cuboid shape is heated upto and stabilized at chosen temperature step inside a furnace, while a heater in the lower block provides a small temperature gradient.

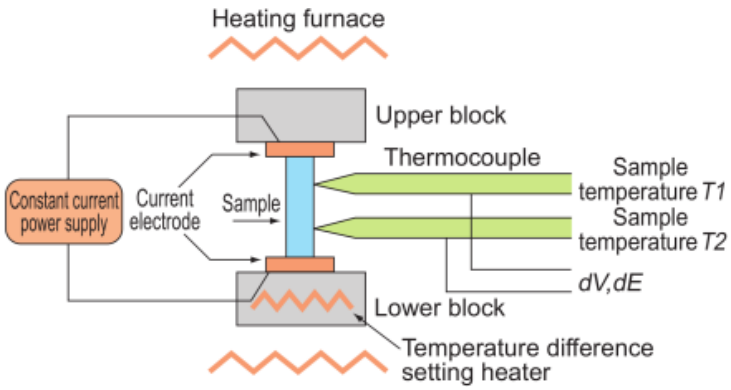

Figure 2.5: Schematic diagram of ULVAC-RIKO ZEM3 system. Image adapted from [67].

This equipment uses a four probe static DC method to measure the electrical resistivity, a constant current is passed through the sample and voltage drop is measured between the wires of the thermocouple. The Seebeck coefficient is obtained by fitting the slope of the voltage

difference dV against the temperature difference dT measured by two thermocouples. The equipment is controlled by computer and data is analyzed by software. The measurement was performed under a low pressure of helium atmosphere, in the temperature range relevant to the materials.

Figure 2.6: ULVAC-RIKO ZEM3 equipment.

2.2.2 Thermal conductivity

Thermal conductivity was measured indirectly with Netzsch's laser flash analysis system LFA 457. In LFA 457 apparatus, three samples can be loaded at once, one of them being the reference sample with known properties. The laser flash analysis works as follows: Laser pulses of controlled energies are shot onto one side of the sample, and the temperature change is monitored on the other side as a function of time. The thermal diffusivity, 'β', of the material is a measure of the time ($\tau_{1/2}$) it takes for the other side of a sample of thickness, 'd', to reach half of the maximum temperature at the side receiving the shot:

$$\beta = 1.38\frac{d^2}{\pi^2\tau_{1/2}} \qquad (2.1)$$

Both faces of thin cuboid samples were sprayed with a graphite spray to coat them with a matt surface of low emissivity to ensure maximum absorption of the laser pulse. Liquid nitrogen was circulated through the laser gun as chiller, so that the laser source could function properly. First the measurement of thermal diffusivity was performed in a purged chamber by heating the samples up to and stabilized at each temperature step. The measured data was then analyzed by the LFA software and both thermal diffusivity, 'β', and specific heat capacity, 'c_p', were estimated with respect to the known properties of the reference sample. The density, 'ρ', of the samples was calculated using Archimedes rule. Thermal conductivity, 'κ', is the product: $\rho\beta c_p$.

Figure 2.7: Netzsch LFA-457 equipment.

2.2.3 Microstructural properties

The microstructural and compositional properties of the samples were observed under a Hitachi TM300 scanning electron microscope (SEM). The equipment is pumped with the help of a diaphragm vacuum pump to achieve a moderate vacuum level. The microscope studies the microstructure of a material by scanning its surface with a focused electron beam. The electron beam is produced thermionically from a tungsten filament. Tungsten has very high melting point, low vapor pressure at high temperature and has very low coefficient of thermal expansion. The electron beam is accelerated by applying a chosen electrostatic potential and focused using electromagnetic lenses.

Figure 2.8: TM3000 tabletop scanning electron microscope with energy dispersive x-ray spectrometer.

TM3000 comes with three beam conditions: the ‘5V’, ‘15V’ and ‘Analysis’ modes. Depending on the image requirements and material specifications, one of these modes is selected. The electron beam penetrates deep into the material and some electrons are scattered back from the nuclei on the lattice points. Because of high energy electrons hitting the atoms, X-rays are also emitted from them, with spectrum of energies corresponding to the electronic

structure of the target atoms. The scattered electrons are of two types: backscattered and secondary electrons. Both kinds of scattered electrons are detected and used to image the surface. Backscattered electrons are produced as a result of elastic scattering and therefore they have high energies, comparable with the energy of the incident beam. They not only come from the vicinity of the surface but also those produced in the deeper volumes manage to reach the detector. Secondary electrons are results of inelastic scattering and have lower energies, therefore only the ones produced in the volume close to the surface manage to escape the surface and are collected by the detector. Backscattered electrons provide better compositional contrast while secondary electrons carry more topographic details and hence the image formed by secondary electrons has better spatial resolution. The Hitachi TM3000 comes with an X-ray energy dispersive spectrometer (EDS) as well, this spectrometer detects the X-rays coming out of the material and hence the chemical composition of the sample can be estimated.

Chapter 3: Selected results and general discussion

3.1 Choice of materials

3.1.1 ZnSb

Zn-Sb system has long been under investigation for thermoelectric applications, due to its high thermoelectric figure of merit, low cost, abundance and non-toxicity [68, 69]. The phonon-glass electron-crystal Zn_4Sb_3 compound semiconductor is one of the best thermoelectric materials because of its low thermal conductivity and degenerate semiconductor-like electronic structure. Snyder et. al. [69] identified that the ideal stoichiometry for this material is $Zn_{13}Sb_{10}$ (see figure 3.2). The small and electropositive Zn atoms were not substituting the large and electronegative Sb sites, instead the Zn sites were only 90% occupied. The rest of the Zn atoms went into interstitial sites. They suggest that Zn-Sb system can be best thought of as a valence compound. The -3 valence Sb(1) atoms have Zn atoms in their 6-nearest neighbor positions at 2.76Å. The -2 valence Sb(2) atoms form Sb-Sb dimers with bond length of 2.82Å, with three Zn(1) atoms at 2.68Å distance. Zn(1) with two electrons available for covalent or ionic bonding to become Zn^{2+}, has four Sb neighbors and one Zn at metallic distance of 2.7Å. In each hexagonal cell of Zn_4Sb_3, there are 18 Sb^{3-} and 12 Sb^{2-} in dimers. To establish valence balance, a total of 39 Zn^{2+} are required, i.e. to form $Zn_{3.9}Sb_3$ compound. As there are only 36 available positions on the main Zn(1) site ($Zn_{3.6}Sb_3$), valence balance dictates that there must be three or more Zn atoms on interstitial Zn sites (more, because complete electron transfer is unlikely for interstitials).

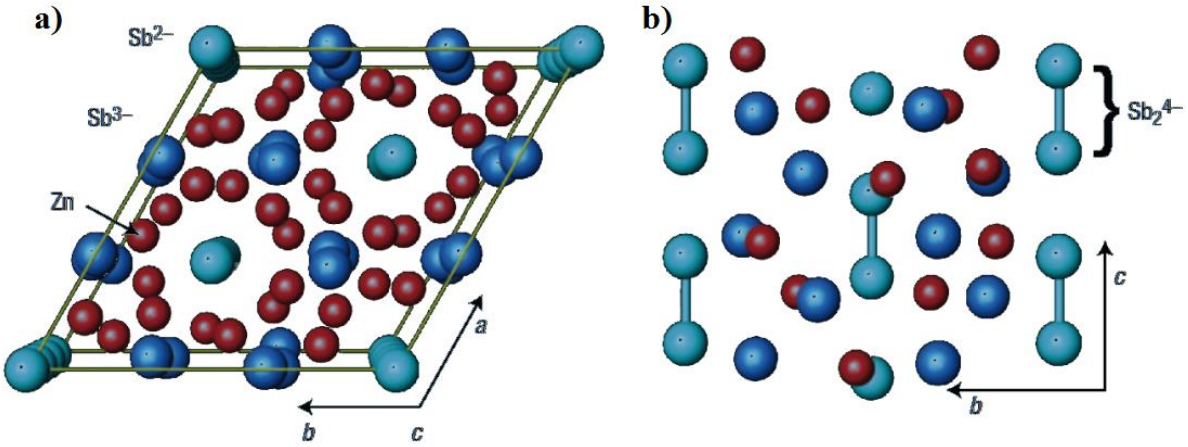

Figure-3.1: The crystal structure of Zn-Sb system without Zn interstitials: a) view from top (c-axis), b) side view showing Sb^{2-} dimers. The Sb^{3-} (dark blue) form distorted hexagonal-closed-packed layers with Sb^{2-} dimers (light blue) in the channels formed by octahedral holes. The red dots are the small Zn atoms. Image adapted from [69].

The understanding of chemistry of this system can give insight into the origins of its excellent thermoelectric properties. The thermal conductivity of Zn_4Sb_3 is like that of an ideal phonon glass, and it is due to the Zn interstitials. The compounds ZnSb and Zn_4Sb_3 have very similar structural features and electronic properties, however, despite its much lower thermal conductivity, Zn_4Sb_3 is not as stable against thermal cycling as ZnSb, and Zn in this system starts to precipitate at the colder end of the leg [26]. Therefore, for long term operation, ZnSb phase is considered to be the better choice. However, because of the complex chemistry of this system, it is difficult to synthesize single phase material[70, 71], and a variety of polymorphs are formed during synthesis. ZnSb phase has orthorhombic crystal structure and an indirect bandgap of 0.5 eV at room temperature and carrier concentration of $\approx 10^{16}cm^{-3}$

[72][73]. Blichfeld et al. studied the structural properties of the SPS sintered ZnSb [74]. The density of the samples was close to the theoretical value of 6.377 g/cm^3. The thermal expansion coefficient of this material is anisotropic, which might cause cracks in a polycrystalline sample. Zn ion migration was also observed, which occurred during sintering along the direction of electrical current. Peaks corresponding to unreacted antimony and zinc were also observed in the PXRD data. The chemical morphology of the material is closely related to the quality of the starting powder and synthesis conditions, like pressure, time and temperature. We studied the contacts and interface evolution for SPS sintered ZnSb, obtained from TEGnology AS, and the results are presented in appendices 1-3.

3.1.2 Filled $CoSb_3$

Pure $CoSb_3$ is a direct bandgap semiconductor with a small bandgap of (0.05-0.22) eV [75]. This material belongs to skutterudite family of compound semiconductors with promising thermoelectric properties. The crystal structure of skutterudites is made up of a cubic lattice with space group $Im\bar{3}$. The unit cell has eight cubic motifs of Co atoms occupying the 8c sites (1/4, 1/4, 1/4), six of which are filled by square planar rectangles of Sb occupying the 24g (0, y, z) sites. The two remaining cubes have void spaces in the unit cell 2a (0, 0, 0) or (1/2, 1/2, 1/2) sites, as shown in figure 3.2 [76]. The electronic band structure of this material is such that it has a very high Seebeck coefficient and low electrical resistivity, but it also has a high thermal conductivity of 6-10 W/m·K [77].

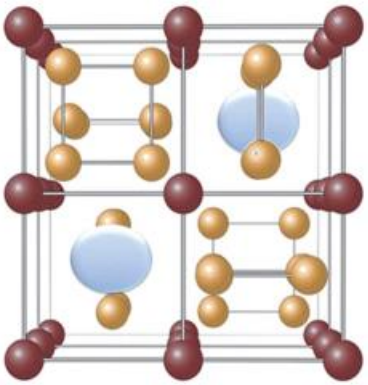

Figure-3.2: The unit cell of $CoSb_3$, the Co atoms are represented by red spheres and Sb by yellow spheres and the void cages by light blue spheres. Image adapted from [76].

Slack [78] proposed that introduction of rattling atoms in voids of skutterudite unit cell can help bring thermal conductivity to reasonably low values. These rattling atoms are supposed to scatter phonons and delay the transport of heat. Since then, many successful attempts have been made and a series of filled skutterudites has been discovered [79]–[81]. In this thesis, the possibility of applying a novel joining method to filled skutterudites commercially obtained from Treibacher Industrie AG is explored. Industrially produced powders of p-type $DD_y(Fe_{1-x}Co_x)_4Sb_{12}$ and n-type $(Mm, Sm)_yCo_4Sb_{12}$ were sintered by Spark plasma sintering method and joined to Crofer 22 APU electrode. The carrier concentration for these materials is reported to be $\approx 10^{20}$ cm^{-3} [82], [83]. The results of the joint formation are presented in appendix 4.

3.1.3 Metallic electrodes

In this research, Ag, Ni and Crofer 22 APU were chosen as electrodes because of their excellent transport characteristics, stability in the mid-to-high temperature range, and abundance. Copper is another widely used electrode due to its excellent transport properties but it was not chosen for this study because it already starts to oxidize at 350 ^{o}C [84]. Crofer 22 APU is a Fe-22Cr based metallic alloy with traces of other elements, i.e.: Mn, C, Si, Cu, Al, S, P, Ti and La. It is widely used for solid oxide fuel cells[85], and it has proved to be corrosion resistant electrode due to formation of a conducting Cr_2O_3 and a $(Mn, Cr)_3O_4$ outer layer in oxidizing environment [86], [87]. This layer is formed due to Cr migration towards the surface of the alloy and reaction with oxygen. It is a low cost and stable electrode, with metallic transport properties and low coefficient of thermal expansion ($10.3\times10^{-6}/^{o}$C at 200 ^{o}C to $12.7\times10^{-6}/^{o}$C at 1000 ^{o}C).

3.2 Thermoelectric properties

The thermoelectric properties of the chosen materials were experimentally measured and a detailed discussion and comparison with literature values follows in appendices 1-4. To understand the phonon-glass nature of these samples, the experimental data needs to be further analyzed. For a good thermoelectric material, thermal conductivity, κ, should be low so as to increase the temperature difference between the hotter and the colder end. Thermal conductivity has two contributions: 1) electronic thermal conductivity (κ_e) which comes from the charge carriers (electrons or holes), and 2) lattice thermal conductivity (κ_l) coming from the lattice vibrations or phonons.

$$\kappa = \kappa_e + \kappa_l. \qquad (3.1)$$

Wiedemann-Franz law relates the electronic contribution to the thermal conductivity as:

$$\kappa_e = LT/\rho, \qquad (3.2)$$

where 'L' is the Lorenz number and 'ρ' is the electrical resistivity. In thermoelectric materials, the lattice thermal conductivity is dominated by acoustic phonons. Lorenz number is constant for metallic systems, but for semiconductors it depends on the electronic band structure. Lorenz number for degenerate semiconductor is defined as [88]:

$$L = \left(\frac{k_B}{q}\right)^2 \left[\frac{3F_2(\eta)}{F_0(\eta)} - \left(\frac{2F_1(\eta)}{F_0(\eta)}\right)^2\right]. \qquad (3.3)$$

Here 'q' is the electronic charge, '$\eta = E_f/k_BT$' is the reduced Fermi level, and $F_i(\eta)$ is the Fermi integral defined as:

$$F_i(\eta) = \int_0^\infty \frac{(E/k_BT)^i}{1+\exp(E/k_BT-\eta)} \qquad (3.4)$$

where 'E_f' denotes the Fermi level of the material, 'E' is the energy of the charge carrier and 'k_B' is the Boltzmann constant. The reduced Fermi level can be calculated from the measured values of Seebeck coefficient, 'α', as:

$$\alpha = \frac{k_B}{q}\left(\frac{2F_1(\eta)}{F_0(\eta)} - \eta\right). \qquad (3.5)$$

Figure 3.3 shows the thermoelectric properties of the ZnSb material used in this research. The Seebeck coefficient is positive in the measured temperature range, which shows p-type conduction. The resistivity increases with increasing temperature, a signature for metallic transport in degenerate semiconductors. Both the electrical resistivity and the Seebeck coefficient reach a maximum around 400 °C. The thermal conductivity is largely contributed by the lattice part. One reason for this could be the lower carrier concentration as compared with other thermoelectric materials. This emphasizes further the importance of phonon scattering in the Zn-Sb system.

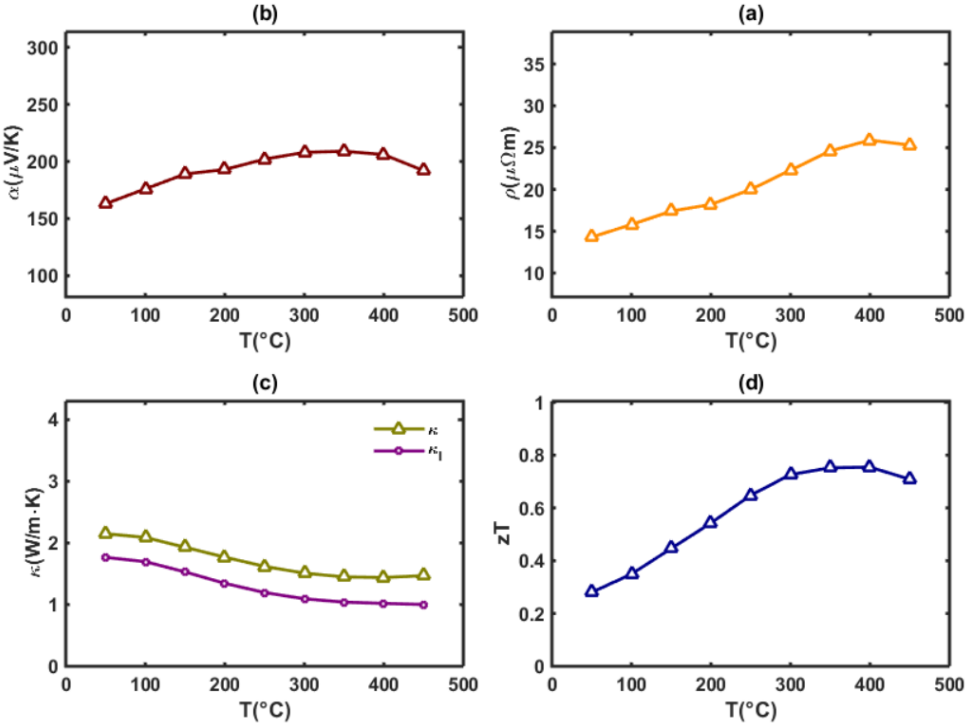

Figure-3.3: Thermoelectric properties of ZnSb.

Figure 3.4 and 3.5 show the thermoelectric properties of the p-type and n-type skutterudites used in this research, respectively. These materials have excellent electrical properties of an ideal thermoelectric, high Seebeck and low electrical resistivity. The high magnitude of Seebeck coefficient observed in skutterudites is attributed to their electronic band structure [75], while the metallic electrical resistivity to the high carrier concentration and the low band gap. The electronic contribution to thermal conductivity is more pronounced in these materials than ZnSb. This is in accordance with the higher carrier concentration in these materials. However, the rattler atoms seem to have played their role in reducing the lattice thermal conductivity, such that the total thermal conductivity became comparable to the thermal conductivities of the state of the art thermoelectric materials[89][90].

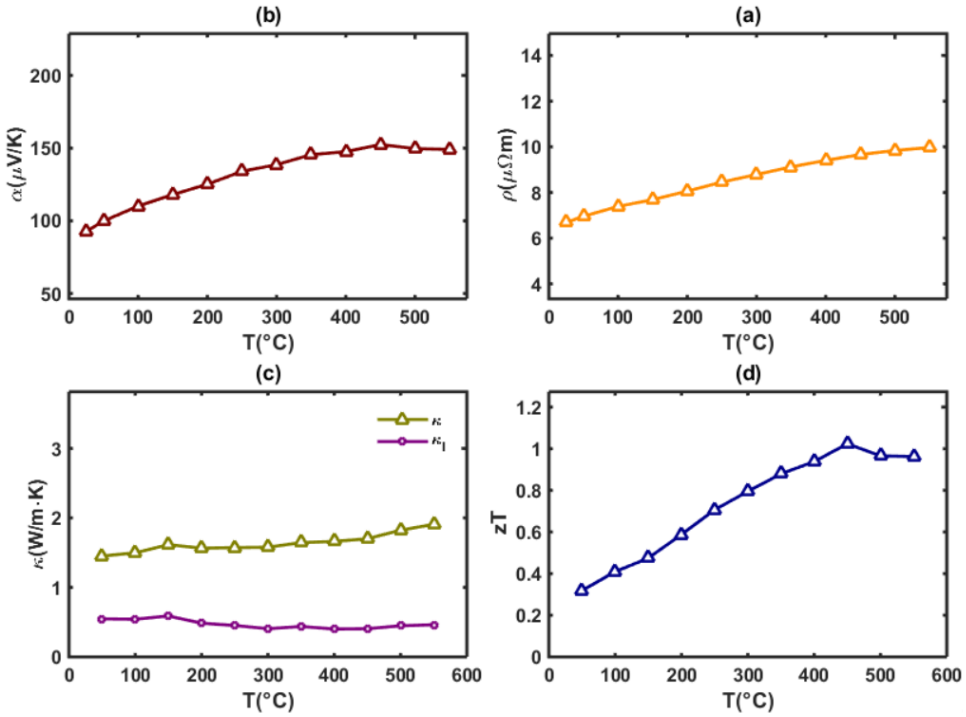

Figure-3.4: Thermoelectric properties of SPS sintered p-type skutterudite legs.

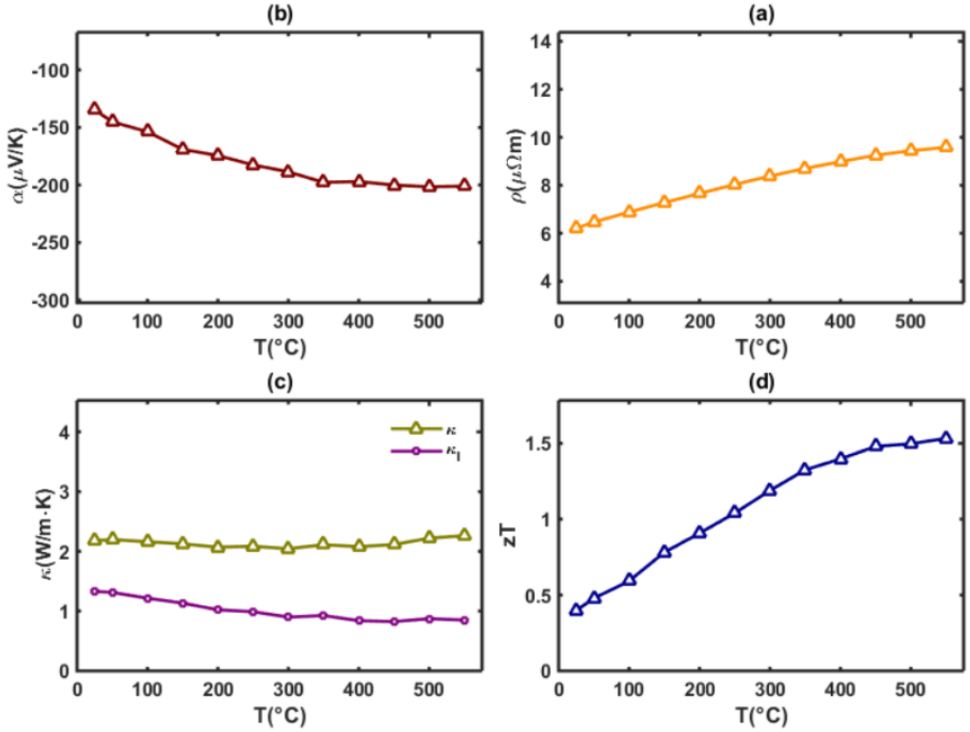

Figure-3.5: Thermoelectric properties of SPS sintered n-type skutterudite legs.

3.3 Joining

Appendices 1-3 contain the detailed discussion about the conventional soldering and a novel solder free joining of ZnSb to Ag and Ni electrodes. Appendix 4 discusses the application of solder free joining method to skutterudites. A stable metallic electrode, Crofer 22 APU, is

proposed for mid temperature thermoelectric applications. Here we discuss the prospects of using this electrode for Zn-Sb system.

3.3.1 Conventional joining

Joining of thermoelectric elements to metallic electrodes using soldering/brazing alloys is an established method for manufacturing thermoelectric devices. ZnSb material performs best around 400 ^{o}C, and hence a suitable solder for conventional joining is the Zn-2Al alloy with solidus temperature of 377 ^{o}C and liquidus temperature of 385 ^{o}C. As pointed out in Appendices 1-3, this solder diffuses deeply to Ag and Ni, common metallic electrodes for this temperature range. This diffusion not only makes it difficult to preserve the excellent properties of electrodes for long time, it can also induce cracks in those electrodes.

In steel industry, Zn has been used as galvanizing agent for long time, to prevent rusting of the surfaces. Fourmentin et al. [91] studied the thermodynamics of the Fe-Zn-Al-Cr system and concluded that the addition of small amount of Al and Cr to the Zn bath at galvanizing temperatures delays the nucleation of brittle Fe-Zn compounds and forms a coating layer of Fe-Al-Zn-Cr alloy. Therefore, Crofer 22 APU electrode was chosen to be soldered to ZnSb using the Zn-2Al alloy. The joining was performed in Argon atmosphere at 400 ^{o}C for 30 minutes under a uniaxial pressure of 3MPa. The surfaces were polished and cleaned before the joining to remove oxidation or contaminant layers. Initially, the assembly was kept at 375 ^{o}C for 30 hours long heat treatment. Later on, to test the long term stability, the samples were kept at 375 ^{o}C for 300 hours. The interface was studied under TM3000 scanning electron microscope.

Figure 3.6 (a) shows the SEM micrograph of the interface between Crofer 22 APU electrode and Zn-2Al solder alloy after initial joining and heat treatment. The interface between the solder and the electrode has no cracks or airgaps, and a relatively thin layer of intermetallic compounds (IMC) is formed. The joining between this solder and ZnSb is discussed in Appendix 2. Figure 3.6 (b) shows the SEM micrograph of the joint after long term testing for 300 hours at 375 ^{o}C. The IMC layer has grown thicker, but this growth is very slow as compared to the other electrodes (Appendices 1-2).

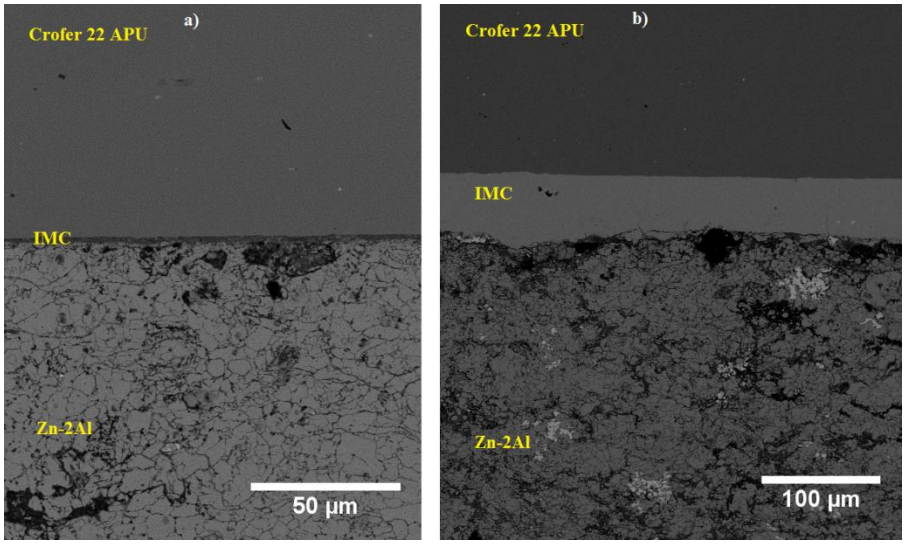

Figure-3.6: a) SEM micrograph of Crofer 22 APU/Zn-2Al interface after joining and initial heat treatment. b) SEM micrograph of Crofer 22 APU/Zn-2Al joint after long term testing.

3.3.2 Solder free joining

Solder free joining is, in essence, a modified diffusion bonding process facilitated by a thin metallic layer between the two surfaces in question. This method achieves good joint formation at lower temperatures than the traditional diffusion bonding temperatures (see section 1.5.2). For solder free joining between Crofer 22 APU and ZnSb, a few microns thick layer of Cr was deposited on a polished and cleaned ZnSb substrate. This surface was then joined with the polished and cleaned surface of Crofer electrode by heating at 450 ^{o}C for 30 minutes under a uniaxial pressure of 3MPa in Argon. For long term testing, this joint was kept at 400C for 100 hours. The interface was studied under TM3000 scanning electron microscope.

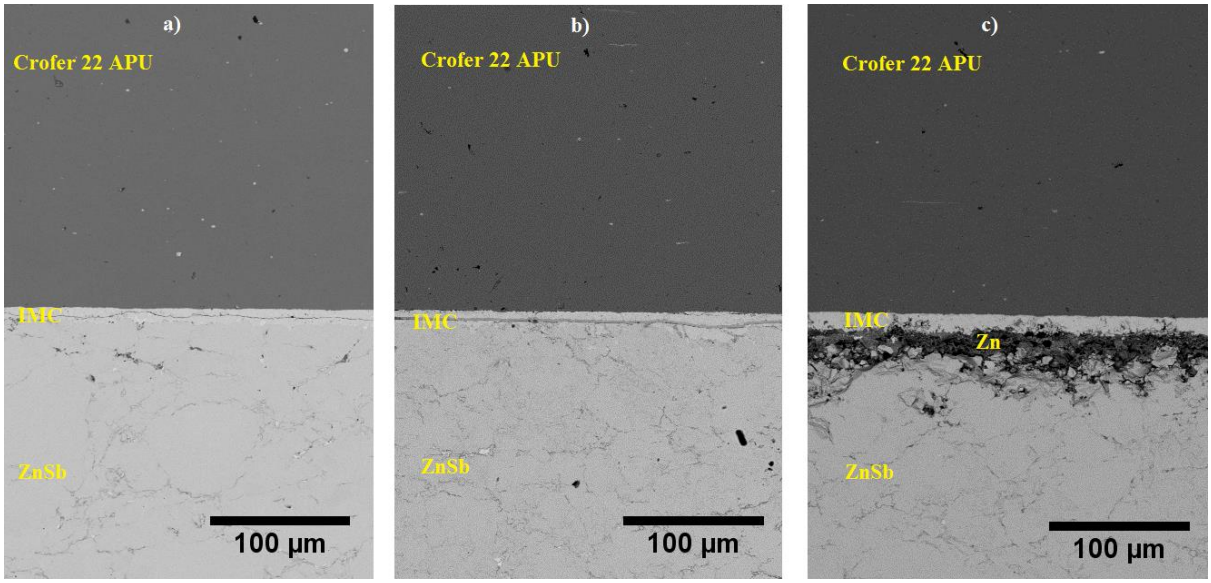

Figure-3.7: a) SEM micrograph of Crofer 22 APU/Cr/ZnSb joint after solder free joining, b) SEM micrograph of the hot side of the joint after 100 hours of heat treatment at 400 ^{o}C, c) SEM micrograph of the colder side of the joint after 100 hours of heat treatment at 400 ^{o}C.

Figure 3.7 (a) shows the SEM micrograph of the interface between Crofer 22 APU electrode and Cr deposited ZnSb after joining. The interface between the solder and the electrode has no cracks or airgaps, and a thin layer of intermetallic compounds (IMC) is formed. Figures 3.7 (b and c) show the SEM micrograph of the joint after long term testing for 100 hours at 400 ^{o}C. The IMC layer has not grown thicker, but Zn has precipitated on the colder side of the leg. This could be the unreacted Zn content that is characteristic to the SPS sintered ZnSb [74]. It has been established that the Zn on interstitial sites of the Zn-Sb system precipitates on the colder end of the leg when subjected to heating [26].

Conclusion and Outlook

This thesis has investigated the stability and interface evolution of contacts between electrodes like Ag, Ni and Crofer 22 APU, and thermoelectric materials like ZnSb and $CoSb_3$ based n-type filled skutterudite. These materials show their best TE performance in the mid to high temperature region (300 °C to 600 °C). The thermoelectric legs were prepared by spark plasma sintering and characterized. The thermoelectric properties show that the filling of voids in the unit cells of the lattice reduces thermal conductivities of these materials sufficiently. However, these void spaces may also enhance the unwanted diffusion of soldering/brazing alloys which are conventionally used to connect the thermoelectric legs to the metallic electrodes.

Zn-Sb material was chosen first, for its low cost, abundance and high thermoelectric performance. The Zn_4Sb_3 phase was ruled out because it is unstable under long operation times. The excess zinc in the 4:3 phase sits on the interstitial sites and these interstitial Zn atoms play the key role in improving the zT of this material by reducing thermal conductivity. However, the very interstitial Zn atoms start to migrate to the colder end when the material is subjected to thermal gradient. This migration results in excess of Zn on the colder side and degrades the performance of the device. However, when conventional soldering was applied to the 1:1 phase, i.e. ZnSb, the soldering alloys available in the desired temperature range were Zn-based alloys: Zn-2Al and S-Bond 400. Ag and Ni were chosen as electrodes because of their excellent transport properties, corrosion resistance in the desired temperature range and comparable coefficients of thermal expansion. It was found that not only zinc diffused into the ZnSb legs, but also it reacted with the Ag and Ni electrodes and formed thick intermetallic layers of $AgZn_3$, Ag_5Zn_8, AgZn, and Ni_5Zn_{21} at the respective interfaces. The problem of Zn diffusion into electrodes was solved by using Crofer 22 APU as electrode. This electrode not only has excellent transport properties and comparable thermal expansion coefficient to ZnSb, but it is also low cost and it resists Zn diffusion due to thermodynamics of the Fe-Zn-Cr-Al system. This electrode was tested for long term stability and after 300 hours of heat treatment at 375 °C, the intermetallic layer at the Crofer 22 APU/Zn-2Al interface was not as thick as the Ni_5Zn_{21} layer on the as-prepared Ni/Zn-2Al joint.

To stop the diffusion of Zn into ZnSb system, buffer layers of Ti and Cr were deposited on the TE legs before joining. This did not stop Zn from diffusing into the TE legs. The puzzle was finally solved by application of an innovative joining method: the thin layers of Cr and Ti were used to assist diffusion bonding between the electrodes and ZnSb. Ag has high solubility in ZnSb and the diffusion joining resulted into Ag electrode being consumed all together, and the buffer layers could not affect the process. However, the scheme was successful for the case of Ni and Crofer 22 APU electrodes. This modified diffusion joining was named solder free joining. The next step was to put this method to long term test. The Cr-assisted joint remained stable for 30 hours, but the Ti-assisted joint was observed to have deteriorated. The joint with Crofer 22 APU electrode was tested for 100 hours and it was observed to be stable. Miraculously, the intermetallic reaction layer did not grow thicker.

The solder free joining method was further extended to the $CoSb_3$ based n-type filled skutterudite. The experiments were performed with single Cr and multi Cr/Co layers. The

bonding was successful, however only the Cr/Co multilayer based joint could pass the 300 hour thermal annealing test at 500 °C.

While this research resulted in the discovery of a reliable solder-free joining method and a low cost and stable electrode for mid to high temperature range, it has opened many questions. First and foremost is the identification of the intermetallic compounds formed at the interface and characterization of their thermal and mechanical properties. This requires a detailed x-ray diffraction study of the thin reaction region. The next step is to measure the transport properties of these intermetallic phases and understand the role they play in electron transfer across the interface. This investigation can be coupled with the measurement of interface potential barrier and simulation of electron transport. A complete picture of both the chemical and electronic landscape needs to be drawn for future development of this joining method.

Bibliography

[1] T. J. Seebeck, “Magnetische Polarisation der Metalle und Erze durch Temperatur-Differenz (Magnetic polarization of metals and ores by temperature differences),” *Abhandlungen der Königlichen Akad. der Wissenschaften zu Berlin*, pp. 265–373, 1822.

[2] H. C. Ørsted, “On some new thermoelectric experiments performed by Baron Fourier and M. Ørsted (1823),” in *Selected Scientific Works of Hans Christian Ørsted*, K. Jelved, A. D. Jackson, and O. Knudsen, Eds. Princeton University Press, 1998, pp. 470–477.

[3] J. C. Peltier, “Nouvelles experiences sur la caoricite des courans electrique,” *Ann. Chim. LVI*, p. 371, 1834.

[4] W. Thomson, “On the dynamical theory of heat. Part V. Thermo-electric currents,” *Trans. R. Soc. Edinburgh*, vol. 21, pp. 123–171, 1854.

[5] W. Thomson, “On a mechanical theory of thermo-electric currents,” *Proc. R. Soc. Edinburgh*, vol. 3, no. 42, pp. 91–98, 1851.

[6] D. Champier, “Thermoelectric generators: A review of applications,” *Energy Convers. Manag.*, vol. 140, pp. 167–181, 2017.

[7] A. Shakouri, “Nanoscale thermal transport and microrefrigerators on a chip,” *Proc. IEEE 94*, vol. 8, pp. 1613–1638, 2006.

[8] R. V. I. Chowdhury, R. Prasher, K. Lofgreen, G. Chrysler, S. Narasimhan, R. Mahajan, D. Koester, R. Alley, “On-chip cooling by superlattice-based thin-film thermoelectrics,” *Nat. Nano.*, vol. 4, no. 4, pp. 235– 238, 2009.

[9] V.A. Semenyuk, “Thermoelectric Cooling of Electro-Optic Components,” in *Thermoelectrics Handbook: Macro to Nano*, 2006.

[10] D. D. Pollock, “Thermoelectric Phenomena,” in *CRC Handbook of Thermoelectrics*, D. M. Rowe, Ed. CRC Press, 1995.

[11] K. Uemura, “Commercial Peltier Modules,” in *CRC Handbook of Thermoelectrics*, D. M. Rowe, Ed. CRC Press, 1995.

[12] W. C. . Hall, “Terrestrial Applications of Thermoelectric Generators,” in *CRC Handbook of Thermoelectrics*, D. M. Rowe, Ed. CRC Press, 1995.

[13] T. Kajikawa, “Thermoelectric Power Generation System Recovering Industrial Waste Heat,” in *Thermoelectrics Handbook: Macro to Nano*, D. M. Rowe, Ed. CRC Press, 2006.

[14] A. F. Ioffe, *Semiconductor Thermoelements and Thermoelectric Cooling*. London: Infosearch Limited, 1957.

[15] G. J. Snyder and E. S. Toberer, “Complex thermoelectric materials,” *Nat. Mater.*, vol. 7, p. 105, Feb. 2008.

[16] L. D. Hicks and M. S. Dresselhaus, “Effect of quantum-well structures on the thermoelectric figure of merit,” *Phys. Rev. B*, vol. 47, no. 19, pp. 12727–12731, May 1993.

[17] J. He, M. G. Kanatzidis, and V. P. Dravid, “High performance bulk thermoelectrics via a panoscopic approach,” *Mater. Today*, vol. 16, no. 5, pp. 166–176, 2013.

[18] G. A. Slack, “New Materials and Performance Limits for Thermoelectric Cooling,” *D. Rowe (Ed.), CRC Handb. Thermoelectr. CRC Press. Boca Raton, FL.*, vol. Ch. 34, 1995.

[19] H. Mizuno, S. Mossa, and J.-L. Barrat, “Beating the amorphous limit in thermal conductivity by superlattices design,” *Sci. Rep.*, vol. 5, p. 14116, Sep. 2015.

[20] G. D. Mahan and J. O. Sofo, “The best thermoelectric.,” *Proc. Natl. Acad. Sci. U. S. A.*, vol. 93, no. 15, pp. 7436–7439, Jul. 1996.

[21] P. Norouzzadeh and D. Vashaee, “Classification of Valleytronics in Thermoelectricity,” *Sci. Rep.*, vol. 6, p. 22724, Mar. 2016.

[22] O. Hiromichi, M. Taku, Z. Shijian, K. Takeharu, I. Yuichi, A. Katsumi, K. Hideya, N. Kenji, and H. Hideo, “Unusually Large Enhancement of Thermopower in an Electric Field Induced Two-Dimensional Electron Gas,” *Adv. Mater.*, vol. 24, no. 6, pp. 740–744, 2012.

[23] J. P. Heremans, V. Jovovic, E. S. Toberer, A. Saramat, K. Kurosaki, A. Charoenphakdee, S. Yamanaka, and G. J. Snyder, “Enhancement of Thermoelectric Efficiency in PbTe by Distortion of the Electronic Density of States,” *Science (80-.).*, vol. 321, no. 5888, pp. 554–557, 2008.

[24] Y. I. Ravich, “Selective Carrier Scattering in Thermoelectric Materials,” in *CRC Handbook of Thermoelectrics*, D. M. Rowe, Ed. CRC Press, 1995.

[25] Y. Pei, A. LaLonde, S. Iwanaga, and G. J. Snyder, “High thermoelectric figure of merit in heavy hole dominated PbTe,” *Energy Environ. Sci.*, vol. 4, no. 6, pp. 2085–2089, 2011.

[26] H. Le Thanh, N. Duc-The, H. Li, I. B. Brummerstedt, Y. Hao, P. Nini, and V. N. Ngo, “In Operando Study of High-Performance Thermoelectric Materials for Power Generation: A Case Study of β-Zn_4Sb_3,” *Adv. Electron. Mater.*, vol. 3, no. 10, p. 1700223, 2017.

[27] K. Biswas, J. He, Q. Zhang, G. Wang, C. Uher, V. P. Dravid, and M. G. Kanatzidis, “Strained endotaxial nanostructures with high thermoelectric figure of merit,” *Nat. Chem.*, vol. 3, p. 160, Jan. 2011.

[28] D. R. Brown, T. Day, K. A. Borup, S. Christensen, B. B. Iversen, and G. J. Snyder, “Phase transition enhanced thermoelectric figure-of-merit in copper chalcogenides,” *APL Mater.*, vol. 1, no. 5, p. 52107, 2013.

[29] G. Rogl, L. Zhang, P. Rogl, A. Grytsiv, M. Falmbigl, D. Rajs, M. Kriegisch, H. Müller, E. Bauer, J. Koppensteiner, W. Schranz, M. Zehetbauer, Z. Henkie, and M. B. Maple, “Thermal expansion of skutterudites,” *J. Appl. Phys.*, vol. 107, no. 4, p. 43507, 2010.

[30] A. Sarhadi, R. Bjørk, and N. Pryds, “Optimization of the Mechanical and Electrical Performance of a Thermoelectric Module,” *J. Electron. Mater.*, vol. 44, no. 11, pp. 4465–4472, 2015.

[31] J. Leszczynski, K. T. Wojciechowski, and A. L. Malecki, “Studies on thermal decomposition and oxidation of CoSb3,” *J. Therm. Anal. Calorim.*, vol. 105, no. 1, p. 211, Mar. 2011.

[32] H. Ran, S. Gabi, and N. Kornelius, “Thermoelectric Devices: A Review of Devices, Architectures, and Contact Optimization,” *Adv. Mater. Technol.*, vol. 3, no. 4, p. 1700256, 2018.

[33] M. Gao, D. M. Rowe, O. Assis, and S. G. K. Williams, “Determining the Electrical and Thermal Contact Resistance of a Thermoelectric Module,” in *Proceedings of 11th International Conference on Thermoelectrics*, 1992, pp. 210–212.

[34] G. Min and M. Phillips, “Preparation and Characterization of TE Interfaces/Junctions,” in *Thermoelectric Energy Conversion: Basic Concepts and Device Applications*, D. D. Pineda and A. Rezania, Eds. 2017, pp. 111–125.

[35] P. Shewmon, *Diffusion in Solids*, Second. Springer, Cham, 2016.

[36] E. European Space Agency, “Phase Diagrams.” [Online]. Available: http://www.spaceflight.esa.int/impress/text/education/Solidification/.

[37] P. F., “Phase diagram of Pb-Sn (lead-tin) system,” in *Phase Equilibria, Crystallographic and Thermodynamic Data of Binary Alloys*, P. F., Ed. 2016.

[38] X. Su, N. Y. Tang, and J. M. Toguri, “Thermodynamic assessment of the Ni-Zn system,” *J. Phase Equilibria*, vol. 23, no. 2, pp. 140–148, 2002.

[39] H. J. Okamoto, “Ni-Zn (Nickel-Zinc),” *J. Phase Equilibria Diffus.*, vol. 34, 2013.

[40] J. E. Gould, “Mechanisms of solid-state bonding processes,” in *Microjoining and Nanojoining*, Y. Zhou, Ed. Woodhead Publishing Limited, 2008, pp. 3–24.

[41] M. Abtew and G. Selvaduray, “Lead-free Solders in Microelectronics,” *Mater. Sci. Eng.*, vol. 27, pp. 95–141, 2000.

[42] S.-J. Kim, K.-S. Kim, S.-S. Kim, C.-Y. Kang, and K. Suganuma, “Characteristics of Zn-Al-Cu Alloys for High Temperature Solder Application,” *Mater. Trans.*, vol. 49, no. 7, pp. 1531–1536, 2008.

[43] MatWeb, “Lucas-Milhaupt AL 802, AL 822, AL 719, Silvaloy 18M, Silvaloy A54N.” [Online]. Available: http://www.matweb.com.

[44] Sil.Fos, “Lucas-Milhaupt Silvaloy 401.” [Online]. Available: http://www.silfos.com/.

[45] D. M. Jacobson and G. Humpston, *Principles of Brazing*. ASM International, 2005.

[46] P. Roberts, *Industrial Brazing Practice*. CRC Press, 2003.

[47] T. Takemoto, “Mechanisms of soldering and brazing,” in *Microjoining and Nanojoining*, Y. Zhou, Ed. 2008, pp. 25–50.

[48] M. Weinstein and A. I. Mlavsky, “Bonding of Lead Telluride to Pure Iron Electrodes,” *Rev. Sci. Instrum.*, vol. 33, pp. 1119–1120, 1962.

[49] M. L. Kuntz and Y. Zhou, “Diffusion soldering and brazing,” in *Microjoining and Nanojoining*, Y. Zhou, Ed. 2008, pp. 269–298.

[50] Y. C. Lin, K. T. Lee, J. D. Hwang, H. S. Chu, C. C. Hsu, S. C. Chen, and T. H. Chuang, “Solid Liquid Interdiffusion Bonding of Zn_4Sb_3 Thermoelectric Material with Cu Electrode,” *J. Electron. Mater.*, vol. 45, no. 10, pp. 4935–4942, 2016.

[51] A. Shirzadi, “Solid-state diffusion bonding,” in *Microjoining and Nanojoining*, Y. Zhou, Ed. 2008, pp. 234–249.

[52] W. Liu, H. Wang, L. Wang, X. Wang, G. Joshi, G. Chen, and Z. Ren, “Understanding of the contact of nanostructured thermoelectric n-type $Bi_2Te_{2.7}Se_{0.3}$ legs for power generation applications,” *J. Mater. Chem. A*, vol. 1, no. 42, pp. 13093–13100, 2013.

[53] D. Kraemer, J. Sui, K. McEnaney, H. Zhao, Q. Jie, Z. F. Ren, and G. Chen, “High thermoelectric conversion efficiency of MgAgSb-based material with hot-pressed contacts,” *Energy Environ. Sci.*, vol. 8, no. 4, pp. 1299–1308, 2015.

[54] W. Schottky, “Halbleitertheorie der Sperrschicht,” *Naturwissenschaften*, vol. 26, p. 843, 1938.

[55] N. F. Mott, “Note on the contact between a metal and an insulator or semi-conductor,” *Math. Proc. Cambridge Philos. Soc.*, vol. 34, pp. 568–572, 1938.

[56] W. Mönch, “On the physics of metal-semiconductor interfaces,” *Reports Prog. Phys.*, vol. 53, pp. 221–278, 1990.

[57] M. J. Deen and F. Pascal, “Electrical characterization of semiconductor materials and devices—review,” *J. Mater. Sci. Mater. Electron.*, vol. 17, no. 8, pp. 549–575, 2006.

[58] S. Oyama, T. Hashizume, and H. Hasegawa, “Mechanism of current leakage through metal/n-GaN interfaces,” *Appl. Surf. Sci.*, vol. 190, no. 1, pp. 322–325, 2002.

[59] W. Mönch, “Metal-semiconductor contacts: electronic properties,” *Surf. Sci.*, vol. 299–300, no. C, pp. 928–944, 1994.

[60] S. Sudharsanan and S. Karmalkar, “Modeling of the reverse gate leakage in AlGaN/GaN high electron mobility transistors,” *J. Appl. Phys.*, vol. 107, no. 6, p. 64501, Mar. 2010.

[61] A. Mimouni, T. Fernández, J. Rodriguez-Tellez, A. Tazon, H. Baudrand, and M. Boussuis, “Gate Leakage Current in GaN HEMT’s: A Degradation Modeling Approach,” *Electr. Electron. Eng.*, vol. 2, no. 6, pp. 397–402, 2012.

[62] S. Ganguly, A. Konar, Z. Hu, H. Xing, and D. Jena, “Polarization effects on gate leakage in InAlN/AlN/GaN high-electron-mobility transistors,” *Appl. Phys. Lett.*, vol. 101, no. 25, p. 253519, 2012.

[63] W. Xu, H. Rao, and G. Bosman, “Evidence of space charge limited flow in the gate current of AlGaN/GaN high electron mobility transistors,” *Appl. Phys. Lett.*, vol. 100, no. 22, p. 223504, May 2012.

[64] “International Energy Agency,” 2018.

[65] L. I. Anatychuk and R. V. Kuz, “Materials for Vehicular Thermoelectric Generators,” *J. Electron. Mater.*, vol. 41, no. 6, pp. 1778–1784, 2012.

[66] O. Guillon, J. Gonzalez-Julian, B. Dargatz, T. Kessel, G. Schierning, J. Räthel, and M. Herrmann, “Field-Assisted Sintering Technology/Spark Plasma Sintering: Mechanisms, Materials, and Technology Developments,” *Adv. Eng. Mater.*, vol. 16, no. 7, pp. 830–849, 2014.

[67] “ULVAC ZEM3 thermoelectric testers.” [Online]. Available: http://www.ulvac.com/components/Thermal-Instruments/Thermoelectric-Testers/ZEM-3-Series.

[68] P. J. Shaver and J. Blair, “Thermal and electronic transport properties of p-type ZnSb,” *Phys. Rev.*, vol. 141, no. 2, pp. 649–663, 1966.

[69] G. J. Snyder, M. Christensen, E. Nishibori, T. Caillat, and B. B. Iversen, “Disordered zinc in Zn_4Sb_3 with phonon-glass and electron-crystal thermoelectric properties,” *Nat. Mater.*, vol. 3, no. 7, pp. 458–463, 2004.

[70] J.-B. Li, M.-C. Record, and J.-C. Tedenac, “A thermodynamic assessment of the Sb–Zn system,” *J. Alloys Compd.*, vol. 438, no. 1, pp. 171–177, 2007.

[71] A. Hruby, J. Berankova, and V. Miskova, “Growth of ZnSb Single Crystal,” *Phys. Stat. Sol.*, vol. 3, p. 289, 1963.

[72] E. K. Arushanov, “Crystal growth, characterization and application of II V compounds,” *Prog. Cryst. Growth Charact.*, vol. 13, no. 1, pp. 1–38, 1986.

[73] H. Komiya, K. Masumoto, and H. Y. Fan, “Optical and Electrical Properties and Energy Band Structure of ZnSb,” *Phys. Rev.*, vol. 133, no. 6A, pp. A1679-A1684, Mar. 1964.

[74] A. B. Blichfeld and B. B. Iversen, “Fast direct synthesis and compaction of phase pure thermoelectric ZnSb,” *J. Mater. Chem. C*, vol. 3, no. 40, pp. 10543–10553, 2015.

[75] Y. Tang, Z. M. Gibbs, L. A. Agapito, G. Li, H.-S. Kim, M. B. Nardelli, S. Curtarolo, and G. J. Snyder, “Convergence of multi-valley bands as the electronic origin of high thermoelectric performance in $CoSb_3$ skutterudites,” *Nat. Mater.*, vol. 14, p. 1223, Oct. 2015.

[76] M. Rull-Bravo, A. Moure, J. F. Fernández, and M. Martín-González, “Skutterudites as thermoelectric materials: revisited,” *RSC Adv.*, vol. 5, no. 52, pp. 41653–41667, 2015.

[77] T. Caillat, A. Borshchevsky, and J. -P. Fleurial, “Properties of single crystalline semiconducting $CoSb_3$,” *J. Appl. Phys.*, vol. 80, no. 8, pp. 4442–4449, 1996.

[78] G. A. Slack, “New Materials and Performance Limits for Thermoelectric Cooling,” *D. Rowe (Ed.), CRC Handb. Thermoelectr. CRC Press. Boca Raton, FL.*, vol. Ch. 34, 1995.

[79] Y. G. Yan, W. Wong-Ng, L. Li, I. Levin, J. A. Kaduk, M. R. Suchomel, X. Sun, G. J. Tan, and X. F. Tang, “Structures and thermoelectric properties of double-filled $(Ca_xCe_{1-x})Fe_4Sb_{12}$ skutterudites,” *J. Solid State Chem.*, vol. 218, pp. 221–229, 2014.

[80] H. Luo, J. W. Krizan, L. Muechler, N. Haldolaarachchige, T. Klimczuk, W. Xie, M. K. Fuccillo, C. Felser, and R. J. Cava, “A large family of filled skutterudites stabilized by electron count,” *Nat. Commun.*, vol. 6, pp. 1–10, 2015.

[81] B. C. Sales, D. Mandrus, and R. K. Williams, “Filled Skutterudite Antimondies: A New Class of Thermoelectric Materials,” *Science (80-.).*, vol. 272, no. V, p. 5266, 1996.

[82] G. Rogl, A. Grytsiv, P. Rogl, N. Peranio, E. Bauer, M. Zehetbauer, and O. Eibl, “N-Type skutterudites $(R,Ba,Yb)_yCo_4Sb_{12}$ (R = Sr, La, Mm, DD, SrMm, SrDD) approaching ZT ≈ 2.0,” *Acta Mater.*, vol. 63, pp. 30–43, 2014.

[83] G. Rogl, A. Grytsiv, P. Rogl, E. Bauer, M. Hochenhofer, R. Anbalagan, R. C. Mallik, and E. Schafler, "Nanostructuring of p- and n-type skutterudites reaching figures of merit of approximately 1.3 and 1.6, respectively," *Acta Mater.*, vol. 76, pp. 434–448, 2014.

[84] K. Mimura, J.-W. Lim, M. Isshiki, Y. Zhu, and Q. Jiang, "Brief review of oxidation kinetics of copper at 350 °C to 1050 °C," *Metall. Mater. Trans. A*, vol. 37, no. 4, pp. 1231–1237, 2006.

[85] J. W. Fergus, "Metallic interconnects for solid oxide fuel cells," *Mater. Sci. Eng. A*, vol. 397, no. 1–2, pp. 271–283, 2005.

[86] A. Bin Kaderi, H. Hartmann, and A. Besmehn, "Observation of Oxide Development from Room Temperature (RT) to 700 ^{O}C Demonstrated by In Situ XPS of Crofer 22 APU Alloy," *Oxid. Met.*, vol. 88, no. 3, pp. 459–468, Oct. 2017.

[87] M. Park, J.-S. Shin, S. Lee, H.-J. Kim, H. An, H. Ji, H. Kim, J.-W. Son, J.-H. Lee, B.-K. Kim, H.-W. Lee, and K. J. Yoon, "Thermal degradation mechanism of ferritic alloy (Crofer 22 APU)," *Corros. Sci.*, vol. 134, pp. 17–22, 2018.

[88] P. Pichanusakorn and P. Bandaru, "Nanostructured thermoelectrics," *Mater. Sci. Eng. R Reports*, vol. 67, no. 2, pp. 19–63, 2010.

[89] J. R. Scotsman, R. J. Pcionek, H. Kong, C. Uher, and M. G. Kanatzidis, "Strong reduction of thermal conductivity in nanostructured PbTe prepared by matrix encapsulation," *Chem. Mater.*, vol. 18, no. 21, pp. 4993–4995, 2006.

[90] E. S. Toberer, L. L. Baranowski, and C. Dames, "Advances in Thermal Conductivity," *Annu. Rev. Mater. Res.*, vol. 42, no. 1, pp. 179–209, 2012.

[91] R. Fourmentin, M.-N. Avettand-Fènoël, G. Reumont, and P. Perrot, "The Fe–Zn–Al–Cr system and its impact on the galvanizing process in chromium-added zinc baths," *J. Mater. Sci.*, vol. 43, pp. 6872–6880, 2008.

Appendix-1

Solder free joining as a highly effective method for making contact between thermoelectric materials and metallic electrodes

Authors: Safdar Abbas Malik, Le Thanh Hung and Ngo Van Nong

Status: published

Materials Today Energy 5 (2017) 305–311

Contents lists available at ScienceDirect

Materials Today Energy

journal homepage: www.journals.elsevier.com/materials-today-energy/

Solder free joining as a highly effective method for making contact between thermoelectric materials and metallic electrodes

Safdar Abbas Malik, Le Thanh Hung, Ngo Van Nong*

Department of Energy Conversion and Storage, Technical University of Denmark, Risø Campus, 4000 Roskilde, Denmark

ARTICLE INFO

Article history:
Received 14 March 2017
Received in revised form
30 June 2017
Accepted 17 July 2017

Keywords:
Low-cost thermoelectrics
Contact resistance
Interface kinetics
Zinc antimonide

ABSTRACT

Quality of joining and interfacial evolution behavior play a critical role in the performance and reliability of thermoelectric (TE) devices. In this study, different joining methods using $Zn-2Al$ solder alloy (1) and solder-free joining with microlayers of Ti and Cr as interconnecting agents (2) were systematically investigated and demonstrated on the low-cost ZnSb TE system. ZnSb material, which was chosen to bond with Ag and Ni metallic electrodes, exhibited a maximum zT value of 0.8 at 400 °C. With the joining method (1), Zn from the $Zn-2Al$ solder was found to diffuse/react with both Ag and Ni electrodes, and penetrate into ZnSb legs. SEM-EDX analysis recorded a significant excess of Zn in the ZnSb leg after joining. We found that, using microlayers of Ti and Cr as interconnecting agent, a very good interfacial contact was obtained, and the starting composition of ZnSb legs was preserved. The interfacial contact of $ZnSb/Cr/Ni$ was found to be stable after heat treatment at 400 °C for 30 h, suggesting solder-free joining as an effective method for reliable contacts in TE devices in the medium temperature region (200 °C – 400 °C).

1. Introduction

Thermoelectric (TE) devices convert heat into electricity and vice versa, without any moving parts. Because of their ability to fit any size and shape, TE devices offer a wide range of applications: from miniaturized cooling of IC chips [1,2] to electricity generation in remote areas [3]. The increasing demand for renewable energy has brought thermoelectricity in the limelight as a potential candidate for green cooling and waste heat recovery. High performance of a TE material requires optimization of a series of interrelated physical properties, namely: the Seebeck coefficient, 'α'; the electrical conductivity, 'σ'; and the thermal conductivity, 'κ'. The material figure of merit, zT, quantifies the performance of a TE material:

$$zT = \frac{\alpha^2 \sigma T}{\kappa}. \tag{1}$$

The device figure of merit, ZT, can be defined in terms of the total Seebeck coefficient, S, total electrical resistance, R, and total thermal conductance, K, of the module [4–6] as:

$$ZT = \frac{S^2 T}{RK} = \frac{S^2 T}{\left(R_{leg} + R_c\right)\left(K_{leg} + K_c\right)}. \tag{2}$$

Here, $R = R_{leg} + R_c$ and $K = K_{leg} + K_c$. R_c and K_c are the electrical and thermal contact resistances, respectively. The maximum efficiency of a device, operating between a hot side temperature T_h and a cold side temperature T_c, is defined as [4]:

$$\eta_{max} = \frac{T_h - T_c}{T_h} \times \frac{\sqrt{ZT+1} - 1}{\sqrt{ZT+1} + \frac{T_c}{T_h}}. \tag{3}$$

It is clear from equations (2) and (3) that the performance of TE device depends not only on the intrinsic material properties, but also on the thermal and electrical contact resistances (R_c and K_c). For practical TE power generation, low resistance and stable interfacial contact play an important role in the performance and long-term stability of TE devices. To achieve high conversion efficiency, the ratio of total contact resistance to total device resistance should be as small as possible, at most within 10%, to minimize the losses [7,8].

The realization of TE generators (TEGs) on an industrial scale is haunted by the conditions of application and complexities involved in TE materials [9]. Since TEGs usually operate at large temperature

* Corresponding author.
E-mail address: ngno@dtu.dk (N. Van Nong).

http://dx.doi.org/10.1016/j.mtener.2017.07.012
2468-6069/

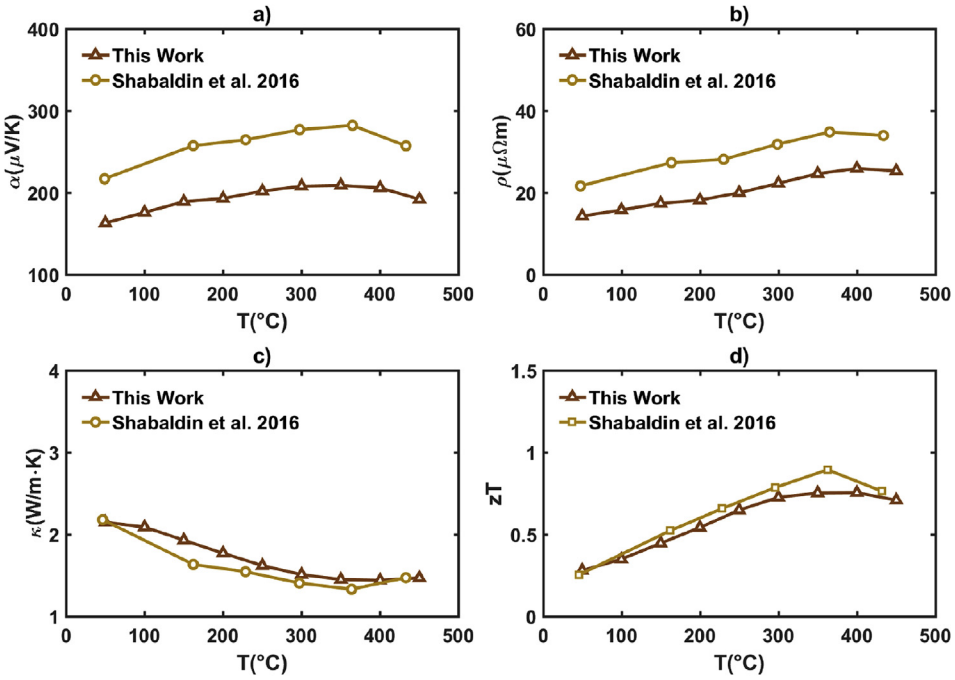

Fig. 1. Temperature dependence of the TE properties of undopped ZnSb in this work as compared with literature (0.1% Sn doped ZnSb) [22]: a) Seebeck coefficient, b) electrical resistivity, c) thermal resistivity, d) figure of merit.

gradients and various thermal cycles, their stability is a matter of great concern. In fact, there are many low cost, non-toxic TE materials such as Cu_2S, Cu_2Se and Zn_4Sb_3 [10,11,13]; that exhibit very good TE properties but there have been concerns about their stability under real operating conditions. As an important example, Zn_4Sb_3 exhibits high zT value of 1.4 at 450 °C due to its very low thermal conductivity resulting from phonon scattering by Zn interstitials [13]. However, it was found that under working conditions, Zn whiskers precipitate at the cold side of the leg and they cause material failure over time [12]. In the family of Zinc Antimonide compounds [14–18], the ZnSb phase has orthorhombic crystal structure and it is expected to be more stable than Zn_4Sb_3 phase since it does not contain mobile Zn on interstitial sites. Ignored for years, ZnSb has an indirect bandgap of 0.5 eV at room temperature and carrier concentration of $\approx 10^{16} cm^{-3}$ [19,20]. Most of the reported work on TE properties of this material involves hole doping because carrier concentration in undoped ZnSb is low compared to state of the art TE materials [21–26]. While it is one of the few Tellurium free TE materials in the medium temperature range [21], there is lack of research on implementation of this material in commercial TE modules.

In this work, both the conventional joining method using lead free $Zn-2Al$ soldering alloy (with chemical formula $Zn_{98}Al_2$) and an innovative direct joining method are investigated to bond the ZnSb material with metallic electrodes such as Silver (Ag) and Nickel (Ni). The TE properties of ZnSb are characterized as a function of temperature from 50 °C up to 450 °C. Ag and Ni electrodes were chosen due to their excellent transport properties, comparable thermal expansion coefficients with ZnSb, corrosion resistance and availability in abundance. $Zn-2Al$ has been selected because of its good wetting properties and high shear strength [27,28]. The solidus and liquidus temperatures of this alloy; 377 °C and 385 °C respectively; are close to the maximum working temperature of ZnSb. The interfacial behavior evolution and chemical composition of the TE material after joining by both the methods are systematically investigated and compared.

2. Experimental details

ZnSb ingots used for this study were provided by TEGnology AS, Denmark. Details of the material synthesis are discussed elsewhere [29]. The electrical resistivity and Seebeck coefficient were measured on an ULVAC-RIKO ZEM-3 from 50 °C up to 450 °C in 0.1 bar Helium atmosphere. The thermal conductivity was calculated from the thermal diffusivity and heat capacity obtained by the laser flash method on NETZSCH LFA 457 MicroFlash®, and mass density using the Archimedes principle. The ZnSb legs, $Zn-2Al$ solder and the Ag, Ni electrodes were cut to their respective dimensions with cross-sectional area of $3 \times 3\ mm^2$. Their surfaces were polished using the SiC sandpaper to remove oxidation layers and to reduce interfacial inhomogeneities, degreased in acetone and finally cleaned by ethanol. Microlayers of Ti and Cr were deposited on the surface of ZnSb using Radio Frequency (RF) sputtering. All parts were assembled together inside a graphite die. The joining was performed in Argon atmosphere. The joining temperature was maintained for 30 min at 400 °C and 450 °C for the Zn-2Al soldering method and the solder-free joining method, respectively. A constant pressure of 3 MPa was applied on the samples during the joining process. The resulting samples were then polished and observed using Hitachi TM3000 electron microscope. The interfaces were scanned in the EDX mode to study the interfacial reactions and interdiffusion.

3. Results and discussion

3.1. Thermoelectric properties

Fig. 1 shows the TE properties of the undopped ZnSb material used in this work as a function of temperature from 50 °C to 450 °C. The recently reported properties of 0.1% Sn-doped ZnSb [22] have also been plotted for comparison. It is seen that the Seebeck coefficient has a positive value in the entire measured temperature range, indicating a p-type conduction, as shown in Fig. 1 (a). In the

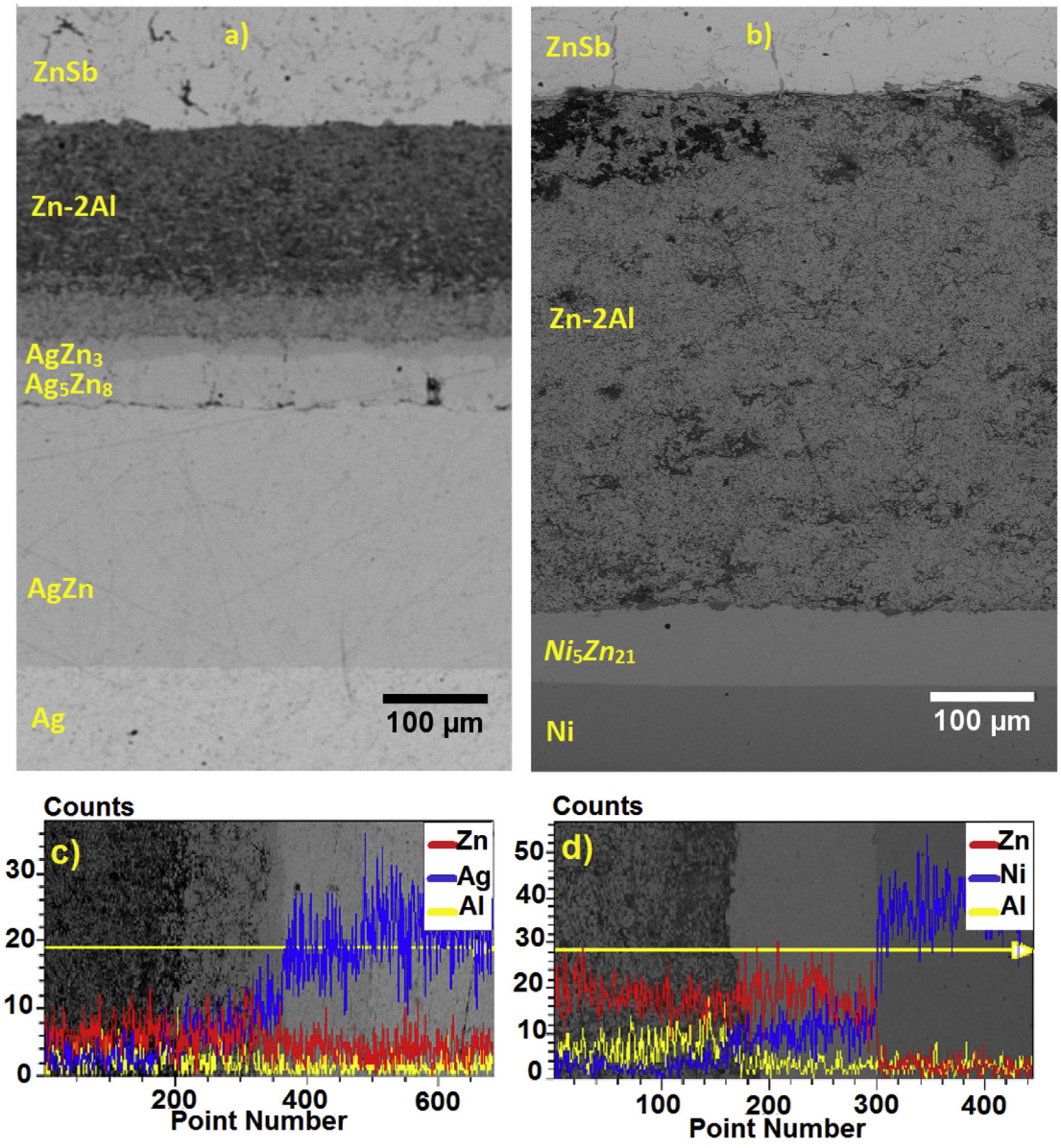

Fig. 2. SEM micrograph of: a) *ZnSb*/*Zn* – 2*Al*/*Ag* and b) *ZnSb*/*Zn* – 2*Al*/*Ni* samples. The EDX linescan of: c) *Zn* – 2*Al*/*Ag* interface and d) *Zn* – 2*Al*/*Ni* interface.

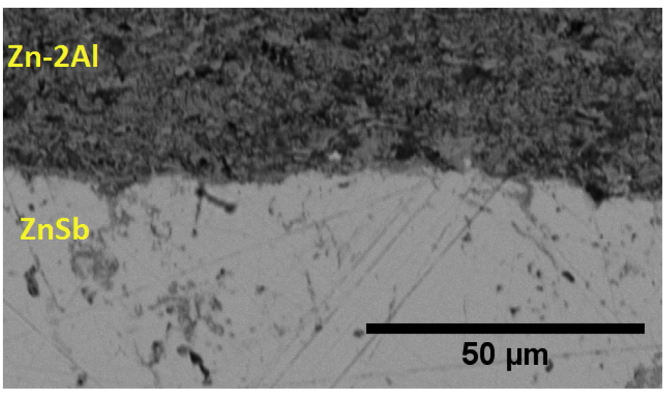

Fig. 3. SEM micrographs of *Zn* – 2*Al*/*ZnSb* interface after joining.

temperature region below 400 °C, the electrical resistivity tends to increase with increasing temperature, showing a metallic behavior (see Fig. 1 (b)). Both the electrical resistivity and Seebeck coefficient start to drop as temperature increases above 400 °C. A similar trend has been observed in other reports on ZnSb due to variation in the carrier concentration with increasing temperature [23–26].

The thermal conductivity decreased from 2.2 W/m·K at 50 °C to 1.5 W/m·K at 400 °C (see Fig. 1 (c)). Overall, the thermal conductivity values of ZnSb phase are relatively higher than those for the Zn_4Sb_3 phase [17]. Our results are in good agreement with the previously reported study [22]. However, the Seebeck coefficient and the electrical resistivity of the material produced by Shabaldin et al. are a bit higher than our samples. This could be attributed to the higher concentration of holes in their samples due to Sn doping. Another reason might be the different synthesis routes. Shabaldin et al. prepared their samples using hot press method on the ZnSb powder, whereas our samples were prepared by an SPS

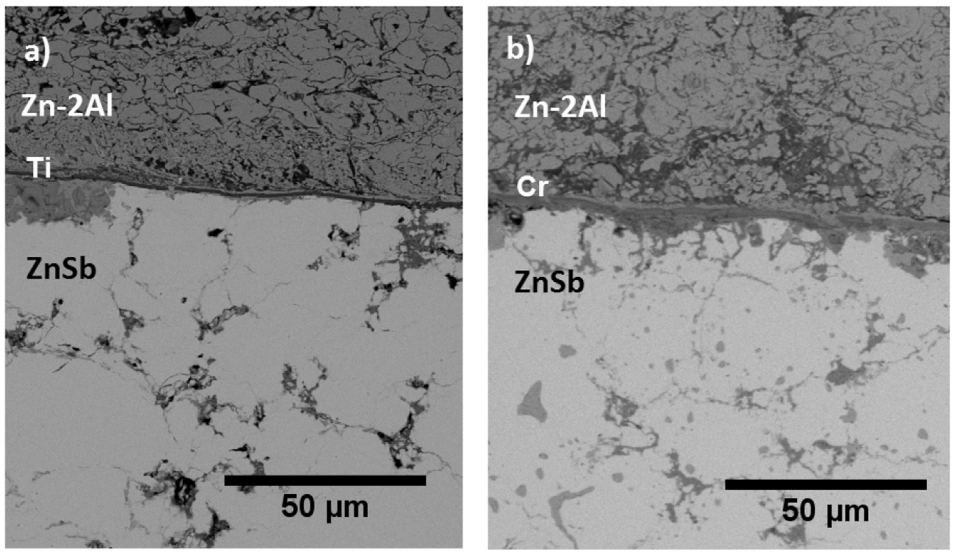

Fig. 4. Interface of *ZnSb* and $Zn-2Al$ solder alloy: a) SEM micrograph of $Zn-2Al/Ti/ZnSb$ interface, b) SEM micrograph of $Zn-2Al/Cr/ZnSb$ interface.

based fast reaction of elemental powders. These differences may end up in different forms of phase inhomogeneities and defects inherent to this complex intermetallic [15,31]. Both the electrical and thermal transport properties of ZnSb are affected by synthesis conditions and hence the concentration and distribution of Zn defects [32,33]. The maximum zT value of 0.8 for our sample was obtained around 400 °C, comparable with other TE materials such as Mn-Si, Clathrates, etc. operating in the same temperature range [7,34].

3.2. Conventional joining with solder

Fig. 2 shows the SEM micrographs of the interface between Ag, Ni electrodes, $Zn-2Al$ solder and ZnSb material. It can be seen that the interfacial contact of the $ZnSb/Zn-2Al$, $Ag/Zn-2Al$ and $Ni/Zn-2Al$ is solid formed without cracks or airgaps. However, a large diffusion/reaction region between solder and electrodes can be observed, and the effect is more profound for Ag than it is for Ni. Further analysis by EDX revealed that Zn from the solder diffused into the electrodes and reacted with Ag and Ni. The high magnitude of Zn diffusion into the Ag and Ni electrodes is evident from the image contrast and EDX linescan.

As we can see from Fig. 2 (a) and (c), reaction layers form on both sides of the $Ag/Zn-2Al$ interface. Not only Zn diffused into Ag, but Ag also diffused deeply into the solder. According to the phase diagram of the $Ag-Zn$ system [35], there exist four intermetallic phases, namely the β, ζ, γ and ε phases with chemical compositions of *AgZn* (high temperature), *AgZn* (low temperature), Ag_5Zn_8 and $AgZn_3$, respectively with distinct properties [36,37]. From the EDX analysis, we find that two consecutive intermetallic layers of compositions Ag_5Zn_8 and $AgZn_3$ are formed on the $Zn-2Al$ side of the interface while a thicker *AgZn* intermetallic layer is formed on the Ag side of the interface. The *AgZn* phase grows fast (with thickness of $\approx 250\mu m$ into the electrode), while the Ag_5Zn_8 grows at an intermediate rate ($\approx 50\mu m$ into the solder) and the $AgZn_3$ develops slowly as compared to the other two (with $\approx 20\mu m$ thickness).

Contrary to the case of Silver, Nickel did not diffuse deeply into the solder as seen from the SEM micrograph and EDX linescan in Fig. 2 (b) and (d). The thermodynamics of the $Ni-Zn$ system [38] suggests low Ni solubility in Zn. Zn diffused and penetrated into Ni and formed a $\approx 70\mu m$ thick intermetallic layer of the γ phase [39] with chemical composition of Ni_5Zn_{21}, based on EDX analysis. The diffusion of Zn into these metallic electrodes is counterproductive because it might deteriorate their excellent properties with time.

Fig. 3 shows the SEM image of the interface between the *ZnSb* leg and the $Zn-2Al$ solder alloy. Overall, the interface looks good i.e. no cracks or airgaps can be observed. In order to investigate the influence on the ZnSb leg after joining, a detailed EDX analysis was carried out by many point measurements along the leg. It was found that the Zn concentration ($\approx$ 56%) is significantly higher than that of Sb($\approx$ 44%) in all randomly selected regions (see figure (1) in Ref. [30]). These observations indicate that a large amount of Zn from $Zn-2Al$ solder has diffused into the ZnSb leg. As a result, after joining, the composition of the leg seems to approach Zn_4Sb_3 phase. While the solder adhered quite well to both electrodes and ZnSb legs, Zn diffused and penetrated into the legs.

To preserve the ZnSb phase of our samples and to minimize the diffusion and reaction at interfaces, we used Ti and Cr layers with a thickness of few microns as diffusion barrier. Shown in Fig. 4 (a, b) are the SEM images of the interfaces between $Zn-2Al$ solder and ZnSb material with Ti and Cr barrier layer. EDX analysis along the ZnSb leg after joining revealed that the barrier layers could not stop Zn from diffusing and penetrating into ZnSb. The average concentrations (in percentage) of Zn:Sb obtained by EDX point measurements are 60:40, approximately. An innovative joining method is needed to overcome this critical problem.

3.3. Solder-free joining through alloying

Since it is hard to stop Zn from diffusing and reacting with both the electrode and ZnSb material, we have tried a direct joining method i.e. without using the Zn-based solder. Looking at the data about the thermodynamics of alloys involving Zn, Sb, Ni, Ag, Ti and Cr [39–43], we conjectured that Ti and Cr could form alloying layers at the interface with electrodes and the TE material, which could serve as interconnects. First, we considered the direct joining with Ag electrode. It turned out to be counterproductive with silver diffusing fast into the ZnSb leg with concentration up to 40%, and hence destroying its thermoelectric

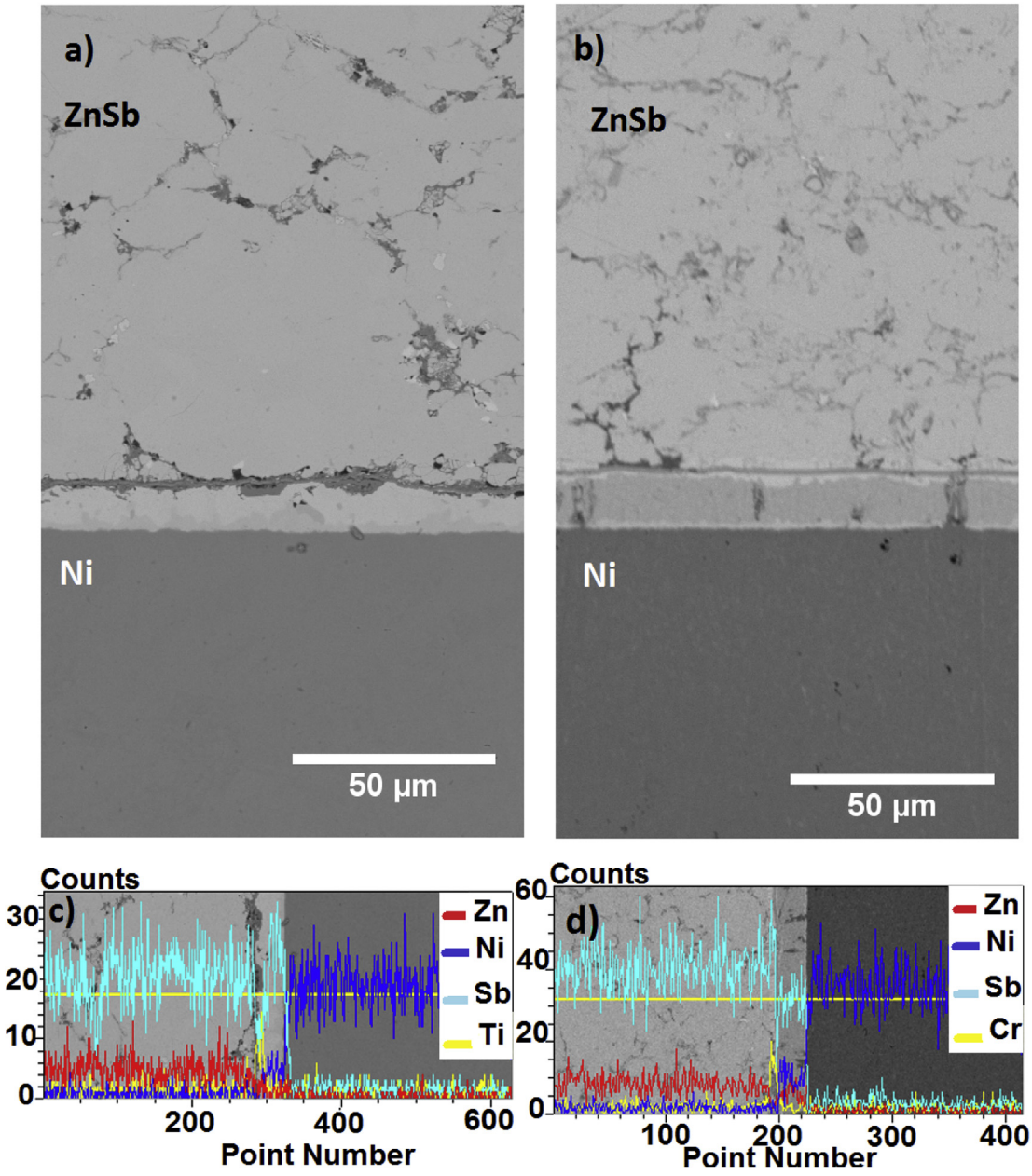

Fig. 5. SEM micrograph of the interface of Ni directly bonded to: a) *Ti/ZnSb* and b) *Cr/ZnSb*. EDX linescan of the interface of Ni bonded to: c) *Ti/ZnSb* and d) *Cr/ZnSb*.

distinction. Therefore, we ruled out Ag and decided to focus on Ni electrode.

Fig. 5 shows the SEM micrographs and EDX profiles of Ni bonded to ZnSb legs via alloying with Ti and Cr layers. A diffusion/reaction region was clearly observed at the interfaces in both the cases of Ti and Cr. Further analysis revealed that Ni, interconnecting layers (Ti, Cr), and ZnSb formed an alloying layer with the thickness in the range of 15–20 µm. EDX linescan indicated strong signal of Sb, Zn, and Ni in the reaction region, while the layers of Ti and Cr could still be detected clearly at the interfaces. Since these alloys involved more than three elements, the phase diagrams describing the kinetics of formation of these alloys and their energetically favorable compositions could not be found in literature. EDX analysis along the ZnSb leg showed that the starting phase of the material was preserved after joining (see Fig. 2 in Ref. [30]).

To check the long-term stability of directly joined contacts in working conditions, the prepared samples were kept at 400 °C under a constant pressure of 3 MPa for 30 h. Fig. 6 presents the SEM micrographs of the joints and EDX linescans through the interfaces. The bonding alloy layer did not proceed further for ZnSb/Cr/Ni contact (Fig. 6(b, d)), while the ZnSb/Ti/Ni contact underwent some degradation with airgaps at the interface (Fig. 6(a, c)). In the ZnSb-side of the ZnSb/Ti/Ni interface, a phase segregation between Zn-rich and Sb-rich regions has occurred which might have caused these airgaps. EDX analysis also pointed out that, in both cases, the composition of the ZnSb leg was preserved. This is a

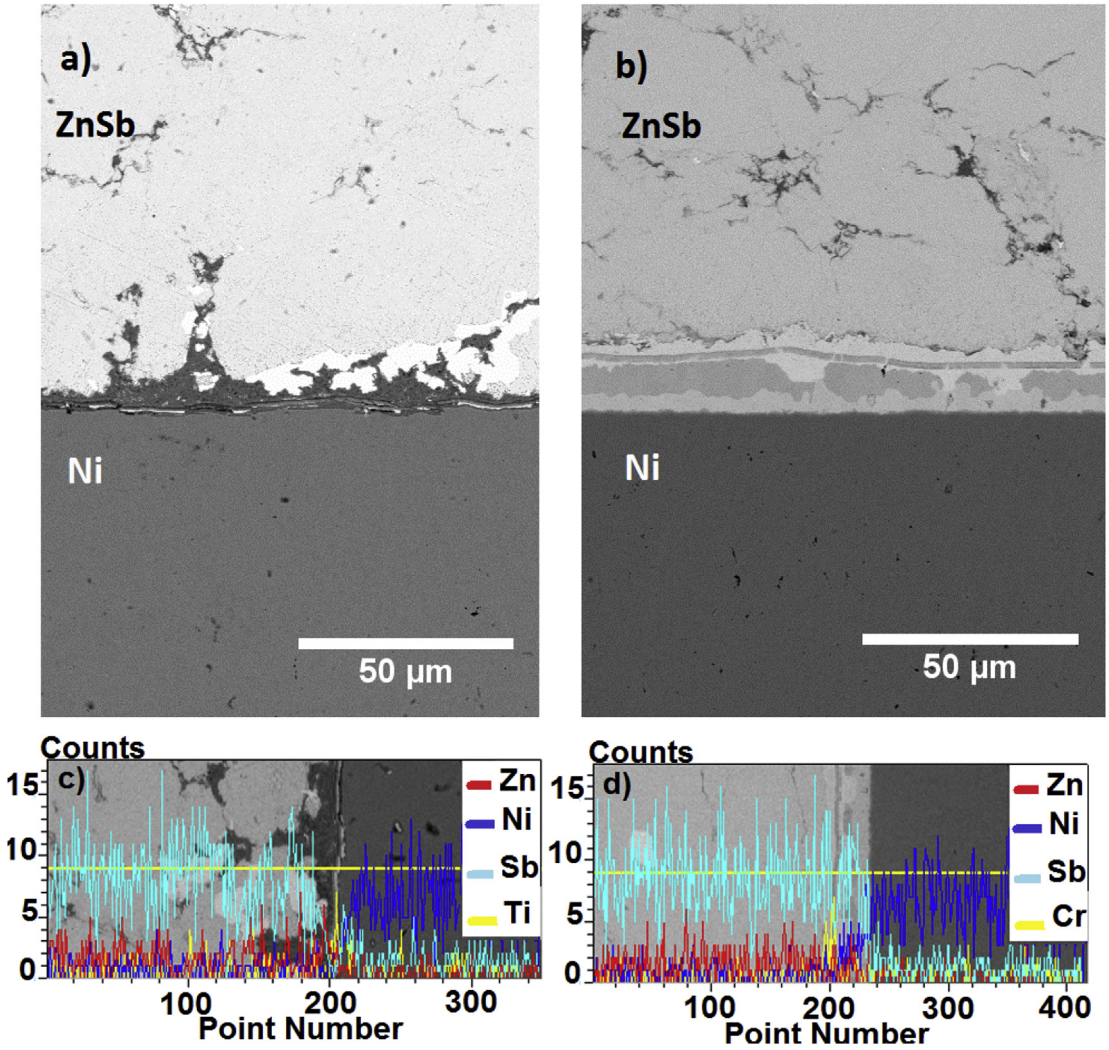

Fig. 6. SEM micrograph of the interface of Ni directly bonded to: a) *Ti/ZnSb* and b) *Cr/ZnSb*, kept at 400 °C for 30 h. EDX linescan of the interface of Ni bonded to: c) *Ti/ZnSb* and d) *Cr/ZnSb*, kept at 400 °C for 30 h.

very promising finding since this method can both make a strong bonding and maintain the composition of the ZnSb phase (see Fig. 3 in Ref. [30]).

4. Conclusion

We have shown that pure ZnSb 1:1 phase is a promising TE material for further development and implementation in TE modules. ZnSb has exhibited good TE properties in medium temperature range with a maximum zT value of 0.8 at 400 °C. Different joining methods were investigated to bond ZnSb-leg with metallic electrodes such as Ag and Ni. In the first method using $Zn-2Al$ soldering alloy, the bonding between ZnSb-leg and Ag, Ni electrodes was good i.e. no cracks or airgaps could be observed. However, Zn from solder strongly diffused and reacted with Ag and Ni, and also penetrated into ZnSb-leg resulting in a significant amount of Zn excess. The diffusion of Zn from solder into TE leg could not be blocked by a diffusion barrier layer of Ti or Cr. A solder-free joining method was discovered and successfully applied to bond Ni electrode with ZnSb using Ti and Cr as interconnects. The results have shown a very good bonding thanks to a thin alloying region formed due to the reaction of Ti and Cr microlayers with Ni and ZnSb. Initial long-term stability test at 400 °C for 30 h revealed that the Cr alloying region was stable and did not develop further, while for the case of Ti, the interface deteriorated over time. Most importantly, the composition of ZnSb leg was maintained after joining. Further research on power generating characteristics including interfacial contact resistance as well as the integration of this material in actual TEG is ongoing.

Acknowledgments

We gratefully acknowledge the financial support by the Danish Council for Strategic Research under the CTEC project No. 1305-00002B. We would also like to thank TEGnology AS for providing us ZnSb ingots.

References

[1] A. Shakouri, Nanoscale thermal transport and microrefrigerators on a chip, Proc. IEEE 94 (8) (2006) 1613–1638, http://dx.doi.org/10.1109/JPROC.2006.879787.
[2] I. Chowdhury, R. Prasher, K. Lofgreen, G. Chrysler, S. Narasimhan, R. Mahajan, D. Koester, R. Alley, R. Venkatasubramanian, On-chip cooling by superlattice-based thin-film thermoelectrics, Nat. Nano 4 (4) (2009) 235–238, http://dx.doi.org/10.1038/nnano.2008.417.

[3] W.C. Hall, Terrestrial applications of thermoelectric generators, in: D. Rowe (Ed.), CRC Handbook of Thermoelectrics, CRC Press, Boca Raton, FL, 1995, http://dx.doi.org/10.1201/9781420049718.ch40. Ch. 40.

[4] H.J. Goldsmid, Conversion efficiency and figure of merit, in: D. Rowe (Ed.), CRC Handbook of Thermoelectrics, CRC Press, Boca Raton, FL, 1995, http://dx.doi.org/10.1201/9781420049718.ch3. Ch. 3.

[5] R.R. Heikes, R.W. Ure, Theoretical Calculation of Device Performance, in: R.R. Heikes, R.W. Ure (Eds.), Thermoelectricity: Science and Engineering, Interscience, New York, 1961, pp. 458–517. Ch. 15.

[6] M. Cobble, Calculation of generator performance, in: D. Rowe (Ed.), CRC Handbook of Thermoelectrics, CRC Press, Boca Raton, FL, 1995, http://dx.doi.org/10.1201/9781420049718.ch39. Ch. 39.

[7] L.T. Hung, N. Van Nong, S. Linderoth, N. Pryds, Segmentation of low-cost high efficiency oxide-based thermoelectric materials, Phys. status solidi (a) 212 (4) (2015) 767–774, http://dx.doi.org/10.1002/pssa.201431626.

[8] G. Min, D.M. Rowe, Handbook of Thermoelectrics, CRC, 1995, http://dx.doi.org/10.1201/9781420049718.ch38. Ch. Peltier Devices as Generators.

[9] L.I. Anatychuk, R.V. Kuz, Materials for vehicular thermoelectric generators, J. Electron. Mater. 41 (6) (2012) 1778–1784, http://dx.doi.org/10.1007/s11664-012-1982-0.

[10] G. Dennler, R. Chmielowski, S. Jacob, F. Capet, P. Roussel, S. Zastrow, K. Nielsch, I. Opahle, G.K.H. Madsen, Are binary Copper Sulfides/Selenides really new and promising thermoelectric materials? Adv. Energy Mater. 4 (9) (2014) http://dx.doi.org/10.1002/aenm.201301581, 1301581–n/a, 1301581.

[11] D.R. Brown, T. Day, T. Caillat, G.J. Snyder, Chemical stability of $(Ag,Cu)_2Se$: a historical overview, J. Electron. Mater. 42 (7) (2013) 2014–2019, http://dx.doi.org/10.1007/s11664-013-2506-2.

[12] L. T. Hung, D.-T. Ngo, L. Han, B. B. Iversen, H. Yin, N. Pryds, N. V. Nong, In operando study of high performance thermoelectric materials for power generation: a case study of Îš-Zn_4Sb_3, Adv. Electron. Mater., (Submitted).

[13] G.J. Snyder, M. Christensen, E. Nishibori, T. Caillat, B.B. Iversen, Disordered zinc in Zn_4Sb_3 with phonon-glass and electron-crystal thermoelectric properties, Nat. Mater 3 (7) (2004) 458–463, http://dx.doi.org/10.1038/nmat1154.

[14] J.-B. Li, M.-C. Record, J.-C. Tedenac, A thermodynamic assessment of the Sb-Zn system, J. Alloys Compd. 39 (06) (2007) 171–177, http://dx.doi.org/10.1016/j.jallcom.2006.08.035.

[15] G.S. Pomrehn, E.S. Toberer, G.J. Snyder, A. van de Walle, Predicted electronic and thermodynamic properties of a newly discovered Zn_8Sb_7 phase, J. Am. Chem. Soc. 133 (29) (2011) 11255–11261, http://dx.doi.org/10.1021/ja202458n.

[16] I. Lapkina, O. Sorokina, V. Ufimtsev, Phase equilibria in system InBi-InSb-Zn_3Sb_2, Zhurnal Neorganicheskoj Khimii 31 (1) (1986) 206–209.

[17] G. Zhu, W. Liu, Y. Lan, G. Joshi, H. Wang, G. Chen, Z. Ren, The effect of secondary phase on thermoelectric properties of Zn_4Sb_3 compound, Nano Energy 2 (6) (2013) 1172–1178, http://dx.doi.org/10.1016/j.nanoen.2013.04.010.

[18] A. He, V. Svitlyk, D. Chernyshov, Y. Mozharivskyj, Identification, structural characterization and transformations of the high-temperature $Zn_{9-\delta}$ Sb phase in the Zn-Sb system, Dalton Trans. 44 (2015) 20983–20990, http://dx.doi.org/10.1039/C5DT03509K.

[19] H. Komiya, K. Masumoto, H.Y. Fan, Optical and electrical properties and energy band structure of ZnSb, Phys. Rev. 133 (1964) A1679–A1684, http://dx.doi.org/10.1103/PhysRev.133.A1679.

[20] E. Arushanov, Crystal growth, characterization and application of II-V compounds, Prog. Cryst. Growth Charact. 13 (1) (1986) 1–38, http://dx.doi.org/10.1016/0146-3535(86)90024-9.

[21] G.J. Snyder, E.S. Toberer, Complex thermoelectric materials, Nat. Mater. 7 (2008) 105–114, http://dx.doi.org/10.1038/nmat2090.

[22] A.A. Shabaldin, L.V. Prokof'eva, G.J. Snyder, P.P. Konstantinov, G.N. Isachenko, A.V. Asach, The influence of weak Tin doping on the thermoelectric properties of Zinc Antimonide, J. Electron. Mater. 45 (3) (2016) 1871–1874, http://dx.doi.org/10.1007/s11664-015-4266-7.

[23] R.C. Miller, Survey of known thermoelectric materials, in: R.R. Heikes, R.W. Ure (Eds.), Thermoelectricity: Science and Engineering, Interscience, New York, 1961, pp. 405–407. Ch. 13.

[24] M. Fedorov, L. Prokof'eva, D. Pshenay-Severin, A. Shabaldin, P. Konstantinov, New interest in intermetallic compound ZnSb, J. Electron. Mater. 43 (6) (2014) 2314–2319, http://dx.doi.org/10.1007/s11664-014-3053-1.

[25] M.I. Fedorov, L.V. Prokofieva, Y.I. Ravich, P.P. Konstantinov, D.A. Pshenay-Severin, A.A. Shabaldin, Thermoelectric efficiency of intermetallic compound ZnSb, Semiconductors 48 (4) (2014) 432–437, http://dx.doi.org/10.1134/S1063782614040095.

[26] L.V. Prokofieva, P.P. Konstantinov, A.A. Shabaldin, D.A. Pshenai-Severin, A.T. Burkov, M.I. Fedorov, Doping and defect formation in thermoelectric ZnSb doped with copper, Semiconductors 48 (12) (2014) 1571–1580, http://dx.doi.org/10.1134/S1063782614120161.

[27] J. Yang, S. Xue, P. Xue, Z. Lv, W. Dai, J. Zhang, Development of novel CsF-RbF-AlF flux for brazing aluminum to stainless steel with Zn-Al filler metal, Mater. Des. 64 (2014) 110–115, http://dx.doi.org/10.1016/j.matdes.2014.07.059.

[28] Y. Takaku, K. Makino, K. Watanabe, I. Ohnuma, R. Kainuma, Y. Yamada, Y. Yagi, I. Nakagawa, T. Atsumi, K. Ishida, Interfacial reaction between Zn-Al-based high-temperature solders and Ni substrate, J. Electron. Mater. 38 (1) (2009) 54–60, http://dx.doi.org/10.1007/s11664-008-0528-y.

[29] A.B. Blichfeld, B.B. Iversen, Fast direct synthesis and compaction of phase pure thermoelectric ZnSb, J. Mater. Chem. C 3 (2015) 10543–10553, http://dx.doi.org/10.1039/C5TC01611H.

[30] S.A. Malik, L.T. Hung, N.V. Nong, SEM/EDX Analysis of Solder Free Joining of the Thermoelectric ZnSb to Metallic Electrodes, 2017. Data in Brief Submitted.

[31] A.S. Mikhaylushkin, J. Nylén, U. Häussermann, Structure and bonding of Zinc Antimonides: complex frameworks and narrow band gaps, Chem. A Eur. J. 11 (17) (2005) 4912–4920, http://dx.doi.org/10.1002/chem.200500020.

[32] K. Hetteer, E. Justi, G. Schneider, Die elektrischen transportgr ossen von ZnSb bei h oheren temperat oren, Adv. Energy Convers. 5 (4) (1965) 355–363, http://dx.doi.org/10.1016/0365-1789(65)90023-8.

[33] R. Pothin, R. Ayral, A. Berche, D. Granier, F. Rouessac, P. Jund, Preparation and properties of ZnSb thermoelectric material through mechanical-alloying and spark plasma sintering, Chem. Eng. J. 299 (2016) 126–134, http://dx.doi.org/10.1016/j.cej.2016.04.063.

[34] S. LeBlanc, S.K. Yee, M.L. Scullin, C. Dames, K.E. Goodson, Material and manufacturing cost considerations for thermoelectrics, Renew. Sustain. Energy Rev. 32 (2014) 313–327, http://dx.doi.org/10.1016/j.rser.2013.12.030.

[35] T. Gómez-Acebo, Thermodynamic assessment of the Ag-Zn system, Calphad 22 (2) (1998) 203–220, http://dx.doi.org/10.1016/S0364-5916(98)00024-8.

[36] B. Magyari-Köpe, G. Grimvall, L. Vitos, Elastic anomalies in Ag-Zn alloys, Phys. Rev. B 66 (2002) 064210, http://dx.doi.org/10.1103/PhysRevB.66.064210.

[37] P. Vaessen, B. Lengeler, W. Schilling, Recovery of the electrical resistivity in electron-irradiated, concentrated Silver-Zinc alloys, Radiat. Eff. 81 (3–4) (1984) 277–292, http://dx.doi.org/10.1080/00337578408206075.

[38] X. Su, N.-Y. Tang, J.M. Toguri, Thermodynamic assessment of the Ni-Zn system, J. Phase Equilibria 23 (2) (2002) 140, http://dx.doi.org/10.1361/1054971023604125.

[39] G.P. Vassilev, T. Gómez-Acebo, J.-C. Tedenac, Thermodynamic optimization of the Ni-Zn system, J. Phase Equilibria 21 (3) (2000) 287–301, http://dx.doi.org/10.1361/105497100770340075.

[40] M. Premović, D. Minić, D. Manasijević, D. Živković, J. Djokić, Experimental investigation and thermodynamic calculations of the Ag-Sb-Zn phase diagram, J. Alloys Compd. 548 (2013) 249–256, http://dx.doi.org/10.1016/j.jallcom.2012.09.030.

[41] K. Wu, Y. Chang, Y. Wang, Simulating interdiffusion microstructures in Ni-Al-Cr diffusion couples: a phase field approach coupled with CALPHAD database, Scr. Mater. 50 (8) (2004) 1145–1150, http://dx.doi.org/10.1016/j.scriptamat.2004.01.025.

[42] P. Turchi, L. Kaufman, Z.-K. Liu, Modeling of Ni-Cr-Mo based alloys: Part I phase stability, Calphad 30 (1) (2006) 70–87, http://dx.doi.org/10.1016/j.calphad.2005.10.003.

[43] R. Schwarz, R. Petrich, C. Saw, The synthesis of amorphous Ni-Ti alloy powders by mechanical alloying, J. Non Crystalline Solids 76 (2–3) (1985) 281–302, http://dx.doi.org/10.1016/0022-3093(85)90005-5.

Appendix-2

Microstructure and chemical data of the thermoelectric ZnSb material after joining to metallic electrodes and heat treatment

Authors: Safdar Abbas Malik, Le Thanh Hung and Ngo Van Nong

Status: published

Data in Brief 15 (2017) 97–101

Contents lists available at ScienceDirect

Data in Brief

journal homepage: www.elsevier.com/locate/dib

Data Article

Microstructure and chemical data of the thermoelectric ZnSb material after joining to metallic electrodes and heat treatment

Safdar Abbas Malik, Le Thanh Hung, Ngo Van Nong *

Department of Energy Conversion and Storage, Technical University of Denmark, Risø Campus, 4000 Roskilde, Denmark

ARTICLE INFO

Article history:
Received 19 July 2017
Received in revised form
5 September 2017
Accepted 12 September 2017
Available online 15 September 2017

ABSTRACT

The data presented in this article are related to the research article entitled: "Solder free joining as a highly effective method for making contact between thermoelectric materials and metallic electrodes" (Malik et al., 2017) [1]. This article presents microstructure obtained by scanning electron microscopy (SEM) and chemical analysis by energy dispersive X-ray spectroscopy (EDX) point measurements of the thermoelectric ZnSb legs after joining to metallic electrodes using solder (Zn-2Al) and free-soldering methods.

Specifications Table

Subject area	*Material Science*
More specific subject area	*Thermoelectric Energy Conversion*
Type of data	*Table, Image (microscopy)*
How data was acquired	*SEM/EDX analysis*

DOI of original article: http://dx.doi.org/10.1016/j.mtener.2017.07.012
* Corresponding author.
E-mail address: ngno@dtu.dk (N.V. Nong).

http://dx.doi.org/10.1016/j.dib.2017.09.023

Data format	*Raw, Analyzed*
Experimental factors	*The ZnSb legs prepared by Spark Plasma Sintering technique from reaction of elemental commercial powders. The surfaces of the leg were polished and cleaned before joining.*
Experimental features	*The quality of material after joining with metallic electrodes was examined.*
Data source location	*Technical University of Denmark, Risø Campus, 4000 Roskilde, Denmark.*
Data accessibility	*The data presented in this article are accessible within this article.*

Value of the data

- This data elaborates the importance of solder free joining method for making good contacts in thermoelectric devices.
- The data presented in this article shows detailed microstructure and EDX analysis of ZnSb material after joining and heat treatment.
- This data allows other researchers to compare the conventional joining method with new solder-free joining method.

1. Data

The following data provides information on the SEM images and EDX analysis along the thermoelectric ZnSb legs. The Figs. 1–3 show micrographs of the ZnSb legs after joining and heat treatment. Tables 1–3 present the concentration ratio of Zn:Sb at selected regions along the leg.

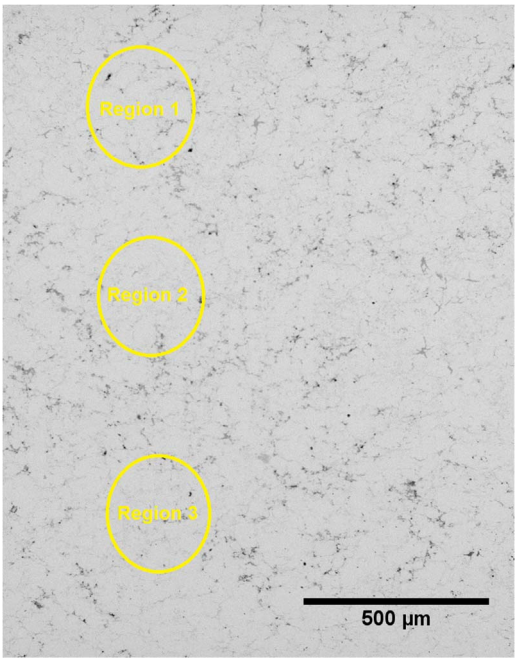

Fig. 1. SEM micrograph and selected EDX point measurements of the ZnSb leg after joining to metallic electrodes using Zn – 2Al solder.

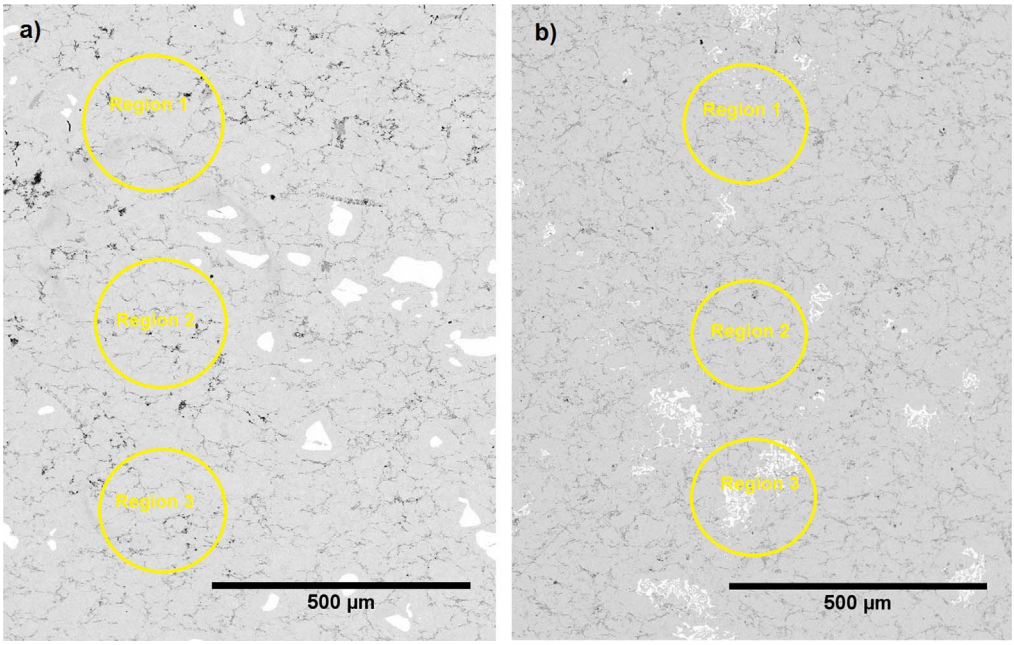

Fig. 2. SEM micrograph and selected EDX point measurements along the ZnSb leg after solder-free joining to Ni electrode with (a) Ti and (b) Cr as interconnecting agents.

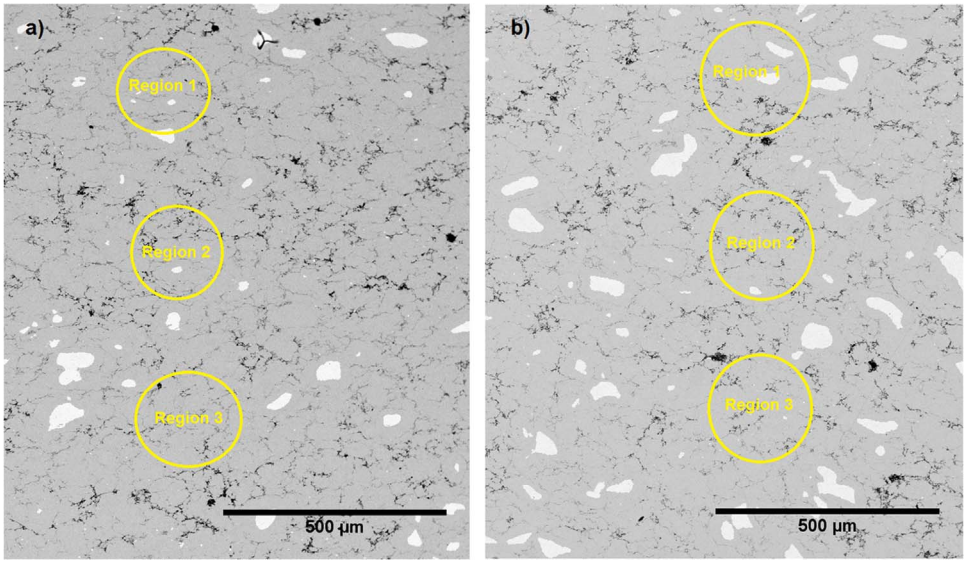

Fig. 3. SEM micrograph of the ZnSb leg after solder-free joining and heat treatment for 30 hours at 400 °C with (a) Ti and (b) Cr as interconnecting agents.

Table 1
Typical EDX point measurements along the ZnSb leg shown in Fig. 1.

% Ratio	Region 1	Region 2	Region 3	Average
Zn:Sb	56.5:43.0	55.3:44.7	56.2:43.4	56:44

Table 2
Typical EDX point measurement along the ZnSb legs shown in Fig. 2.

% Ratio	Region 1	Region 2	Region 3	Average
(a) Zn:Sb	48.9:51.1	47.9:52.1	48.9:51.1	48.5:51.5
(b) Zn:Sb	49.8:50.2	50.5:49.5	52.3:47.7	50.8:49.2

Table 3
Typical EDX point measurement along the ZnSb legs shown in Fig. 3.

% Ratio	Region 1	Region 2	Region 3	Average
(a) Zn:Sb	50.9:49.4	50.8:49.2	51.4:48.6	~51:49
(b) Zn:Sb	50.1:49.9	51.9:48.1	51.5:48.5	~51:49

1.1. After conventional joining with solder

Fig. 1 presents a typical SEM micrograph of the ZnSb leg after conventional joining using Zn – 2Al solder alloy. The chemical analysis of selected EDX point measurements along the leg is presented in Table 1. The average ratio of Zn:Sb is 56:44.

1.2. After solder-free joining

Fig. 2 presents SEM micrographs of the ZnSb legs after solder-free joining with (a) Ti and (b) Cr as interconnecting agents. The EDX point measurements on selected regions are presented in Table 2. The average Zn:Sb ratios are 48.5:51.5 for (a) and 50.8:49.2 for (b).

Fig. 3 shows SEM micrograph of the ZnSb leg after solder-free joining and heat treatment for 30 hours at 400 °C with (a) Ti and (b) Cr as interconnecting agents. The typical EDX point measurements are given in Table 3.

2. Experimental design, materials and methods

ZnSb ingots used for this study were provided by TEGnology AS, Denmark. ZnSb legs with dimension of 3×3×3 mm^3 were cut to join with metallic electrodes (Ni, Ag) using two methods: the conventional with solder and a solder-free method [1]. The joining were performed in the temperature range of 400–450 °C under a pressure of 3 MPa for 30 min. Heat treatment of the joint parts was carried out at 450 °C for 30 h. The SEM images and EDX point measurements along the ZnSb leg after joining were carried out in a Hitachi TM3000 scanning electron microscope.

Acknowledgments

The authors acknowledge the financial support by the Danish Council for Strategic Research under the CTEC Project no. 1305-00002B. The authors also thank TEGnology AS for providing us ZnSb ingots for carrying out this research.

Transparency document. Supplementary material

Transparency document associated with this article can be found in the online version at http://dx.doi.org/10.1016/j.dib.2017.09.023.

Reference

[1] S.A. Malik, L.T. Hung, N.V. Nong, Solder free joining as a highly effective method for making contact between thermoelectric materials and metallic electrodes, Mater. Today Energy 5 (2017) 305–311. http://dx.doi.org/10.1016/j.mtener.2017.07.012.

Appendix-3

Contact of ZnSb thermoelectric material to metallic electrodes using S Bond 400 solder alloy

Authors: Safdar Abbas Malik, Le Thanh Hung and Ngo Van Nong

Status: in press

Available online at www.sciencedirect.com

ScienceDirect

Materials Today: Proceedings 00 (2018) 0000–0000

materialstoday: PROCEEDINGS

www.materialstoday.com/proceedings

ECT_2017

Contact of ZnSb thermoelectric material to metallic electrodes using S-Bond 400 solder alloy

Safdar Abbas Malik[a], Le Thanh Hung[a], Ngo Van Nong[a]*

[a]*Department of Energy Conversion and Storage, Technical University of Denmark, Risø Campus, 4000 Roskilde, Denmark.*

Abstract

ZnSb is one of the promising low-cost p-type thermoelectric materials for constructing waste heat recovery devices operating in the medium temperature region (250 – 400 °C). To obtain high performance, these devices require stable and low resistance contacts between thermoelectric materials and metallic electrodes. In this paper, we investigate the joining of ZnSb to Ni and Ag electrodes using a commercial solder alloy S-Bond 400 and hot-pressing technique. Ti and Cr layers are also introduced as a diffusion barrier and microstructure at the interfaces is observed by scanning electron microscopy. We found that S-bond 400 solder reacts with Ag and Ni electrodes to form different alloys at the interfaces. Cr layer was found to be broken after joining, resulting in a thicker reaction/diffusion layer at the interface, while Ti layer was preserved.

Selection and/or Peer-review under responsibility of 15th European Conference on Thermoelectrics.

Keywords: Thermoelectric Modules; Interface Kinetics; Zinc Antimonide; S-Bond 400

1. Introduction

Thermoelectric (TE) devices generate electricity directly from heat, and hence they offer many possible applications in industry, e.g. waste heat harvesting. The TE devices must operate at high temperatures, therefore, the stability of the materials is a matter of great concern. While many materials have been reported to exhibit excellent TE properties, only a few have been industrialized [1]. Zinc antimonide has been applied in thermoelectric industry since the discovery of the Seebeck effect until Tellurides took the stage in the 1960's [2]. However, the material gained new interest after the discovery of the high thermoelectric figure of merit of its 4:3 (Zn_4Sb_3) phase [3]. Among the

* Corresponding author. *E-mail address:* ngno@dtu.dk

Selection and/or Peer-review under responsibility of 15th European Conference on Thermoelectrics.

compounds based on the semiconductor zinc antimonide, Zn_4Sb_3 and ZnSb phases are the most investigated materials showing good TE performance [4]. In addition, they are low-cost, abundant, and their material processing is environment friendly which makes them one of the best choices for constructing TE device in the medium temperature range. Zn_4Sb_3 has a promising figure of merit, zT, value of 1.4 at 450 °C due to its phonon-glass character caused by Zn atoms on interstitial sites which reduce the thermal conductivity substantially [5]. However, these Zn interstitial atoms in Zn_4Sb_3 are very mobile: under working conditions, they form whiskers within the leg [6] and degrade the material over time. Among the various chemical phases of zinc antimonide [4, 7], the 1:1 phase (ZnSb) has orthorhombic crystal structure and it is expected to be more stable than Zn_4Sb_3 phase since it does not contain mobile Zn on interstitial sites. ZnSb has an indirect bandgap of 0.5 eV at room temperature and carrier concentration of $\approx 10^{16}$ cm^{-3} [8, 9]. Although zinc antimonides have glass-like thermal conductivity which makes them attractive for TE applications, their poor carrier concentration compared with state-of-the-art TE materials [10] has inspired many scientists to try to improve their electrical properties by adding dopants such as Al, Ag, Sn, etc [11,12].

Application of Zn_4Sb_3 and ZnSb in devices is still under investigation. Lin, et al. [13] studied bonding of Zn_4Sb_3 with copper electrode using a solid-liquid interdiffusion process. The thermoelectric leg was coated with Ni and then Ag layer, while the Cu electrode was coated with Ag and then Sn layer. The Zn_4Sb_3/Ni/Ag/Sn/Ag/Cu assembly was heated in vacuum over the range of 250 °C – 325 °C for 5-30 minutes under a pressure of 3MPa. Ag diffusion converts the Sn layer into intermetallic Ag_3Sn and Cu_3Sn, resulting in strong adhesion. Several unintended diffusions also carried on, increasing with time: Zn from Zn_4Sb_3 diffused into the Ni barrier layer to form γ - Ni_5Zn_{21}. Zn also diffused into the Sn layer. Traces of Sb migration into the Sn layer were also identified.

Since Zn_4Sb_3 phase has been found to be unusable on long-term operation for practical purposes, the ZnSb phase was chosen as the subject of study because not only is it stable and cheap, but it also has reasonable TE performance. In our recently published work [14] we investigated the soldering of this material with metallic electrodes at its high-performance temperatures (400 °C) using Zn-2Al solder alloy. The investigation had pointed out that Zn-2Al solder is not suitable for ZnSb material. We also developed a novel solder free joining method to join ZnSb to metallic electrodes, which was initially stable after testing at 400 °C over 30 hours. However, for mass production with low-cost processing, joining with solder alloy is still a preferable method.

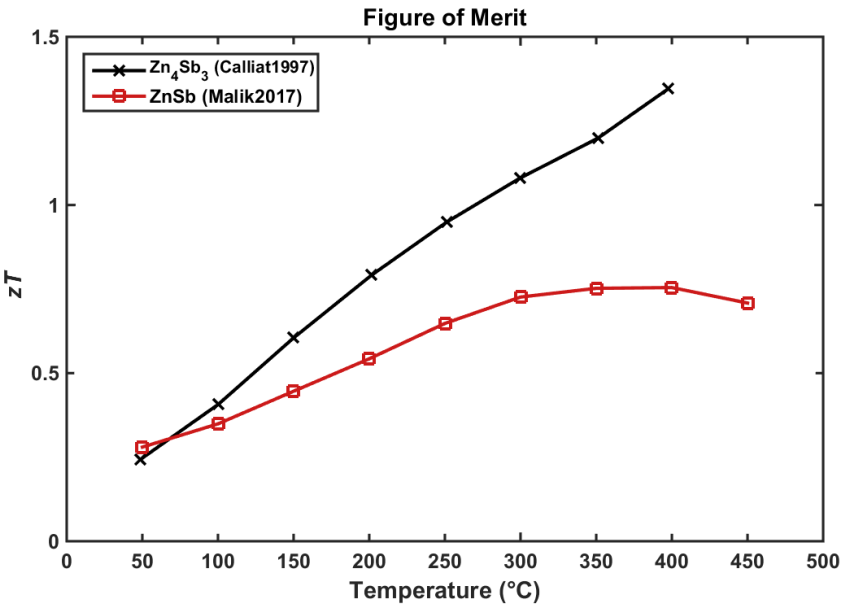

Fig. 1. Thermoelectric figure of merit of ZnSb as compared to the Zn_4Sb_3 phase [3, 14].

In the present paper, the joining of ZnSb material with metallic electrodes is investigated by using a different commercially available S-Bond 400 alloy (Zn-4Ag-2Al with traces of Ga and Ce). With solidus temperature of 400 °C and liquidus temperature of 420 °C, S-Bond 400 alloy can stand the expected operating temperatures of ZnSb (i.e. 300 °C to 400 °C). Copper has been widely used as electrical conductor due to its excellent transport properties, but it is not useful for mid-to-high temperature TE applications because it already starts to oxidize at 350°C [15]. In this study, Silver and Nickel electrodes are chosen because of their excellent transport characteristics, stability in the mid-to-high temperature range, and abundance. These metals are widely used in mid-to-high temperature thermoelectric devices [16,17]. Thin layers (few μm) of Cr and Ti are introduced as a diffusion barrier. The microstructure evolution at the interfaces is observed and discussed in detail.

2. Experimental details

ZnSb ingots used for this study were provided by TEGnology ApS, Denmark. Detailed TE properties of these legs have been reported elsewhere [14]. The ZnSb legs, S-Bond 400 solder, and the Ag, Ni electrodes were cut to their respective dimensions with cross-sectional area of 3 x 3 mm^2. Their surfaces were polished using the SiC sandpaper to remove oxidation layers and to reduce interfacial inhomogeneities, degreased in acetone and finally cleaned with ethanol. All parts were assembled inside a graphite die. To preserve the ZnSb phase of our samples and to minimize the penetration of Zn into the legs, Ti and Cr layers with a thickness of few microns were deposited on ZnSb as diffusion barriers. The joining was performed in Argon atmosphere with temperature maintained for 30 min at 400 °C. A constant pressure of 3 MPa was applied to the samples during the joining process. The assembly was heated around the liquidus temperature of the solder under pressure, so that it melts and wets the electrode and the leg, making a strong mechanical contact between them. The resulting samples were then polished and observed using Hitachi TM3000 electron microscope in BSE mode. The interfaces were scanned in the EDX mode to study the interfacial reactions and interdiffusion.

3. Results and Discussions

Fig. 1 shows the TE figure-of-merit as a function of temperature for ZnSb and Zn_4Sb_3 materials. The peak zT value is 1.4 for 4:3 phase, while it is about 0.8 for the 1:1 phase synthesized by spark plasma sintering (SPS). Although ZnSb has lower zT than Zn_4Sb_3, it is expected to be more stable as we have aforementioned.

Fig. 2 shows the SEM micrographs of the interfaces between Ag, Ni electrodes, Zn-4Ag-2Al solder and ZnSb TE leg. It can be seen that in both cases of Ag and Ni electrodes, no crack or air gap were found at the joint parts. However, a thicker diffusion/reaction layer was observed in Ag case (Fig. 2a). The darker lines at the interfaces represent Cr (Fig. 2a) and Ti (Fig. 2b) barrier layers respectively. However, these two layers behaved quite differently. The Cr layer broke into pieces during the joining process, while the Ti layer stayed intact. One possible reason for this could be the high flux of Ag atoms from the Ag electrode bombarding the Cr interface. This high solubility of Ag in Zn changed the chemical composition of the solder too. The solder has a much higher content of Ag after joining. However, Ag did not diffuse beyond the solder into ZnSb. Due to the broken Cr layer, the interfacial diffusion/reaction region (Fig. 2a) was larger than that for Ti (Fig. 2b). Dark lines at soldering region (Fig. 2a) may be due to different concentrations of Ag/Zn resulting in different contrast.

Fig. 3 shows EDX analysis and lines-scanning through the interfaces. It can be seen from Fig. 3a that Zn from the solder also diffused into the Ag electrode. The interdiffusion between the solder and Ag is so strong that it is hard to identify the boundary between the solder and the electrode from SEM contrast (see Fig. 2a). According to the phase diagram of the Ag-Zn system [18], four intermetallic phases, namely the β, ζ, γ and ε phases with chemical compositions of AgZn (high temperature), AgZn (low temperature), Ag_5Zn_8 and $AgZn_3$ might possibly form during joining [19, 20].

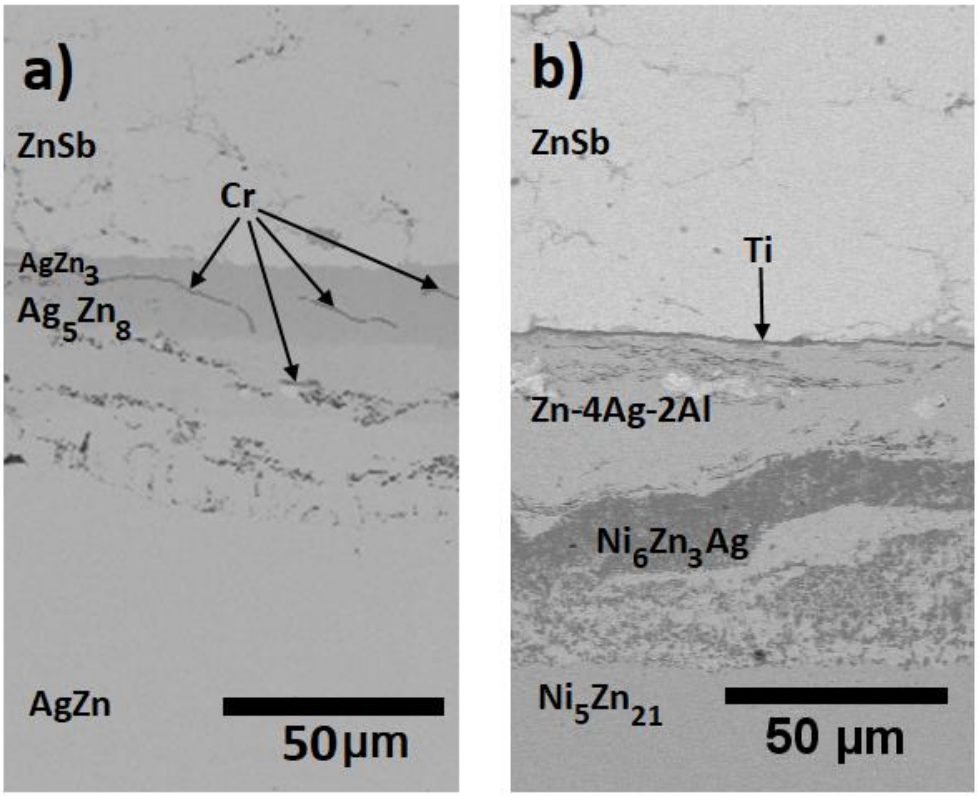

Fig. 2. SEM micrograph of: a) ZnSb/Zn-4Ag-2Al/Ag and b) ZnSb/Zn-4Ag-2Al/Ni samples after joining.

Contrary to the case of Silver, the boundary between Nickel and solder is clearly visible (see Fig. 2b). We observed a dark region of high Nickel content with the possible composition of Ni_6Zn_3Ag, as given by EDX point measurements, in the solder after joining. Fig. 3b shows Ni peaks (green) in EDX linescan of that region. The thermodynamics of the Ni-Zn system [21] suggests low solubility of Ni in Zn. The Ni diffusion that we observed here could be caused by the presence of impurities like Ag (4%), Al (2%) and traces of Ga and Ce which could have modified the free energy landscape of the system. On the other side of the interface, Zn diffused and penetrated into Ni and formed an intermetallic layer with composition Ni_5Zn_{21} [22] as identified by EDX point measurements. Typical compositional ratios of the phases formed during the joining process are given in table 1.

The composition of ZnSb leg was also studied by EDX after joining. EDX point measurements (not shown here) along the leg showed that the Zn concentration was significantly higher than that of Sb in all randomly selected regions (average Zn:Sb ratio is ≈ 56:44). This observed result is similar to the case of Zn-2Al solder as reported [23]. This penetration of Zn into the leg changes the composition of the leg to Zn_4Sb_3 phase. The diffusion of Zn into the material and electrodes may be counterproductive because it might deteriorate their excellent TE properties over time when operating at high temperature with fast cooling [6]. In this case, both Cr and Ti diffusion barriers could not stop the penetration of Zn from solder into ZnSb leg. This could be because the atomic radius of Zn is very small, and also the thickness and density of these barriers may not be good enough.

In Fig. 3, we notice the inhomogeneity in the solder. There are different areas with different concentrations of elements. From Fig. 3a, we can also see that there is a flux of Silver from the electrode through the solder. It is also difficult to distinguish the boundary between the solder and ZnSb. In Fig. 3a, there is a strong signal of Sb next to the Cr peak, which may be an unreacted Sb particle coming from ZnSb, as suggested by the SEM micrographs of the material used in this study [23]. However, in Fig. 3b, the boundary between Ni, the solder and ZnSb is sharp. The solder is more inhomogeneous and there is a region of rich Ni.

Table 1. Typical compositional ratios of the phases formed during the joining process

Formula	% ratio	1	2	3	Average
AgZn	Ag:Zn	54.3:45.7	51.6:48.4	52.6:47.4	52.8:47.2
Ag_5 Zn_8	Ag:Zn	35.7:64.3	34.3:65.7	32.9:67.1	34.3:65.7
$AgZn_3$	Ag:Zn	26.5:73.5	25.1:74.9	23.1:76.9	24.9:75.1
Ni_6 Zn_3 Ag	Ni:Zn:Ag	65.8:25.8:8.4	66.7:26.7:6.6	59.0:31.0:10.0	63.8:27.8:8.4
Ni_5 Zn_{21}	Ni:Zn	21.2:78.8	19.3:80.7	19.9:80.1	20.1:79.9
Zn_4Sb_3	Zn:Sb	53.4:46.6	57.7:42.3	56.6:43.4	55.9:44.1

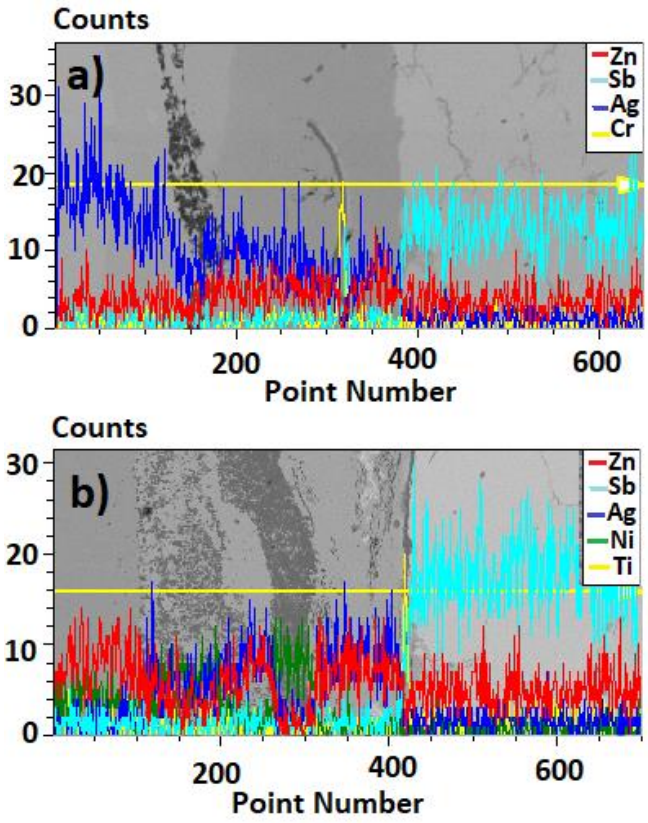

Fig. 3. The EDX linescan of: a) Ag/Zn-4Ag-2Al/ZnSb interface and b) Ni/Zn-4Ag-2Al/ZnSb interface.

4. Conclusion

We have investigated the contacts of ZnSb material to Ag and Ni electrodes using S-Bond 400 solder (Zn-4Ag-2Al) with Cr and Ti as diffusion barrier. The result showed that contacts were formed without any visible cracks or airgaps at the interfaces. However, diffusion/reaction regions were observed at the interface between Ag and Ni electrodes and ZnSb material, and the effect is more substantial for the case of Ag electrode than Ni. The interfacial boundary between ZnSb/Ti/solder/Ni was much clearer than that of ZnSb/Cr/solder/Ag. EDX point measurements along the ZnSb leg after joining revealed that there is a significant higher concentration of Zn, which diffused from the solder and changed the chemical composition of the Zn-Sb material from 1:1 to 4:3 phase. The attempts to stop this penetration by applying a thin layer of Ti and Cr metals as diffusion barriers could not be successful. We think that multi layers of Cr and Ti, or other possible elements such as Mo or Ta, may be a better solution to overcome this issue, and further investigation is ongoing.

5. Acknowledgements

The authors will like to acknowledge the financial support of the Danish Council for Strategic Research under the CTEC project No. 1305-00002B. We would also like to thank TEGnology ApS for providing ZnSb ingots to carry out this research.

References

[1] L.I. Anatychuk, R.V. Kuz, Materials for vehicular thermoelectric generators, J. Electron. Mater. 41 (6) (2012) 1778-1784. DOI: 10.1007/s11664-012-1982-0

[2] Xin Song and Terje G. Finstad, Review of Research on the Thermoelectric Material ZnSb, Thermoelectrics for Power Generation - A Look at Trends in the Technology, Dr. Mikhail Nikitin (Ed.), InTech, (2016). DOI: 10.5772/65661.

[3] T. Caillat, et al., Preparation and Thermoelectric Properties of Semiconducting Zn_4Sb_3, J. Phys. Chem Solids Vol. 58, No. 7, pp. 1119-1125, (1997). DOI: 10.1016/S0022-3697(96)00228-4.

[4] A. Castellero, C. Fanciulli, R. Carlini, G. Fiore, P. Mele, F. Passaretti, M. Baricco, Effect of processing routes on the synthesis and properties of Zn_4Sb_3 thermoelectric alloy, Journal of Alloys and Compounds, (2015), P 54-60. DOI: 10.1016/j.jallcom.2015.08.251.

[5] G.J. Snyder, M. Christensen, E. Nishibori, T. Caillat, B.B. Iversen, Disordered zinc in Zn_4Sb_3 with phonon-glass and electron-crystal thermoelectric properties, Nat. Mater 3 (7) (2004) 458-463. DOI: 10.1038/nmat1154.

[6] Le Thanh Hung, Duc-The Ngo, Li Han, Bo Brummerstedt Iversen, Hao Yin, Nini Pryds and Ngo Van Nong, In Operando Study of High-Performance Thermoelectric Materials for Power Generation: A Case Study of β-Zn_4Sb_3, Adv. Electron. Mater. (2017), 3, 1700223. DOI: 10.1002/aelm.201700223.

[7] J.-B. Li, M.-C. Record, J.-C. Tedenac, A thermodynamic assessment of the Sb-Zn system, J. Alloys Compd. 39 (06) (2007) 171-177. DOI: 10.1016/j.jallcom.2006.08.035.

[8] H. Komiya, K. Masumoto, H.Y. Fan, Optical and electrical properties and energy band structure of ZnSb, Phys. Rev. 133 (1964) A1679-A1684, DOI: 10.1103/PhysRev.133.A1679.

[9] E. Arushanov, Crystal growth, characterization and application of II-V compounds, Prog. Cryst. Growth Charact. 13 (1) (1986) 1-38, DOI: 10.1016/0146-3535(86)90024-9.

[10] G.J. Snyder, E.S. Toberer, Complex thermoelectric materials, Nat. Mater. 7 (2008) 105-114. DOI: 10.1038/nmat2090.

[11] Riccardo Carlini, Daniele Marré, Ilaria Pallecchi, Riccardo Ricciardi, Gilda Zanicchi, Thermoelectric properties of Zn_4Sb_3 intermetallic compound doped with Aluminum and Silver, Intermetallics, Vol. 45, (2014), P 60-64. DOI: 10.1016/j.intermet.2013.10.002.

[12] A.A. Shabaldin, L.V. Prokof'eva, G.J. Snyder, P.P. Konstantinov, G.N. Isachenko, A.V. Asach, The influence of weak Tin doping on the thermoelectric properties of zinc antimonide, J. Electron. Mater. 45 (3) (2016) 1871-1874. DOI: 10.1007/s11664-015-4266-7.

[13] Y. C. Lin, K. T. Lee, J. D. Hwang, H. S. Chu, C. C. Hsu, S. C. Chen, and T. H. Chuang, Solid Liquid Interdiffusion Bonding of Zn4Sb3 Thermoelectric Material with Cu Electrode, Journal of Electronic Materials 45, 4935 (2016). DOI: 10.1007/s11664-016-4645-8.

[14] Safdar Abbas Malik, Le Thanh Hung, Ngo Van Nong, Solder free joining as a highly effective method for making contact between thermoelectric materials and metallic electrodes, Materials Today Energy, Vol. 5, P. 305-311, (2017). DOI: 10.1016/j.mtener.2017.07.012.

[15] K. Mimura, J.-W. Lim, M. Isshiki, Y. Zhu, and Q. Jiang, Brief review of oxidation kinetics of copper at 350 °C to 1050 °C, Metallurgical and Materials Transactions A 37, 1231-1237 (2006). DOI: 10.1007/s11661-006-1074-y.

[16] J. de Boor, D. Droste, C. Schneider, J. Janek, E. Mueller, Thermal Stability of Magnesium Silicide/Nickel Contacts, Journal of Electronic Materials, Vol. 45, No. 10, (2016). DOI: 10.1007/s11664-016-4716-x.

[17] H. N. Pham, N. Van Nong, T. H. Le, B. Balke, L. Han, E. M. Jensen Hedegaard, S. Linderoth, N. Pryds, On the Challenges of Reducing Contact Resistances in Thermoelectric Generators Based on Half-Heusler Alloys, Journal of Electronic Materials, Vol 45, no. 1, pp. 594-601 (2016). DOI: 10.1007/s11664-015-4156-z.

[18] T. Gómez-Acebo, Thermodynamic assessment of the Ag-Zn system, Calphad, 22 (2) (1998) 203-220. DOI: 10.1016/S0364-5916(98)00024-8.

[19] B. Magyari-Köpe, G. Grimvall, L. Vitos, Elastic anomalies in Ag-Zn alloys, Phys. Rev. B 66 (2002) 064210. DOI: 10.1103/PhysRevB.66.064210.

[20] P. Vaessen, B. Lengeler, W. Schilling, Recovery of the electrical resistivity in electron-irradiated, concentrated Silver-Zinc alloys, Radiat. Eff. 81 (3-4) (1984) 277-292. DOI: 10.1080/00337578408206075.

[21] X. Su, N.-Y. Tang, J.M. Toguri, Thermodynamic assessment of the Ni-Zn system, J. Phase Equilibria 23 (2) (2002) 140. DOI: 10.1361/1054971023604125.

[22] G.P. Vassilev, T. Gómez-Acebo, J.-C. Tedenac, Thermodynamic optimization of the Ni-Zn system, J. Phase Equilibria 21 (3) (2000) 287-301. DOI: 10.1361/105497100770340075.

[23] Safdar Abbas Malik, Le Thanh Hung, Ngo Van Nong, Microstructure and chemical data of the thermoelectric ZnSb material after joining to metallic electrodes and heat treatment, Data in Brief, 15 (2017), 97-101. DOI: 10.1016/j.dib.2017.09.023.

Appendix-4

Solder free joining for $CoSb_3$ based Skutterudite thermoelectrics

Authors: Safdar Abbas Malik, Eugen Stamate and Ngo Van Nong

Status: to be submitted

Solder free joining for $CoSb_3$ based Skutterudite thermoelectrics

Safdar Abbas Malik, Eugen Stamate, Ngo Van Nong

Department of Energy Conversion and Storage,

Technical University of Denmark,
Risø Campus, 4000 Roskilde, Denmark

Abstract

Skutterudites are among the most promising thermoelectric (TE) materials in the medium to high temperature range (300 ^{o}C to 600 ^{o}C) because of their high TE performance (zT>1). However, the use of these high performance materials in practical TE devices is still very limited due to the challenges in formation of good and stable contacts with electrodes. In this work, we report a new approach using solder-free joining method to make contacts of $CoSb_3$ based filled skutterudite legs with low-cost and stable Crofer 22 APU electrode. Commercially available high performance skutterudite material was sintered by Spark Plasma Sintering (SPS) technique. Their thermoelectric properties were measured from RT to 550 ^{o}C. The results show that the SPS sintered sample has a maximum zT value of 1.5 at 550 ^{o}C, which is comparable with the best reported value in the literature. The TE properties of Crofer 22 APU show similar characteristics to most of the metals, i.e. very low electrical and thermal resistivities and low Seebeck coefficient. For contacts by solder free joining method, a thin layer of Cr and a multilayer Cr/Co were used to bond the skutterudite legs to the Crofer 22 APU electrode at 550 ^{o}C under 1.5 MPa for 30 minutes. We found that a very good interfacial contact without any visible gaps or cracks was formed between the TE material and Crofer 22 APU. The contact remained stable after long term testing at 550 ^{o}C for 300 hours, although some changes could be observed at the interface.

Keywords: low-cost thermoelectrics, contact resistance, Skutterudite, thermoelectric modules, interface kinetics

---

1. Introduction

It is estimated that more than 50% of industrial usage of energy is lost in the form of waste heat[1]. The interplay of heat and electrical currents has been investigated since 1823 when Seebeck noted that a compass needle would deflect if it was placed near a closed loop of two dissimilar conductors and one of the junctions was heated[2]. This effect was later termed as thermoelectric effect[3]. With increasing demands for renewable energy resources, thermoelectric (TE) technology has drawn attention of the scientific community[4]. Poly-crystalline, degenerate semiconductors, that can manage to sufficiently scatter phonons but has high mobility channels for the charge carriers - i.e. 'phonon-glass electron-crystal' materials - exhibit the best thermoelectric performance[5]. One of the major hurdles in the path of widespread application of this technology is the stability of the metal-thermoelectric joints under practical circumstances[6]. Efficient TE material exhibits a fine balance between a number of inter-related physical properties, namely: the material Seebeck coefficient, 'α'; the electrical conductivity, 'σ'; and the thermal conductivity, 'κ'. The dimensionless figure of merit, zT, is a measure of the performance of a TE material[7]:

$$zT = \frac{\alpha^2 \sigma T}{\kappa} \quad (1)$$

The device figure of merit, ZT, can be defined in terms of the total Seebeck coefficient, S, total electrical resistance, R, and total thermal conductance, K, of the module [8] as:

$$ZT = \frac{S^2 T}{RK} = \frac{S^2 T}{(R_{leg} + R_c)(K_{leg} + K_c)}. \quad (2)$$

here, $R = R_{leg} + R_c$ and $K = K_{leg} + K_c$. R_c and K_c are the electrical and thermal contact resistances, respectively. It is obvious from equation 2 that low contact resistance is necessary in order to increase the device figure of merit. Strong adhesion and absence of cracks and airgaps at the interface reduces the electrical and thermal contact resistances.

Skutterudites are a promising class of materials that can be used for thermoelectric applications in the mid to high temperature region. The general formula of these materials is RM_4X_{12}: R is the so-called "rattler" used to fill the large void spaces in the unit cells; M is a transition metal, e.g. Co, Fe, Ru, or Os; and X is P, As, or Sb. They are cubic with 34 atoms per unit cell and belong to the space group $IM\bar{3}$ [9]. The structure consists of square planar rings of four pnictogen (Nitrogen family, the X) atoms along the (100), (010), or (001) directions. The unit cell can be thought of as an array of MX_6 distorted octahedrons, sharing corners. This arrangement gives two large unfilled cavities which are available for the fillers, R. The transition metal atoms (M) form a simple cubic sublattice and the rattlers fill the two void cages in the unit cell. When the R atoms are absent from the structure, the binary skutterudite antimonides show excellent transport characteristics [10][11]. Filling of the cavities provides phonon scattering centers that reduce the thermal conductivity substantially, with phonon-glass spatially separated from the electron-crystal of the Sb sublattice [12][13][14]. Filled skutterudites have extra phonon modes [15], the atoms filling the voids reduce thermal conductivity.

Rogl et al. [16] have studied the TE properties of p-type ($DD_y(Fe_{1-x}Co_x)_4Sb_{12}$) and n-type (($Mm, Sm)_yCo_4Sb_{12}$) filled skutterudite materials produced by Treibacher Industrie AG. They first processed the powder to obtain small grain sizes, and then hot-pressed it under a uniaxial pressure in Argon atmosphere to obtain sample pellets. The samples resulting from ball-milled powders appeared to have smaller grain sizes (<1μm). The zT for p-type samples peaked at 500°C, in the range of 1.1 to 1.3, higher for the ball milled samples due to their low thermal conductivities. In the case of n-type samples, the effect of microstructure on the transport properties was more evident and all of the thermoelectric properties appeared to change with respect to average grain size. This indicates not only the phonon transport was hindered but also the electrons faced scattering and filtering at the grain boundaries. The zT for n-type samples peaked at 550°C, in the range of 1.0 to 1.6, higher for the ball milled samples.

Thermal degradation of pure $CoSb_3$ occurs because of two mechanisms: (i) oxidation in air, resulting into a complex three-layered scale consisting of $CoSb_2O_4$, $CoSb_2O_6$, Sb_2O_3 and Sb_2O_4 layers, (ii) thermal decomposition into $CoSb_2$, CoSb and Sb_4, whereby Sb_4 evaporates. The oxidation of pure $CoSb_3$ material starts at about 380°C and the oxidation activation energy of the pure material is about 170 kJ/mol [17]. Exothermic differential thermal analysis (DTA) peaks were observed at 583°C, 655°C, and 740°C; accompanied by derivative thermogravimetry (DTG) peaks. Powder XRD performed on the completely oxidized $CoSb_3$ at 550°C and 650°C indicated that the main products were: α-Sb_2O_4, $CoSb_2O_6$ and $CoSb_2O_4$. The optical micrograph of a cross section of $CoSb_3$ surface heated in air at 600°C for 48 hours showed three layers with different colors formed. An X-ray diffraction depth profile showed that the top layer is made of α-Sb_2O_4 and the next two layers are of $CoSb_2O_6$ and $CoSb_2O_4$, respectively. The inner $CoSb_2O_4$ was also observed to be 4-times thicker than the $CoSb_2O_6$ layer on top of it. The electrical conductivity and Seebeck

coefficient were measured after thermal treatment of $CoSb_3$ at 615^{o}C for 48 hours. It was noted that the thermal treatment enhanced the electrical conductivity (σ) 4-times and decreased the value of Seebeck coefficient (α) twice, resulting in the same power factor ($\alpha^2\sigma$) as before. For Fe-doped $CoSb_3$ alloys, the starting temperature and activation energy of oxidation is slightly different[18]. Skald et al. [19] studied the oxidation behavior of Ce-filled Fe_4Sb_{12} from room temperature to 800^{o}C in air. The oxidation already starts slowly at 225^{o}C and the mass gain starts to increase after 300^{o}C. With increasing temperature, the surface of sample changes colors indicating formation of different compounds. At the temperatures below 500^{o}C, powder XRD could only observe Sb and Ce based oxide crystallites, however at 800^{o}C, $FeSbO_4$ was observed along with Sb_2O_4 and CeO_2. For better insight, X-ray absorption near edge spectroscopy (XANES) was performed which indicated the onset of formation of an Fe^{3+} oxide at 300^{o}C. However, since this phase was not detected by powder XRD, it ought to be polycrystalline.

Leszczynski et al.[17] studied the decomposition of $CoSb_3$ doing a non-isothermal DTA in He gas flow and thermogravimetry (TG) analysis in vacuum-sealed quartz tubes. They found that the endothermic decomposition of $CoSb_3$ starts at about 420^{o}C and that four DTG peaks can be observed whose onset temperatures are approximately 580^{o}C, 690^{o}C, 870^{o}C, and 930^{o}C, for a heating rate of 10 K/min. The increase of decomposition rate at 580^{o}C with the peak maximum at 640^{o}C could be attributed to faster antimony sublimation for exceeding the melting point of antimony (630^{o}C). For the next DTG peak with onset temperature of 690^{o}C, they assumed that it may correspond to activation of a faster antimony diffusion path. They attributed the subsequent increases of decomposition rate at 875^{o}C and 930^{o}C to the thermodynamic stability limits of the δ-CoSb3 (874^{o}C) and γ-$CoSb_2$ (930^{o}C) phases, respectively. The product of $CoSb_3$ decomposition in vacuum was mainly $CoSb_2$ and Sb_4. $CoSb_2$ did not seem to further decompose into CoSb, this could be because the TG was performed in sealed quartz tubes and the gradually increasing Sb_4 pressure might have affected the decomposition process. This explanation is also supported by the fact that the mass loss of $CoSb_3$ sample in sealed vacuum quartz tubes was much smaller than that in inert gas flow. F. Wu et al.[20] studied the TG and DTG curves for different heating rates (5^{o}C/min, 10^{o}C/min, 15^{o}C/min and 20^{o}C/min) and observed faster decomposition for higher heating rate. The peaks in weight loss were also shifted to lower temperatures for when heating rate was high.

The application of skutterudite thermoelectrics to make devices has also become a hot topic lately. Both conventional brazing[21][22] and current assisted co-sintering[23] [24] methods have been studied. Zhao et al. [21] used Mo–Cu alloy as electrode and Ag–Cu alloy as brazing agent, using a 20μm thick Mo layer as a diffusion barrier. The joining quality was good and the efficiency was measured to be 6.4% and output power seemed to stay unaltered under thermal cycling. However, long-term stability is still an open question. Chen et al. [22] studied the joining to Ag–Cu braze alloy with Co, Ni and Ti barrier layers sputtered on the $CoSb_3$ substrate, and also without any barrier layer. It was noted that without the barrier, the solder would completely diffuse into $CoSb_3$ within 3 days. On the contrary, the Co barrier layer forms a thin intermetallic layer with the braze alloy after 40 days of reaction at 600^{o}C, which indicates low Cu and Ag solubility in Co. However, on the $CoSb_3$ side of the joint, Co reacts with the thermoelectric to form CoSb and $CoSb_2$ layers which grow slowly with time (>10μm) and cracks start to appear at the interface after 44 days of reaction at 450^{o}C. The Ni barrier layer reacted fast with both the material and the braze alloy. In the case of Ti barrier layer, 4 binary Cu–Ti compounds were formed at the Ag–Cu/Ti interface. However, the reaction layers formed at the Ti/$CoSb_3$ interface were quite thin (<3μm after 21 days), although the Ti layer detached itself from the $CoSb_3$ surface.

Zhao et al. [23] sintered $CoSb_3$ powder on a Ti barrier foil and Mo–Cu electrode. The joint was studied after thermal aging at temperatures of 550 ^{o}C, 575 ^{o}C and 600 ^{o}C for 0-20 days. The joining had no gaps or cracks when tested below 600 ^{o}C. Intermetallic phases TiSb, $TiSb_2$ and ToCoSb formed at Ti/$CoSb_3$ interface and grew over time. In a recent work, Zhao et al. [24] co-sintered $CoSb_3$ powder with Ti powder as a barrier layer and W–Cu metallic alloy as the electrode, using spark plasma sintering technique. The W–Cu electrode was chosen because of comparable thermal expansion coefficients. No cracks appeared at the Ti/$CoSb_3$ interface for W–20Cu electrode because it's thermal expansion co-efficient is pretty close to $CoSb_3$ in the operating temperature range (10×10^{-6}/^{o}C to 11×10^{-6}/^{o}C). After thermal aging at 500 ^{o}C for 30 days, the Ti

layer did not detach, and intermetallic TiSb layer formed at the Ti/$CoSb_3$ interface. Increased temperature of 550^{o}C resulted in thicker (~20 μm) intermetallic layer and formation of two more phases, $TiSb_2$ and TiCoSb. Thermal aging decreased the shear strength of the joint because the intermetallic phases formed at the Ti/$CoSb_3$ interface are brittle. It also increased the electrical contact resistance. So far, most commonly used electrodes in the mid to high temperature range are Ag and Ni, which are costly and unstable at high temperatures. Low cost, stable materials and innovative joining method are needed.

Commercially available Crofer 22 APU [25] has proved to be a very promising electrode for solid oxide fuel cells[26]. It is an Fe–22Cr alloy with small traces of Mn, C, Si, Cu, Al, S, P, Ti, La. It is a low cost and stable alloy, with metallic transport properties and low coefficient of thermal expansion (10.3×10^{-6}/^{o}C at 200 ^{o}C to 12.7×10^{-6}/^{o}C at 1000 ^{o}C). Kaderi et al. [27] observed the oxidation behavior of Crofer 22 APU by in-situ XPS in the low-to-mid temperature range (< 700^{o}C). Cr ions start moving to the surface and form oxide layer at 300 °C with a Cr concentration reaching its maximum at 500°C. Mn and Ti ions reach the surface at 500 °C and 700 °C, respectively and form oxides. This process also reduces Fe oxides present on the surface as oxygen prefers Cr. Thermal degradation and oxidation of this alloy at elevated temperatures was examined by Park et al. [28]. Upon annealing in air at elevated temperatures (> 800^{o}C), layers of conducting chromia (Cr_2O_3) and chromium-manganese oxide ($(Mn, Cr)_3O_4$) covered the samples. The thickness of the chromia layer increased relatively faster after 825 ^{o}C.

Recently, we have developed a novel solder-free joining method and we have successfully applied this method to join ZnSb with Ni electrode [29]. The interface of this contact was found to be stable at 400 ^{o}C after 30 hours. In the present work we employ and further developed this method for $CoSb_3$ based filled skutterudite material using Crofer 22 APU electrode. The thermoelectric properties of SPS sintered TE material are investigated over the desired temperature range and compared with the reported hot-pressed samples. The thermoelectric properties of Crofer 22 APU electrode are also measured to confirm its metallic nature. Cr and Co layers were deposited by DC sputtering on the clean and polished surface of skutterudite legs. Interface microstructure was observed after joining as well as after long term testing at high temperature.

2. Methods

The commercial powders of p-type and n-type skutterudites were obtained from Treibacher Industrie AG and SPS sintered using Dr. Sinter in vacuum under a uniaxial pressure of 50 MPa. Sintering temperature for the p-type leg was 650^{o}C and for n-type leg, it was 700 ^{o}C. After sintering, the pellets were taken out of the graphite die, cleaned and cut for thermoelectric characterization and joining experiments. The electrical resistivity and Seebeck coefficient were measured on an ULVAC-RIKO ZEM-3 from room temperature (RT) to 550 ^{o}C in 0.1 Bar Helium atmosphere. The thermal conductivity was calculated from the thermal diffusivity and heat capacity obtained by the laser flash method on NETZSCH LFA 457 MicroFlash ^{R}, and mass density using the Archimedes principle. For the joining experiments, the skutterudite legs, Al–12Si braze and electrode were cut to their respective dimensions with cross-sectional area of 4mm × 4mm. Their surfaces were polished using the SiC sandpaper to remove oxidation layers and to reduce interfacial inhomogeneities, degreased in Acetone and finally cleaned by Ethanol. Microlayers of Cr and Co/Cr multilayer were deposited on the skutterudite substrate using DC sputtering. All parts were assembled together inside a graphite die. The joining was performed in Argon atmosphere. The joining temperature was maintained for 30 minutes at 500 ^{o}C. A constant pressure of 3 MPa was applied on the samples during the joining process. A long term test was run for 300 hours at 500 ^{o}C. The resulting samples were then polished and observed using Hitachi TM3000 electron microscope. The interfaces were scanned in the EDX mode to study the interfacial reactions and interdiffusion.

3. Results and Discussion

3.1 Thermoelectric Properties

Figure 1 shows the TE properties of the SPS sintered p-type skutterudite as a function of temperature from RT to 550°C, alongside the literature values of the best hot-pressed samples for comparison. The electrical resistivity tends to increase with increasing temperature, showing a metallic behavior (see figure 1 (a)). The Seebeck coefficient has a positive value in the entire measured temperature range, indicating a p-type conduction, as shown in figure 1 (b). Both the electrical resistivity and Seebeck coefficient start to flatten after 400°C. A similar trend has been observed by Rogl et al. [16] for hot pressed samples. However, the Seebeck coefficient values are lower in magnitude, this could be attributed to the change in synthesis method. SPS is a fast and current assisted technique which could not only introduce microstructural inhomogeneities but also cause ion migration.

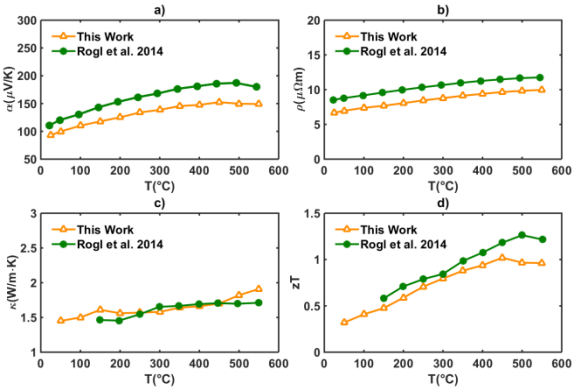

Figure 1: Temperature dependence of the TE properties of SPS sintered p-type skutterudite: a) electrical resistivity, b) Seebeck coefficient, c) thermal resistivity, d) figure of merit.

The thermal conductivity for our SPS sintered samples is very close to the ball milled, hot-pressed samples of Rogl et al. (see figure 1 (c)). The same trend was also observed by Rogl et al. [16] as well, this trend indicates that the electronic contribution to the thermal conductivity is dominant at elevated temperatures. The best performing samples reported by Rogl et al. were carefully prepared with nanostructured grains. The perfect match of thermal conductivity values indicates that the fast SPS method can result in phonon-glass like characteristics.

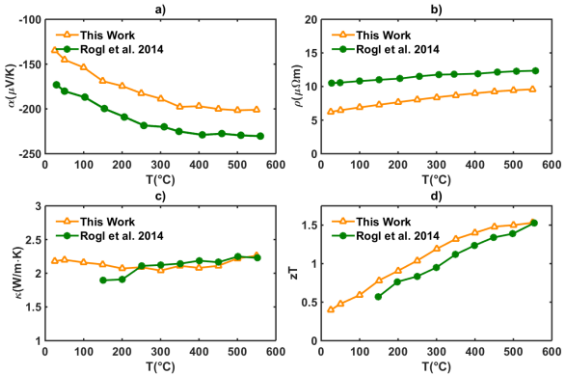

Figure 2: Temperature dependence of the TE properties of SPS sintered n-type skutterudite: a) electrical resistivity, b) Seebeck coefficient, c) thermal resistivity, d) figure of merit.

Figure 2 shows the TE properties of the SPS sintered n-type skutterudite as a function of temperature from RT to 500°C. The electrical resistivity tends to increase with increasing temperature, showing a metallic behavior (see figure 2 (a)). The Seebeck coefficient has a negative value in the entire measured temperature range, indicating an n-type conduction, as shown in figure 2 (b). The magnitude of Seebeck coefficient start to become constant after 450°C. A similar trend has been observed by Rogl et al. [16] for hot pressed samples. However, the magnitudes are closer to the samples that were not ball milled and had bigger grain sizes. The thermal conductivity is in good agreement with the best performing sample of Rogl et al. (see figure 1 (c)). This almost constant value was also reported by Rogl et al. [16] as well, with the same order of magnitude for samples with nanostructuring. The lower magnitude of Seebeck coefficient and electrical resistivity cancel out and the overall zT values are as good as the best hot-pressed samples in literature.

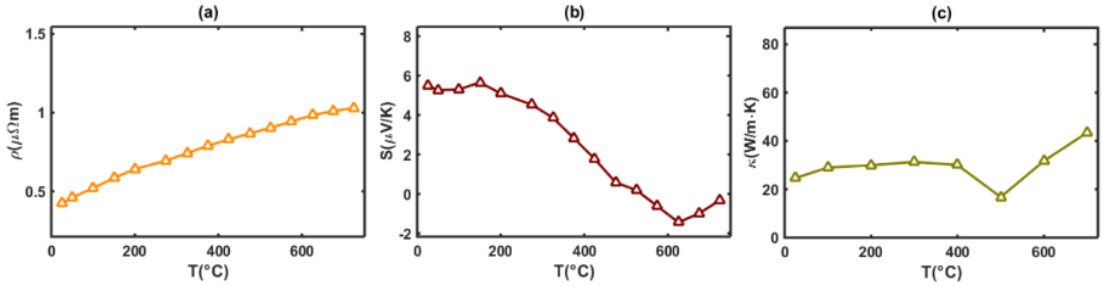

Figure 3: Temperature dependence of the TE properties of Crofer 22 APU: a) electrical resistivity, b) Seebeck coefficient, c) thermal resistivity.

Figure 3 shows the TE properties of Crofer 22 APU as a function of temperature from RT to 700°C. The electrical resistivity is as low as pure metals, and it increases with increasing temperature because of increasing electron-lattice scattering. The Seebeck co-efficient is also very low in magnitude, however the sign of the Seebeck coefficient is positive. This is also the case for most metals and it has been discussed in detail by K. Behnia [30]. The thermal conductivity of the alloy is also comparable with metals.

3.2 Solder-free joining

Solder-free joining is a modified diffusion bonding between two materials, under application of a uniaxial pressure at elevated temperature, facilitated by a few micron thick layer of a carefully chosen metal. Few micron layer of Cr and Cr/Co multilayer were grown on the cleaned skutterudite substrates.

Figure 4 (a) shows the SEM micrograph of bonding between Crofer electrode and n-type skutterudite with Cr layer as the interconnect. It is evident that the contact is solid formed. An IMC diffusion/reaction region of < 5 µm is observed at the interface. On the skutterudite side of the interface, a layer of Sb rich phase has developed which adds to strengthening of the bond. A few Sb rich grains are also observed in Crofer. These grains don't seem to dissolve in the Crofer matrix, hence the excellent transport properties of the electrode are preserved. Figure 4 (b) shows the SEM micrograph of bonding between Crofer electrode and n-type skutterudite with Cr/Co multilayer as the interconnect. It is evident that the joint is solid formed. An IMC diffusion/reaction region of ~10 µm is observed at the interface. On the skutterudite side of the interface, Co layer reacted with the TE material to form layers of CoSb and $CoSb_2$ phases.

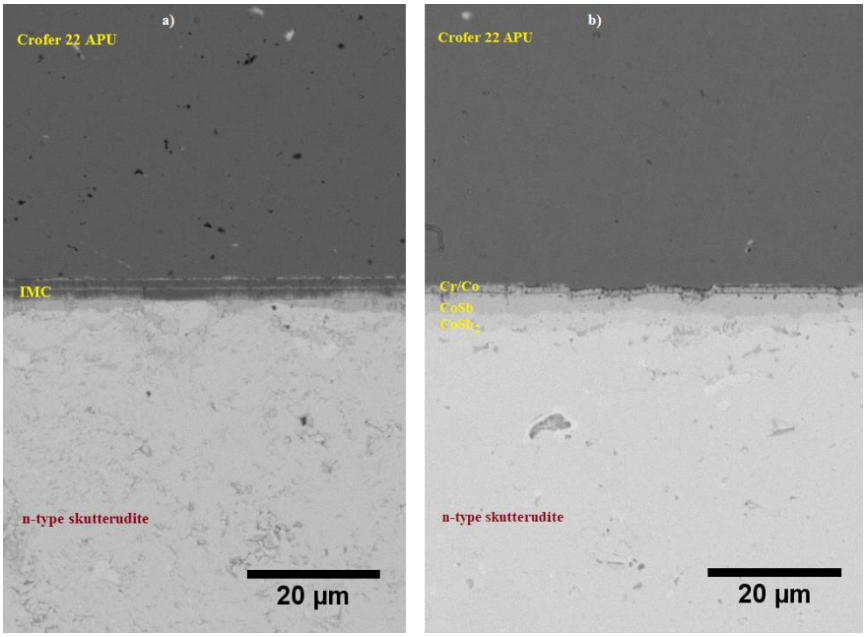

Figure 4: SEM micrograph of: a) Crofer 22 APU/Cr/n-type skutterudite, b) Crofer 22 APU/Cr/Co/n-type skutterudite.

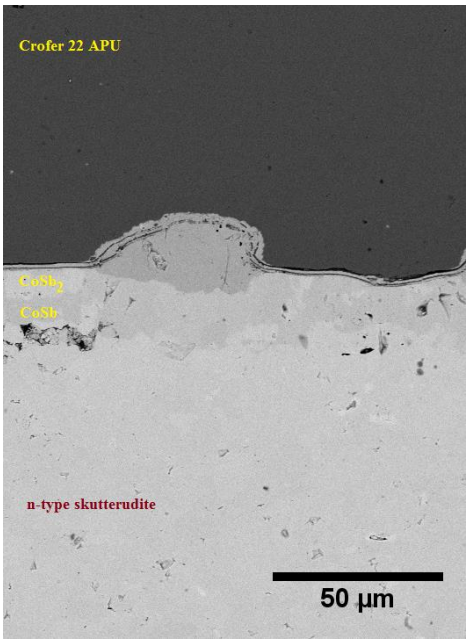

Figure 5: SEM micrograph of Crofer 22 APU/Cr/Co/n-type skutterudite after heat treatment at 500 °C for 300 hours.

Figure 5 (a) shows the SEM micrograph of the sample with Cr/Co multilayer after 300 hours of heat treatment at 500 °C. The quality of joint is still good. However, the materials seem to be interlocked by some micrograins of skutterudite penetrating into the electrode. This phenomenon needs to be further investigated. The IMC diffusion/reaction region has not grown further and seems to have reached saturation point. On the skutterudite side of the interface, Co layer reacted with the TE material to form layers of CoSb and $CoSb_2$ phases.

4. Conclusion

We have shown that the high performance of filled skutterudite thermoelectrics could also be achieved by the spark plasma sintering method, which is much faster than the ball milling and hot-pressing route. The material figure of merit, zT, has the same order of magnitude as the best reports in the literature. Our investigation of transport properties of the low cost and stable electrode, Crofer 22 APU, confirmed the metallic behavior of this alloy. Using solder-free joining with single Cr and multi Cr/Co layers, good contacts between n-type skutterudite and Crofer 22 APU were formed thanks to a think alloying region that formed due to the intermetallic reaction at the interface. Long term test on the Cr/Co multilayer sample for 300 hours has shown that the diffusion does not develop further and the quality of joint was preserved.

Acknowledgments

We gratefully acknowledge the financial support by the Danish Council for Strategic Research under the CTEC project No. 1305-00002B.

References

[1] U.S. Department of Energy, "Waste Heat Recovery: Technology and Opportunities in U.S. Industry," 2008.

[2] T. J. Seebeck, "Magnetische Polarisation der Metalle und Erze durch Temperatur-Differenz (Magnetic polarization of metals and ores by temperature differences)," *Abhandlungen der Königlichen Akad. der Wissenschaften zu Berlin*, pp. 265–373, 1822.

[3] H. C. Ørsted, "On some new thermoelectric experiments performed by Baron Fourier and M. Ørsted (1823)," in *Selected Scientific Works of Hans Christian Ørsted*, K. Jelved, A. D. Jackson, and O. Knudsen, Eds. Princeton University Press, 1998, pp. 470–477.

[4] W. Liu, J. Hu, S. Zhang, M. Deng, C.-G. Han, and Y. Liu, "New trends, strategies and opportunities in thermoelectric materials: A perspective," *Mater. Today Phys.*, vol. 1, pp. 50–60, Jun. 2017.

[5] B. C. Sales, D. Mandrus, B. C. Chakoumakos, V. Keppens, and J. R. Thompson, "Filled skutterudite antimonides:Electron crystals and phonon glasses," *Phys. Rev. B*, vol. 56, no. 23, pp. 15081–15089, 1997.

[6] X. R. Ferreres, S. Aminorroaya Yamini, M. Nancarrow, and C. Zhang, "One-step bonding of Ni electrode to n-type PbTe - A step towards fabrication of thermoelectric generators," *Mater. Des.*, vol. 107, pp. 90–97, 2016.

[7] A. F. Ioffe, *Semiconductor Thermoelements and Thermoelectric Cooling*. London: Infosearch Limited, 1957.

[8] H. J. Goldsmid, "Conversion efficiency and figure of merit," in *CRC Handbook of Thermoelectrics*, D. Rowe, Ed. CRC Press, 1995.

[9] W. Jeitschko and D. Braun, "LaFe4P12 with filled CoAs3-type structure and isotypic lanthanoid–transition metal polyphosphides," *Acta Crystallogr. Sect. B Struct. Crystallogr. Cryst. Chem.*, vol. 33, no. 11, pp. 3401–3406, 1977.

[10] D. T. Morelli, T. Caillat, J. P. Fleurial, A. Borshchevsky, J. Vandersande, B. Chen, and C. Uher, "Low-temperature transport properties of p-type CoSb3," *Phys. Rev. B*, vol. 51, no. 15, pp. 9622–9628, 1995.

[11] J. W. Sharp, E. C. Jones, R. K. Williams, P. M. Martin, and B. C. Sales, "Thermoelectric properties of CoSb3 and related alloys," *J. Appl. Phys.*, vol. 78, no. 2, pp. 1013–1018, 1995.

[12] B. C. Sales, D. Mandrus, and R. K. Williams, "Filled Skutterudite Antimondies: A New Class of Thermoelectric Materials," *Science (80-.).*, vol. 272, no. V, p. 5266, 1996.

[13] D. J. Singh and W. E. Pickett, "Skutterudite antimonides: Quasilinear bands and unusual transport," *Phys. Rev. B*, vol. 50, no. 15, pp. 11235–11238, 1994.

[14] D. Jung, M. H. Whangbo, and S. Alvarez, "Importance of the X4 Ring Orbitals for the Semiconducting, Metallic, or Superconducting Properties of Skutterudites MX3 and RM4X12," *Inorg. Chem.*, vol. 29, no. 12, pp. 2252–2255, 1990.

[15] P. Lu, Z. Shen, and X. Hu, "Effects of the voids filling on the lattice vibrations for the CoSb3-based thermoelectric materials—Raman scattering spectra and theoretical study," *Phys. B Condens. Matter*, vol. 405, no. 11, pp. 2589–2592, 2010.

[16] G. Rogl, A. Grytsiv, P. Rogl, E. Bauer, M. Hochenhofer, R. Anbalagan, R. C. Mallik, and E. Schafler, "Nanostructuring of p- and n-type skutterudites reaching figures of merit of approximately 1.3 and 1.6, respectively," *Acta Mater.*, vol. 76, pp. 434–448, 2014.

[17] J. Leszczynski, K. T. Wojciechowski, and A. L. Malecki, "Studies on thermal decomposition and oxidation of CoSb3," *J. Therm. Anal. Calorim.*, vol. 105, no. 1, pp. 211–222, 2011.

[18] K. H. Park, S. W. You, S. C. Ur, I. H. Kim, S. M. Choi, and W. S. Seo, "High-temperature stability of thermoelectric skutterudite In 0.25Co 3FeSb 12," *J. Electron. Mater.*, vol. 41, no. 6, pp. 1051–1056, 2012.

[19] A. C. Sklad, M. W. Gaultois, and A. P. Grosvenor, "Examination of CeFe4Sb12 upon exposure to air: Is this material appropriate for use in terrestrial, high-temperature thermoelectric devices?," *J. Alloys Compd.*, vol. 505, no. 1, pp. 6–9, 2010.

[20] F. Wu, Q. He, D. Hu, F. Gao, H. Song, J. Jia, and X. Hu, "Thermal decomposition of thermoelectric material CoSb3: A thermogravimetry kinetic analysis," *J. Electron. Mater.*, vol. 42, no. 8, pp. 2574–2581, 2013.

[21] D. Zhao, C. Tian, S. Tang, Y. Liu, L. Jiang, and L. Chen, "Fabrication of a CoSb3 - based thermoelectric module," *Mater. Sci. Semicond. Process.*, vol. 13, pp. 221–224, 2010.

[22] S. wen Chen, A. H. Chu, and D. S. H. Wong, "Interfacial reactions at the joints of CoSb3-based thermoelectric devices," *J. Alloys Compd.*, vol. 699, pp. 448–454, 2017.

[23] D. Zhao, X. Li, L. He, W. Jiang, and L. Chen, "High temperature reliability evaluation of CoSb3/electrode thermoelectric joints," *Intermetallics*, vol. 17, no. 3, pp. 136–141, 2009.

[24] D. Zhao, H. Geng, and X. Teng, "Fabrication and reliability evaluation of CoSb3/W–Cu

thermoelectric element," *J. Alloys Compd.*, vol. 517, pp. 198–203, 2012.

[25] VDM-Metals, "VDM ® Crofer 22 APU," no. Werkstoffdatenblatt Ausgabe Januar, p. 10, 2010.

[26] J. W. Fergus, "Metallic interconnects for solid oxide fuel cells," *Mater. Sci. Eng. A*, vol. 397, no. 1–2, pp. 271–283, 2005.

[27] A. Bin Kaderi, H. Hartmann, and A. Besmehn, "Observation of Oxide Development from Room Temperature (RT) to 700 oC Demonstrated by In Situ XPS of Crofer 22 APU Alloy," *Oxid. Met.*, vol. 88, no. 3, pp. 459–468, Oct. 2017.

[28] M. Park, J.-S. Shin, S. Lee, H.-J. Kim, H. An, H. Ji, H. Kim, J.-W. Son, J.-H. Lee, B.-K. Kim, H.-W. Lee, and K. J. Yoon, "Thermal degradation mechanism of ferritic alloy (Crofer 22 APU)," *Corros. Sci.*, vol. 134, pp. 17–22, 2018.

[29] S. A. Malik, L. T. Hung, and N. Van Nong, "Solder free joining as a highly effective method for making contact between thermoelectric materials and metallic electrodes," *Mater. Today Energy*, vol. 5, pp. 305–311, Sep. 2017.

[30] K. Behnia, *Fundamentals of Thermoelectricity*, 1st ed. Oxford University Press, 2015.